

EVALUATING LONG-TERM CHANGES AND THEIR CAUSES IN SURFACE
SOLAR IRRADIANCE IN OREGON

by

LAURA RIIHIMAKI

A DISSERTATION

Presented to the Department of Physics
and the Graduate School of the University of Oregon
in partial fulfillment of the requirements
for the degree of
Doctor of Philosophy

September 2008

University of Oregon Graduate School

Confirmation of Approval and Acceptance of Dissertation prepared by:

Laura Riihimaki

Title:

"Evaluating Long-Term Changes and their Causes in Surface Solar Irradiance in Oregon"

This dissertation has been accepted and approved in partial fulfillment of the requirements for the Doctor of Philosophy degree in the Department of Physics by:

Gregory Bothun, Chairperson, Physics
Stephen Kevan, Member, Physics
Frank Vignola, Member, Physics
James Coakley, Member, Not from U of O
Mark Reed, Outside Member, Geological Sciences

and Richard Linton, Vice President for Research and Graduate Studies/Dean of the Graduate School for the University of Oregon.

September 6, 2008

Original approval signatures are on file with the Graduate School and the University of Oregon Libraries.

An Abstract of the Dissertation of
Laura Dian Riihimaki for the degree of Doctor of Philosophy
in the Department of Physics to be taken September 2008
Title: EVALUATING LONG-TERM CHANGES AND THEIR CAUSES IN SURFACE
SOLAR IRRADIANCE IN OREGON

Approved: _____
Dr. Gregory Bothun

The amount of solar radiation at the earth's surface is modulated by fluctuations in aerosol density and cloud optical depth--two uncertain factors in climate change studies. The University of Oregon Solar Radiation Monitoring Lab has collected five-minute resolution surface shortwave irradiance measurements at three sites in Oregon since 1980 or earlier. Direct normal surface solar irradiance has increased 4-5% per decade (8-11 W/m^2 per decade) at these three sites since 1980 (1979 in Eugene). Total solar irradiance has likewise increased by 1-2% per decade (2-3 W/m^2 per decade). This unusually long direct normal time series was used to examine the causes of trends because of its high sensitivity to scattering and high instrumental accuracy.

The strongest factor causing direct normal irradiance trends was found to be the high stratospheric aerosol concentrations after the volcanic eruptions of El Chichón (1982) and Mt. Pinatubo (1991). Removing the four years most impacted by each volcanic

eruption (1982-1985 and 1991-1994) reduces the trend in annual average direct normal irradiance by 20-55%, depending on the site.

All measurement sites show low irradiance values before the volcanic eruption of El Chichón in 1982 compared to later periods of relatively low volcanic aerosols (1989-1990, and 2000-2007). These low values are visible both in all-sky and clear-sky monthly averages, suggesting high aerosol loads as a likely cause.

Clear-sky direct normal irradiance measurements from high solar zenith angles (65-75°) are analyzed to test the hypothesis that the increase in irradiance comes from a reduction of anthropogenic aerosols since the late 1980s. No change in anthropogenic aerosols between 1987 and 2007 is detectable within the noise of the data. Even after removing the four years most heavily impacted by volcanic eruptions, the continued reduction of volcanic aerosol loads causes over half of the clear-sky direct normal irradiance increase since 1987. The remaining increase could be accounted for by a 20-year decrease in 550 nm aerosol optical depth of $.005 \pm .005$, or $6\% \pm 6\%$, but considerable statistical uncertainty exists.

CURRICULUM VITAE

NAME OF AUTHOR: Laura Riihimaki

PLACE OF BIRTH: Eugene, Oregon, USA

DATE OF BIRTH: June 30, 1979

GRADUATE AND UNDERGRADUATE SCHOOLS ATTENDED:

University of Oregon, Eugene, Oregon
Wheaton College, Wheaton, Illinois

DEGREES AWARDED:

Doctor of Philosophy, Physics, 2008, University of Oregon
Master of Science, Physics, 2004, University of Oregon
Bachelor of Science, Physics, 2001, Wheaton College

AREAS OF SPECIAL INTEREST:

Radiative impacts of aerosols and clouds
Atmospheric radiative-transfer

PROFESSIONAL EXPERIENCE:

Research assistant, Department of Physics, University of Oregon, Eugene, 2008

GK-12 fellow, GK-12 Program, University of Oregon, Eugene, 2003-2008

Teaching assistant, Department of Physics, University of Oregon, Eugene, 2002-
2003

GRANTS, AWARDS AND HONORS:

NSF GK-12 Fellowship, University of Oregon, 2003-2008

PUBLICATIONS:

Riihimaki, L. D., F. E. Vignola, and C. N. Long (2008), Analyzing increasing direct normal irradiance in Oregon for changes due to aerosols, *J. Geophys. Res.* (submitted).

Lohmann, S., L. Riihimaki, F. Vignola, and R. Meyer (2007), Trends in direct normal irradiance in Oregon: Comparison of surface measurements and ISCCP-derived irradiance, *Geophys. Res. Lett.*, *34*, L02705, doi:10.1029/2006GL027322.

ACKNOWLEDGMENTS

I wish to express my gratitude for the help and feedback of my committee. In particular, I thank Dr. Frank Vignola for the many hours he spent working with me. It was a privilege to be mentored by a scientist so committed both to quality research and meaningful applications. I also wish to thank Dr. Gregory Bothun for sharing his experience with statistical analysis and climate change, and for being my advocate with the department. In addition, I appreciate the help of Dr. James Coakley in introducing me to the theory and practice of radiative transfer, and for driving from Corvallis to be on the committee.

Many thanks to Dr. Charles Long for providing the clear-sky analysis identification program and all the time and advice that came with it.

This project was based on data collected by the University of Oregon Solar Radiation Monitoring Lab, and sincere thanks go to all those who were committed enough to the lab's goals to keep the monitoring stations running over the last 30 years, even when funding was tight. I wish to offer a special thanks to Peter Harlan, Rich Kessler, and Sara Davidson for helping with many projects and for being great people to work with.

I could not have completed my degree program without the support of the University of Oregon GK-12 program. Many thanks especially to Anae Rosenberg, Dean Livelybrooks, and Catherine Hayden for their good advice and encouragement, to my fellow graduate students in the program for creativity and friendship, and to the students

and staff of River Road, Howard, Maple, Moffitt, Delight Valley, and Sunset Elementary Schools for their enthusiasm for science.

Finally, I wish to thank the many family members and friends who have walked alongside me over the last 6 years, including Team 231, the Smurfettes, my parents and sisters, the people of Emerald Baptist and Cascade Presbyterian Churches, and the Marsh family.

For Dr. Stephen Rauseo, who taught me the value of perseverance.

TABLE OF CONTENTS

Chapter	Page
I. INTRODUCTION	1
1.1. Introduction	1
1.2. Global Dimming and Brightening	3
1.3. Causes of Regional Trends in Surface Irradiance.....	8
1.4. Examining Surface Irradiance in Oregon.....	12
II. METHOD OF MEASURING SURFACE SOLAR IRRADIANCE	16
2.1. Introduction	16
2.2. Monitoring Stations.....	18
2.3. Equipment Setup.....	20
2.4. Measurement Uncertainties	22
2.4.1. Total Horizontal Measurements	22
2.4.2. Direct Normal Measurements	25
2.4.3. Diffuse Horizontal Measurements and Calculations.....	27
2.5. Filling in Missing Data.....	29
III. DETERMINING CONSISTENT CALIBRATION NUMBERS	33
3.1. Introduction	33
3.2. NIP Calibrations	35
3.3. PSP Calibrations	39
3.3.1. Adjusting PSP Calibration Methods for Consistency	39
3.3.2. Using Adjusted Calibration Records to Find Instrument Responsivities	45

Chapter	Page
IV. ANALYSIS OF ALL-SKY IRRADIANCE MEASUREMENTS	54
4.1. Introduction	54
4.2. Method of Calculating Trends and Uncertainties	55
4.3. Trends in Direct Normal and Total Irradiance	57
4.4. Comparing Measurements to Satellite-Derived Direct Normal Irradiance	63
V. ANALYSIS OF CLEAR AND CLOUDY SKY IRRADIANCE	65
5.1. Introduction	65
5.2. Method of Detecting Clear Skies	66
5.2.1. Description of Long and Ackerman Method	67
5.2.2. Checking the Accuracy of Clear-sky Identification Using Calculated Diffuse Irradiance.....	70
5.3. Clear-sky Data Analysis	76
5.3.1. Method of Analysis	78
5.3.2. Clear-sky Results	79
5.4. Cloud Fraction Calculations	88
VI. USING RADIATIVE TRANSFER CALCULATIONS TO DISTINGUISH BETWEEN POSSIBLE CAUSES OF CLEAR-SKY IRRADIANCE CHANGES	94
6.1. Introduction	94
6.2. Description of Radiative Transfer Calculations	96
6.2.1. Integro-differential Radiative Transfer Equation	96
6.2.2. Atmospheric Inputs to the Radiative Transfer Model	98
6.2.3. Discrete Ordinate Method of Solving the Equation of Radiative Transfer	101
6.3. Aerosol Optical Depth Retrievals	104
6.3.1. Possibility of Retrieving Aerosol Optical Depths with Available Measurements.....	104
6.3.2. Daily Retrievals	108
6.4. Setting Limits on the Possible Amount of Change in Tropospheric Aerosols	115

Chapter	Page
6.5. Annual Average Calculations	122
6.6. Summary of Results	126
VII. CONCLUSIONS	128
7.1. Examining Causes of Trends in All-sky Solar Irradiance	130
7.2. Determining Changes in Aerosols between 1987 and 2007	133
APPENDICES	135
A. NIP CALIBRATION RECORDS	135
B. PSP CALIBRATION RECORDS	143
C. COMPARING AUTOMATED IDENTIFICATION OF CLEAR PERIODS TO MANUAL IDENTIFICATION USING CHARTS	155
REFERENCES	161

LIST OF FIGURES

Figure	Page
2.1. Sites in Oregon with Measurements since 1979 or Earlier	17
2.2. Components of Total Solar Irradiance	18
2.3. PSP Zenith Angle Dependence for 3 Instruments	25
2.4. Example of NIP Alignment Error	26
2.5. Measured and Calculated Diffuse Irradiance	29
2.6. Correlations between Daily Average K_t and K_b	31
2.7. Differences between Measured Daily Average Direct Normal Irradiance and that Calculated from K_t - K_b Correlations	32
3.1. Calibration Records from the Two Main NIPs Used in Eugene	36
3.2. Eugene Direct Normal Measurements at Solar Noon from Clear Days ...	37
3.3. Histogram of Ratio of Responsivities for NIPs Calibrated at Eppley and NREL	38
3.4. Histogram of Ratios of PSP Responsivities Calibrated by Eppley and NREL	43
3.5. Ratio of PSP Responsivities from Eppley Labs and NREL	44
3.6. Clear Noon Total Irradiance Values	46
3.7. Calibration Record for PSP P1	48
3.8. The Calibration History of P3	50
3.9. Eugene Normalized Clear Noon Measurements Using Annually Adjusted Responsivity Values	51
3.10. Eugene Normalized Clear Noon Measurements Using Responsivities from Calibration Events Every 2-3 Years	52
4.1. Annual Average Daily Total Horizontal Irradiance	59
4.2. Annual Average Daily Direct Normal Irradiance	60
4.3. Monthly Average Anomalies of Daily Direct Normal Irradiance	61
4.4. Seasonal Average Daily Direct Normal Irradiance	62
5.1. Daily Plot for Burns with Example of Periods Identified Clear	66
5.2. Total, Direct Normal, and Diffuse Irradiance for July 11, 2004	71
5.3. Ratio of Diffuse Irradiance to Total Irradiance Measurements	72
5.4. The Standard Deviation of the Normalized Diffuse Ratio	73

Figure	Page
5.5. Direct Normal Irradiance Measurements Identified as Clear in Eugene in 2004	74
5.6. Monthly Average Anomalies of Clear-sky Direct Normal Irradiance for Zenith Angles 65-75°	76
5.7. Monthly Average Direct Normal Irradiance from Clear Periods for Zenith Angles of 25-35°	77
5.8. Monthly Anomalies of Clear-sky Direct Normal Irradiance for Solar Zenith Angles of 65-75 Degrees	80
5.9. Example of Smoothing the Monthly Average Burns Data	83
5.10. Smoothed Monthly Average Time Series	84
5.11. Summer Averages of 5-Minute Resolution Clear-sky Direct Normal Irradiance for Zenith Angle Ranges of 65-75 Degrees	87
5.12. Histogram of Difference between Daily Average Cloud Fraction Determined Using One-Minute Measured Diffuse and Five-Minute Calculated Diffuse	89
5.13. Trends in Annual Average Daily Cloud Fraction	91
5.14. Seasonal Average Daily Cloud Fraction	92
6.1. Radiative Transfer Calculations of Direct Horizontal and Diffuse Irradiance Plotted by Zenith Angle for Three Aerosol Types	105
6.2. Modeled and Measured Direct Horizontal and Diffuse Irradiance for January 26, 2001	106
6.3. Modeled and Measured Irradiance for Clear Skies on July 1, 2001	107
6.4. Aerosol Optical Depth (550 nm) Retrievals for 3 Aerosol Types	110
6.5. AOD Retrievals as Described in Figure 6.4, but for October 1, 2001	111
6.6. Daily Average AOD Retrieved from Direct and Diffuse Irradiance	112
6.7. Correlations between AOD Retrieved from Direct and Diffuse	113
6.8. Correlations between AOD Retrieved from Direct and Diffuse Irradiance for an Aerosol Mixture of 1/3 Continental Average and 2/3 Continental Clean.....	114
6.9. Zonal Average Monthly Stratospheric Aerosol Optical Depth	116
6.10. Eugene Monthly Average Clear-sky Direct Normal Irradiance	118
6.11. Monthly Average Anomalies of Modeled and Measured Irradiance	119
6.12. Trends in Clear-sky Eugene Direct Normal Irradiance from 1987-2007 ..	121
6.13. Measured All-sky Annual Average Irradiance and Modeled Clear-sky Annual Averages.....	123

LIST OF TABLES

Table	Page
1.1. Global Dimming and Brightening Study Results	4
2.1. Missing Direct Normal Daily Averages	30
2.2. Statistical Differences between Measured and Calculated Daily Average Direct Normal Irradiance.....	32
3.1. Adjustments Made to Responsivities	45
4.1. Surface Irradiance Trends and Uncertainties	58
4.2. Surface Irradiance Trends after Removing Volcanic Years	58
5.1. Standard Deviations of Clear-sky Monthly Average Anomalies	75
5.2. Trends in Background Clear-sky Direct Normal Irradiance	81
5.3. Trends in Summer Clear-sky Direct Normal Irradiance Anomalies	87
5.4. Seasonal Bias and Standard Deviations between Cloud Fraction Determined from Calculated and Measured Diffuse	90
5.5. Cloud Fraction Trends from 1980-2007	90
6.1. Wavelength Intervals Used in the Radiative Transfer Calculations	98
6.2. Model Layers	99
6.3. Eugene Annual Average Irradiance Trends	126

CHAPTER I

INTRODUCTION

1.1. Introduction

In its 11-year cycle, the sun's irradiance varies by only a tenth of a percent [Fröhlich and Lean, 1998], corresponding to a variation of approximately 0.3 W/m^2 or less in annual average surface irradiance at any specific location. The total irradiance reaching a point on the surface of the earth at a given time, however, varies from zero to over one thousand W/m^2 . Some of that variation is caused by the calculable geometry of the earth's orbit, tilt, and rotation. But the solar irradiance at the earth's surface is also modulated by the complex elements of the atmosphere. The strongest modulators of surface irradiance are clouds. Thick clouds scatter and reflect all incoming solar radiation so that no radiation is transmitted directly through the atmosphere, but only scattered diffuse radiation reaches the surface. Various gases, including water vapor, absorb incoming radiation at specific wavelengths. Some aerosols, like soot particles, also absorb incoming radiation. The scattering of radiation from gases and aerosols attenuates the direct radiation through the atmosphere, with the direction of scattering determined

by the ratio of the size of the scattering particle to the wavelength of radiation. Thus, changes in the surface solar irradiance can tell us important information about clouds and aerosols.

While records of surface solar flux lack the spatial and temporal representation of temperature measurements worldwide, satellite and surface measurement time series are now reaching the length and spatial coverage needed to indicate climate changes. Recent reports of analyses of these measurements have indicated that the average worldwide surface solar irradiance decreased from the middle of the 20th century to about 1990, and then increased after that. The most commonly hypothesized cause for these trends is variation in the worldwide emission of anthropogenic aerosol particles. If the observed decrease in surface irradiance caused by anthropogenic aerosols is significant, then the global warming from increased greenhouse gases might be underestimated [i.e., *Pittock, 2006*].

The forcing by anthropogenic aerosols is an uncertain climate factor. The fourth Intergovernmental Panel on Climate Change (IPCC) report estimates the total anthropogenic radiative forcing of the atmosphere to be $+1.6 \text{ W/m}^2$ with an uncertainty range of $.6$ to 2.4 W/m^2 [*Solomon et al., 2007*]. Even though the fourth assessment report gives a reduced uncertainty for the forcing caused by direct ($-.9$ to $-.1 \text{ W/m}^2$) and indirect (-1.8 to $-.3 \text{ W/m}^2$) effects of anthropogenic aerosol concentrations than previous editions of the report, the summary for policy makers says aerosol forcings “remain the dominant uncertainty in radiative forcing” [*Solomon et al., 2007*]. Considering the estimated magnitude of the positive forcing of CO_2 to date is $+1.66 \text{ W/m}^2$, reducing the uncertainty

in anthropogenic aerosol radiative forcing is needed for accurate estimates of the human impact on the climate.

The University of Oregon Solar Radiation Monitoring Lab (SRML) has been measuring surface solar irradiance in the Northwest since 1975. Simultaneous measurements of direct normal and total irradiance are available with five-minute resolution for three ground sites beginning in 1980 or earlier. These measurements show a 1-2% increase per decade in annual averages of total irradiance, and a 4-5% increase per decade in direct normal irradiance. Cloudy and clear-sky measurements were separated to investigate the causes of the trends. The clear-sky data was analyzed specifically to determine whether the trends are caused by aerosol changes, as hypothesized for other regions.

1.2. Global Dimming and Brightening

A number of others have investigated both regional and worldwide trends in shortwave surface irradiance. Table 1.1 shows a summary of the results of several studies that sought to quantify worldwide trends in surface solar irradiance. From about 1960 to 1990, trend analyses of surface solar irradiance measurements from ground-based networks around the world show a negative trend. This decrease has been named “global dimming.” (The word “global” in global dimming initially referred to the type of measurement--global irradiance, the total irradiance on a horizontal surface. This has

become confused, however, and is now also used to mean “worldwide” dimming.) After 1990, analyses of both ground-based and satellite-derived measurements indicate a positive trend in surface solar irradiance, or “global brightening.” The most commonly hypothesized cause for the “dimming and brightening” is changing anthropogenic aerosols. This section describes these studies in more detail.

Table 1.1. Global dimming and brightening study results

Study	Dates of study	Change per Decade	W/m² per Decade	Location	Data Source
<i>Gilgen et al., 1998</i>	1950-1990 (most >1965)	-2%		Worldwide	GEBA
<i>Stanhill and Cohen, 2001</i>	1950-2000	-2.7%	-5.1	Worldwide	GEBA, regional studies
<i>Liepert, 2002</i>	1961-1990	-1.4%	-2.3	Worldwide	GEBA
	1961-1990	-3.5%	-6.33	USA	NSRDB
<i>Alpert et al., 2005</i>	1964-1989		-4.1	Highly populated	GEBA
	1964-1989		-1.6	Sparsely populated	GEBA
<i>Wild et al., 2005</i>	1992-2001		+6.6	World	BSRN
<i>Pinker et al., 2005</i>	1983-2001	+1.0%	+1.6	World	GEWEX SRB

Three studies summarizing worldwide findings found decreases in surface irradiance of 1.4-2.7% per decade until around 1990 [Gilgen *et al.*, 1998; Stanhill and Cohen, 2001; Liepert, 2002]. Each of these studies analyzed monthly average surface flux records from ground networks of radiometers. All three studies used data from the Global Energy Balance Archive (GEBA) archived by the Swiss Federal Institute of Technology. The GEBA gathers data from monitoring networks around the world run by various organizations. This is the most comprehensive dataset for surface flux measurements before 1990. A careful quality control process identifies large errors [Gilgen *et al.*, 1998; Gilgen and Ohmura, 1999]. However, because the GEBA only archives the data and is not responsible for its collection, there is limited information available to detect systematic errors. Gilgen *et al.* [1998] used a study of independent measurements at the same location to estimate uncertainties in monthly averages at 5% and annual averages at 2%. Besides the data from the GEBA network, Liepert [2002] analyzed data from the National Solar Radiation Data Base (NSRDB), which contains measured and modeled surface data from around the United States. The NSRDB shows an even stronger decrease of 3.5% per decade over the US than the worldwide trend. This dataset also has larger uncertainties than GEBA on the order of 9% [Maxwell *et al.*, 1995] because, although some of the data are measured, much is modeled from parameterizations with cloud cover.

Two recent papers in *Science* reported on “global brightening” in the 10-15 years preceding 2001. Wild *et al.* [2005] examines ground-based measurements from the Baseline Surface Radiation Network (BSRN) beginning in 1992. Responding to the need

for more consistent measurements worldwide, the BSRN was formed with a goal of representative worldwide coverage and uniform data collection protocol. BSRN sites increase by 6.6 W/m^2 in the decade of study, though this time period is too short to determine a significant trend of that magnitude. GEBA data is also analyzed, and similarly finds positive trends since 1990. Satellite-derived estimates of surface irradiance were used in a study by *Pinker et al.* [2005] which also found a “global brightening” of 1.0% per decade from 1983 to 2001. The data used in the study models surface irradiance using the International Satellite Cloud Climatology Project (ISCCP) quantification of clouds. ISCCP uses geostationary and polar orbiting satellites to create a gridded dataset of cloud properties with the longest time period possible for worldwide coverage.

A number of causes have been considered to explain the worldwide dimming and following brightening, but the most commonly suggested is a change in anthropogenic aerosols. Some have also questioned whether the observed trends are related to significant atmospheric changes. One concern is the influence of calibration errors on the measurements. The instruments used to measure irradiance decline in sensitivity over time with exposure to radiation [i.e., *Wilcox et al.*, 2001]. Thus, regular calibrations are necessary in order to determine trends in the data. Acceptable calibration procedures are defined for BSRN monitoring stations. With the GEBA data, however, different networks handled calibrations individually. The positive trend in GEBA data since 1990 is evidence that trends are not caused by sensor degradation as sensor degradation can only cause a decrease.

The statistical significance of the trends has also been questioned. Besides the impact of the variability of the data, *Weatherhead et al.* [1998] quantified the impact of auto-correlation on the number of years necessary to find a statistically significant trend. The uncertainty of a fit to data is determined by normalizing the statistical variations around that trend by the number of degrees of freedom. With independent measurements, the degrees of freedom of the variations are the number of measurements used in the fit minus two. Auto-correlation between successive time steps means that the number of degrees of freedom is reduced because non-independent measurements do not contain as much information (Halstead Harrison, personal communication). *Hinkelman et al.* [2006] used the satellite-derived data set of the GEWEX-SRB along with the *Weatherhead et al.* [1998] statistical calculations to determine that more years are required to determine a significant trend of the size seen in worldwide datasets. This may not be the case for regional studies, however, where trends are stronger relative to the variability.

Despite concerns, the hypothesis that anthropogenic aerosol emissions caused the observed trends has been supported by a variety of studies. *Alpert et al.* [2005] analyzed GEBA irradiance measurements in relation to the proximity of the measurement sites to cities with population greater than 0.1 million. Population was thus used as a proxy for anthropogenic aerosol production. From 1969-1989, the average of the highly populated sites decreased at a rate of 4.1 W/m^2 per decade, while the sparsely populated sites (population less than 0.1 million) decreased at a rate of 1.6 W/m^2 per decade. *Streets et al.* [2006] calculated the total emissions of anthropogenic black carbon and SO_2 aerosols from multiple sources globally. The calculated emissions agree with the hypothesis of a

worldwide increase in global aerosol optical depth from 1982 until 1989, followed by a decrease of 550 nm aerosol optical depth from 0.108 to 0.105 (a change of 0.003) between 1988 and 2000. These changes in anthropogenic aerosols are related primarily to clean air regulations in Europe and the United States as well as changes in economic activity in Eastern Europe, the former USSR, and China. *Mischenko et al.* [2007] analyzed the average aerosol optical thickness over the oceans derived from the Advanced Very High Resolution Radiometer (AVHRR) radiance satellite record. They find a 0.03 decrease in the aerosol optical depth at a wavelength of 550 nm between 1991-2005 that is statistically significant at the 99% confidence level. Note that this aerosol optical depth change is an order of magnitude higher than that estimated by *Streets et al.* [2006] over a similar time period. The accuracy of this, surprisingly large (20%) decrease in aerosol optical depth has been questioned due to the difficulty of retrieving aerosol optical depths from AVHRR measurements.

1.3. Causes of Regional Trends in Surface Irradiance

While the previously mentioned studies describe a worldwide trend in anthropogenic aerosols, such aerosols come from localized sources and thus ought to have regionally specific impacts. As in the previously described study by *Alpert et al.* [2005], some regional studies show variation that supports the hypothesis that dimming is stronger in regions with higher anthropogenic aerosol loads. Also of note is that both

remote regions and regions with high aerosol loads have reported a “brightening” or recovery of surface irradiance since the 1990s. Some regional studies also show changes in cloud cover that impact the all-sky trends. Thus, as the following examples show, regional studies are needed to better sort out the underlying causes and complexity of aerosol and surface irradiance changes.

The *Alpert et al.* [2005] finding that sparsely populated areas have little or no dimming agreed with atmospheric transmission measured at the remote location of the European Southern Observatory in Chile [*Schwartz, 2005*]. *Schwartz* found that between 1978 and 1997 the only atmospheric dimming in that period is due to the volcanic eruptions of El Chichón and Mt. Pinatubo. The average transmission in years not affected by these volcanic eruptions (1978-1981, 1985-1990, 1996-1997) stayed constant over the whole time period. *Schwartz* also looked at transmission data from Mauna Loa, Hawaii in non-volcanic periods and likewise finds no significant change. This study ends in 1997, however, and it would be interesting to know how the transmission at this remote site has changed since then as a “brightening” might not have been detectable by 1997.

An example of dimming caused by a regional increase in anthropogenic aerosols can be seen in China. With increased industrial activity in China in recent years, an increase in anthropogenic aerosols is expected that should reduce the surface irradiance. A decrease of 4.5 W/m^2 per decade was found in China from 1960 to 2000, accompanied by a decrease in direct irradiance and increase in diffuse irradiance for the same time period [*Che et al.*, 2005]. These results are fairly consistent regionally, with 90% of the 64 stations analyzed showing a decrease in total irradiance. Interestingly, the direct

radiative impact of the increase in pollutants is high enough to counter the opposing decrease in cloud cover over the same period [*Qian et al.*, 2006]. *Qian et al.* also found that although emissions of pollutants have been continuously increasing in China, the total irradiance matched worldwide claims of dimming until 1990 followed by at least a partial recovery or brightening.

The behavior of dimming and then brightening also fits with analysis of three remote NOAA GMD sites between 1977-2004 [*Dutton et al.*, 2006]. Data from Mauna Loa and American Samoa in the Pacific Ocean, the South Pole and Boulder, Colorado all support the “dimming” and then “brightening” seen in other studies [e.g., *Wild et al.*, 2005]. The Barrow, Alaska site, however, declined for the entire 27-year record. The existence of the reverse to brightening at these remote sites as well as the industrial sites in China is an interesting similarity if these changes are indeed caused by anthropogenic aerosols.

The study by *Liepert and Kukla* [1997] gives us another example of irradiance under cloudy and clear-sky conditions changing differently. They describe the change in both clear and cloudy skies from measurements at eight German monitoring stations between 1960 and 1990. At high zenith angles, there was a decrease in clear-sky solar surface irradiance. However, at low zenith angles, clear-sky irradiance showed a slight increase. The authors suggested that the lessening of aerosols after volcanic eruptions combined with increased urban aerosols may have caused these clear-sky trends as well as the positive trend in horizontal visibility. In addition to clear-sky trends, *Liepert and Kukla* [1997] reported a decrease in the total solar radiation under completely overcast

skies. Because cloud fraction and sunshine duration did not change over the period of time, the decrease is hypothesized to come from a decrease in cloud transmissivity or an increase in multi-level cloudiness. These effects combined to give an overall decrease in all-sky condition surface solar irradiance.

While there is evidence that anthropogenic aerosols cause surface solar irradiance trends, these regional studies illustrate the complexities that still need to be understood to verify that link. The trends themselves still have high uncertainties, as the spatial and temporal representation of the data worldwide is only just sufficient to determine statistical significance. There is a change to “brightening” in the last decade in both industrial areas like the Chinese monitoring sites and remote sites like those on Mauna Loa and the South Pole. This consistency between very different sites suggests a change with worldwide impact, or several simultaneous changes that cause brightening in multiple regions. Yet there is some evidence that the “dimming” seen until 1990 is seen in areas near industrial activity, but not in remote areas. The change in surface irradiance in some regions has been attributed to changes in cloudiness rather than aerosol changes (though clouds are also impacted by increased aerosols). Natural aerosols from volcanic eruptions also impact surface irradiances significantly, and in fact are the only aerosol impact seen in studies like that of the transmission about the European Southern Observatory in Chile [*Schwartz, 2005*]. Worldwide averages of surface solar irradiance show a dimming from 1960-1990 followed by a brightening until the present. And worldwide studies of average anthropogenic aerosols show changes that are consistent with the possibility that anthropogenic aerosols caused those trends in surface irradiance.

Measurement uncertainties, complex regional behavior in response to aerosols, and changes in clouds and volcanic aerosols, however, all still leave room for other explanations for the changes in surface irradiance.

1.4. Examining Surface Irradiance in Oregon

If anthropogenic aerosols have only local impacts, the University of Oregon Solar Radiation Monitoring Lab (SRML) data set can only answer questions about aerosol changes regionally and not worldwide changes. If the dimming and brightening observed around the world comes from a global change in aerosols, then the UO SRML data is well suited to investigate the impact of changes in aerosols on surface solar irradiance because of the quality and length of simultaneous measurements of total and direct normal irradiance. Direct normal irradiance measures the amount of radiation that passes directly through the atmosphere (and the small portion of diffuse light that is scattered in the direction of the beam). Total irradiance, on the other hand, measures both the direct beam and the diffuse, or scattered radiation. The direct normal irradiance is, therefore, a much more sensitive indicator of the presence of aerosols than total irradiance. It is rare to have a high-quality direct normal time-series of the length available from the SRML.

Trend lines fit to both direct normal and total surface irradiance are positive at all three sites in Oregon since 1980 or earlier. The all-sky annual averages of direct normal irradiance increase by 4-5% per decade and the total irradiance by 1-2% per decade over

the time period. Clear-sky data shows that a large part of this trend is the result of the changes in stratospheric aerosol concentrations due to volcanic aerosols. At the peak of the Mt. Pinatubo eruptions, for example, the stratospheric aerosols reduce monthly average clear-sky direct normal measurements at high zenith angles up to 200 W/m^2 or over 25%. An increase in clear-sky direct normal radiation since 1987 may have been caused by aerosol concentration changes, though caused by anthropogenic aerosols can be detected since 1987. The trends seen in both direct normal and total irradiance are impacted by low irradiance values before 1982 that could be caused by high aerosol loads. Changes in cloudiness could also cause part of the trend, though the analysis done here is not sufficient to determine the magnitude of those changes. The analysis is organized as follows:

Chapter II describes the setup of the instruments used to measure the solar irradiance. An analysis of the uncertainties in the measurements is also included. A description is given of how missing data is filled in with measurements from other instruments to make the data set as complete as possible.

The consistency of the measurements over the long record is of particular interest in this study. Thus, Chapter III describes the careful work done examining calibration records to assure that observed trends are not due to instrument changes. The sensitivity of thermopile instruments is known to change over time as the coating of the thermopile ages from exposure to UV light. Using calibration records and measurements from clear periods, responsivity values (calibration numbers) are adjusted to ensure the consistency of the time-series.

In Chapter IV, the all-sky data is examined for trends. Monthly and annual averages are fitted using linear regression lines. Statistical significance levels of the trends are found including the impact of auto-correlation. Trends in seasonal slices of the data are also analyzed for multi-decadal changes. Finally, a study comparing these direct normal time-series to satellite-derived fluxes for large boxes is referenced to show that these sites represent a regional trend [*Lohmann et al.*, 2007].

Measurements are screened for clouds, and clear-sky periods are used to better understand the causes of the increase in surface solar irradiance. This process is discussed in Chapter V, along with analysis of clear and cloudy periods. The identification of clear skies was done in collaboration with Dr. Charles Long, using a well-developed algorithm that identifies clear skies from total and diffuse measurements. The program identifies clear skies, gives estimated clear-sky values for all time periods by empirically fitting clear data, and calculates an estimated cloud fraction using that information [*Long and Ackerman*, 2000; *Long et al.*, 1999]. Chapter V includes a discussion of the accuracy of this method using diffuse irradiance values calculated from total and direct normal measurements. The cloud-free direct normal measurements are then analyzed for trends at high zenith angles. Cloudy-sky irradiance measurements are also analyzed for changes in cloud-fraction.

Chapter VI describes the radiative transfer calculations used to determine what changes in aerosol optical depths (AODs) would cause the change seen in irradiance. Atmospheric data, including water vapor profiles, are taken from the NCEP reanalysis to use in the calculations [*Kalnay et al.*, 1996]. Aerosol properties were taken from the

OPAC model for several typical aerosol mixes [*Hess et al.*, 1998]. Measured diffuse irradiance available in Eugene in recent years was used along with direct normal irradiance measurements to determine the absorption properties and average aerosol optical depth of the background tropospheric aerosols in Eugene. The stratospheric aerosol optical depth data set described by *Sato et al.* [1993] was used to calculate the impact of volcanic aerosols on the clear-sky direct normal irradiance. This analysis showed that even after removing the 4 years most heavily impacted by Pinatubo aerosols, over half of the observed trend from 1987 to 2007 in clear-sky direct normal irradiance was caused by a continuing reduction of stratospheric aerosols following the eruption.

Chapter VII gives a summary of conclusions found in the study.

CHAPTER II

METHOD OF MEASURING SURFACE SOLAR IRRADIANCE

2.1. Introduction

The University of Oregon Solar Radiation Monitoring Lab (SRML) has been operating solar radiation monitoring stations around the Northwest since the mid-1970s. This unusually long direct normal data record from high quality instruments is a valuable resource for studying aerosol changes. The three stations with the longest records are located in Eugene, Hermiston, and Burns. These stations, shown in Figure 2.1, have irradiance measurements at five-minute intervals from 1979 or earlier. Both total irradiance and direct normal irradiance measurements are made with thermopile-based radiometers. The records are continuous except for a gap in Hermiston from 1990 through 1992 when the station was closed.

The three components of broadband solar radiation measured at the surface are direct, diffuse, and total irradiance. Only two of these are independent. Figure 2.2 shows how the total solar irradiance can be broken into direct and diffuse components.

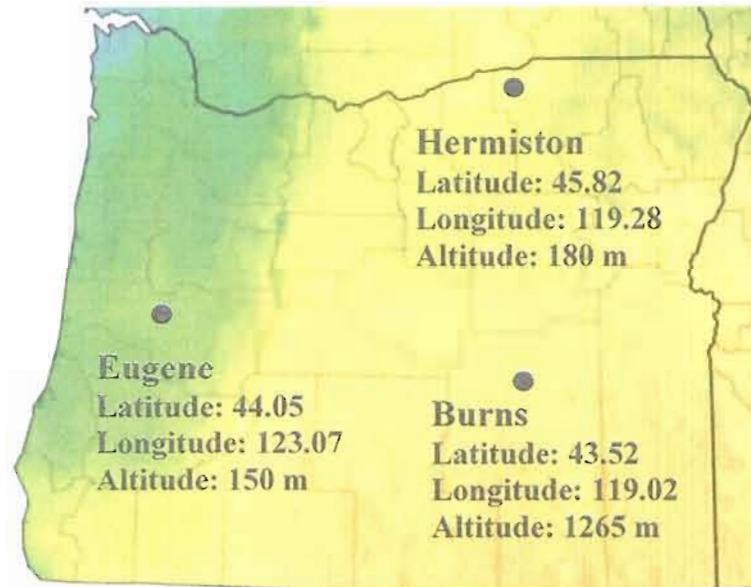


Figure 2.1. Sites in Oregon with measurements since 1979 or earlier.

Measuring any two of these components allows calculation of the third. At the UO SRML, the direct flux is measured normal to the incoming radiation. This direct normal irradiance can be projected onto the horizontal by multiplying the flux by the cosine of the solar zenith angle, giving direct horizontal irradiance. Total and diffuse irradiance are measured or calculated by the UO SRML on a horizontal plane, that is, the flux passing through a surface parallel to the surface of the earth. Total horizontal irradiance is measured at all three sites, and diffuse horizontal irradiance is calculated by subtracting the direct horizontal irradiance from the total horizontal irradiance. Diffuse measurements are available in Eugene from 1997 to the present.

This chapter describes the locations of the three stations, the setup of the monitoring equipment, and the uncertainties of the measurements used.

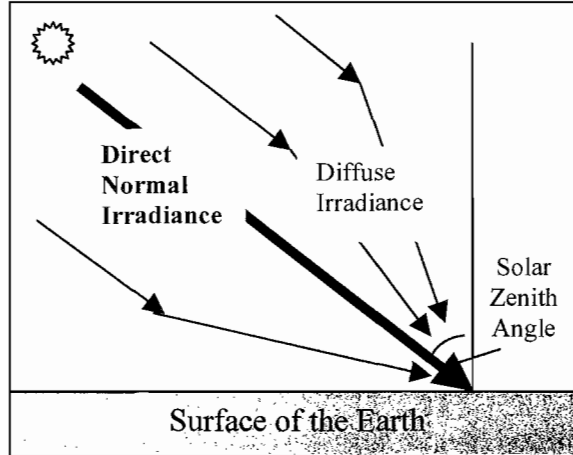


Figure 2.2. Components of total solar irradiance.

2.2. Monitoring Stations

The three sites used in this study are shown in Figure 2.1. The color variation in the map shows average annual direct normal irradiance throughout the state derived from satellite measurements [Vignola and Perez, 2004]. The three sites are located in different climate zones. Eugene is in the Willamette Valley, with its higher precipitation and cloudiness. Hermiston is located along the Columbia River, also at a low altitude like Eugene, but surrounded by a much drier climate. Burns is located in Eastern Oregon on a high desert plateau.

The Eugene station is located on the University of Oregon campus on the roof of Pacific Hall. The Eugene station is the reference station for the network and so has more meteorological and irradiance measurements than the other stations. In 1997, a fully automatic tracker was installed in Eugene allowing better measurements of diffuse

irradiance and eliminating the need for frequent manual adjustments to the direct normal alignment. Since 2000, one-minute resolution data has been recorded in Eugene for some of the measurements along with five-minute data. The availability of one-minute measured diffuse data is useful in checking the accuracy of the clear-sky identification described in Chapter V.

The Hermiston station is located at the Hermiston Agricultural Research and Extension Center run by Oregon State University. The station is located in an important agricultural region, and is surrounded by research fields. Besides the total and direct normal irradiance measurements, the station has a Rotating Shadowband Pyranometer, added in 1995, that measures broadband total, direct and diffuse irradiance. These additional measurements are helpful in filling in missing data in the thermopile measurements. The site is co-located with an AgriMet station (part of the Pacific Northwest Cooperative Agricultural Weather Network), which has measured meteorological variables like temperature, relative humidity, wind speed and others since 1993.

Burns has a much higher altitude than the other stations. The monitoring equipment is currently located at the Eastern Oregon Agricultural Research Center, where it was moved in April of 1982. Earlier than that time the site was located in downtown Burns (lat. 43.58, long. 119.05, alt 1295 m). The location receives a substantial amount of solar irradiance each year as shown by the coloring in Figure 2.1. Temperature is the only measurement made at Burns besides total and direct normal irradiance.

2.3. Equipment Setup

Total horizontal and direct normal irradiance are measured with thermopile-based instruments that convert incident solar radiation into a voltage. Total irradiance is measured with Eppley Precision Spectral Pyranometers (PSPs). Direct normal irradiance is measured with Eppley Normal Incident Pyrheliometers (NIPs) mounted on trackers so that the instrument is always pointing in the direction of incident radiation. In both the PSP and NIP, a wire-wound thermopile measures the temperature difference between a coated sensor disk that absorbs solar radiation and an instrument body that acts as a heat sink. Domes on the PSPs and windows on the NIPs protect the sensors and act as spectral filters, blocking longwave radiation. The voltage produced by that thermopile is measured and converted into irradiance (W/m^2) by calibration against a known reference.

Two data logging systems have been used at the UO SRML to record the voltage output from the radiometers. Since 1995, data have been recorded with Campbell Scientific CR-10 or CR-10X data loggers, and then transferred by modem to the UO SRML database. These data loggers have an accuracy of .3%. Before 1995, a data logging system created by the SRML and electronics shop was used. This system consisted of “pods” that charged capacitors from the voltage output of the instrument and then emitted pulses after a certain cumulative voltage was reached. The pulses were then transmitted to a data logger and recorded on back up tapes. The pods were calibrated in the shop with an offset and multiplicative factor, and are estimated to have an uncertainty of .5%. In addition to data loggers, continuously plotted charts are used as backup. This

was particularly important with the old data logging system when the charts were used to fill in missing data.

The data are recorded in five-minute integrated measurements. Before the change in data loggers, the data was only processed at hourly intervals. This included putting the data into ASCII text files and manually inspecting the data for errors. In order to separate the data into clear and cloudy periods as described in Chapter V, 5-minute or shorter time resolution is needed. Thus, raw data from 5-minute files were put into ASCII text files. This required reading data from several data formats and media. Manually inspecting and correcting all of this data was not possible. Instead, the data quality flags from the hourly files were transferred to the 5-minute files and data labeled as bad in the hourly files were eliminated from the 5-minute files. The back-up methods for the old data logging system were only available at hourly time periods, thus there are some periods that are missing in the 5-minute data but complete in hourly files. Because the hourly data was more thoroughly checked and complete, it was used for the all-sky studies in Chapter IV, when short time resolution was not as important.

In addition to the data logger change, two other changes have been made to the equipment setup. Around the same time as the systems were switched to Campbell Scientific data loggers, ventilators were installed around the PSPs. The ventilators blow air around the domes of the PSPs to help keep snow and rain from collecting on the instruments. The primary impact of the ventilators is to make the dataset more complete in the later years than the earlier years. Another change made in Eugene was an update in 1997 to a fully automatic sun tracker that holds the NIP. Each NIP must be mounted on a

tracker that moves with the sun allowing continuous readings. In the years from 1978 to 1997 at Eugene and all years at Burns and Hermiston, the NIPs were mounted on clock-driven Eppley Solar trackers. These trackers move automatically during the day to follow the path of the sun, but must be manually adjusted for changes in declination and solar time. When the trackers are not adjusted frequently enough because of the absence of station operators or when the weather is too cloudy to align the trackers properly, the measured direct normal irradiance values are too low. Low values are visible upon manual inspection of the data, and bad data is eliminated or corrected. The fully automatic tracker in Eugene adjusts to both time of day and declination and so is much less likely to cause an alignment error in the data. Thus, the Eugene direct normal measurements after 1997 are more complete than earlier records.

2.4. Measurement Uncertainties

2.4.1. Total Horizontal Measurements

Total irradiance is measured with Eppley Precision Spectral Pyranometers (PSPs), which have a calibration accuracy of 3-4%. The uncertainty comes primarily from nonlinearities in zenith angle dependence (cosine response). A difficulty in using these pyranometers to measure trends is the drift of the instrument calibration over time. With increasing exposure to sunlight, the coating on the surface of the thermopile degrades and

the instrument becomes less sensitive to incident radiation. Periodic calibrations are used to adjust for this degradation as described in Chapter III.

One of the largest sources of uncertainty in PSPs is the thermal offset error, also called IR loss or re-radiation effect. A study by *Bush et al.* [2000] showed that differences between the temperature of the PSP detector and the temperature of the outer dome caused thermal offset errors proportional to the difference of the fourth power of the two temperatures. The dome temperature equilibrates with the sky temperature. On clear days, the sensor radiates to a cold sky via the dome, leading to a measurement error caused by the ambient IR radiation. Thus, depending on environmental conditions, unequal blackbody radiation between the detector and surrounding dome can cause measurement offsets of up to about 25 W/m^2 or 3-6% for total irradiance measurements on clear days. These offsets also show up at night as negative values of irradiance when the warmer detector radiates to the cooler dome. In order to correct some of the thermal offset error, the UO SRML adds these nighttime values to the daily measurements. This only corrects about one-fourth to one-half of the IR loss during daylight hours. Corrections for the thermal offset error have been developed using measurements of IR radiation. The corrections cannot be used at these sites, however, as no IR measurements are available.

The cosine response of the PSP is at least in part due to the thermal offset effect. As a rough estimate, consider an equal offset during the day of 10 W/m^2 . At zenith angles below 30 degrees, the total irradiance reaches values on the order of 1000 W/m^2 , leading to a percentage error of only 1%. At high zenith angles of around 70 degrees, the clear-

sky total irradiance is as low as 300 W/m^2 , so a 10 W/m^2 offset causes an error of over 3%. Because the thermal offset depends on the atmospheric conditions of the day, the cosine response also depends on the atmospheric conditions.

The cosine response also depends on the particular instrument, as shown by calibrations in Eugene of three different PSPs done at the same time during the summer of 2006 (Figure 2.3). The instruments are calibrated against a reference total irradiance found by summing measured direct horizontal and diffuse irradiance. Each data point is the average ratio of the PSP measurement to the reference irradiance for a 10° zenith angle bin. Error bars are plotted for two standard deviations of the zenith angle bin. The ratios change by 7-10% between zenith angles of 20° and 70° (5-7% between zenith angles of 20° to 60°). The cosine responses of the three instruments are within 1% of each other up to zenith angles of 60° , then differ at large zenith angles.

The UO SRML uses the convention of calibrating PSPs at a solar zenith angle of 45° according to the method used by the National Renewable Energy Lab. Individual measurements at other zenith angles will have errors up to 7-8% at high zenith angles, but much of that error averages out in daily totals. Similarly, using annual averages to compute trends makes the seasonal zenith angle variation less important. If the instruments have been regularly calibrated, the relative uncertainties in annual averages of total irradiance measured with thermopile pyranometers is generally considered to be on the order of 1.5% [i.e. *Dutton et al.*, 2006] to 2% [*Gilgen et al.*, 1998].

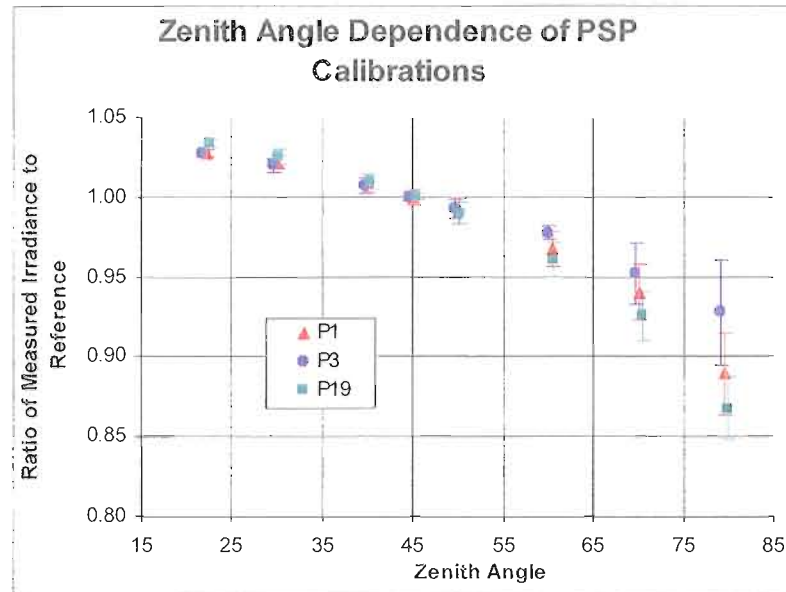


Figure 2.3. PSP zenith angle dependence for 3 instruments during the same calibration event in Eugene. Averages of 10° zenith angle bins are plotted, with error bars determined by 2 standard deviations from the mean. The reference total irradiance is the sum of diffuse and direct measurements.

2.4.2. Direct Normal Measurements

Eppley Normal Incidence Pyrheliometers (NIPs), have absolute calibration accuracies around 2% and do not degrade significantly over time. Calibrations can be done directly against an absolute cavity radiometer with an absolute accuracy of 1.5% or less at a 95% confidence level.

Direct normal measurements made with an Eppley NIP have an uncertainty in the field of about 2-3%. Because the pyrheliometer tracks the sun during the day, zenith angle responses are not as important. The impact of the environmental conditions on the

performance of the instrument is smaller than the thermal offset found in PSPs. *Vignola and Reda* [1998] found a 0.5% variation in responsivity for a temperature range of 5°C to 45°C. Wilcox, Hickey, and Myers (Environmental Effects on the Eppley Normal Incidence Pyrheliometer Draft research summary, 2005) found a 1.5% variation in responsivity depending on the environmental factors of wind speed, direct beam irradiance, and temperature combined.

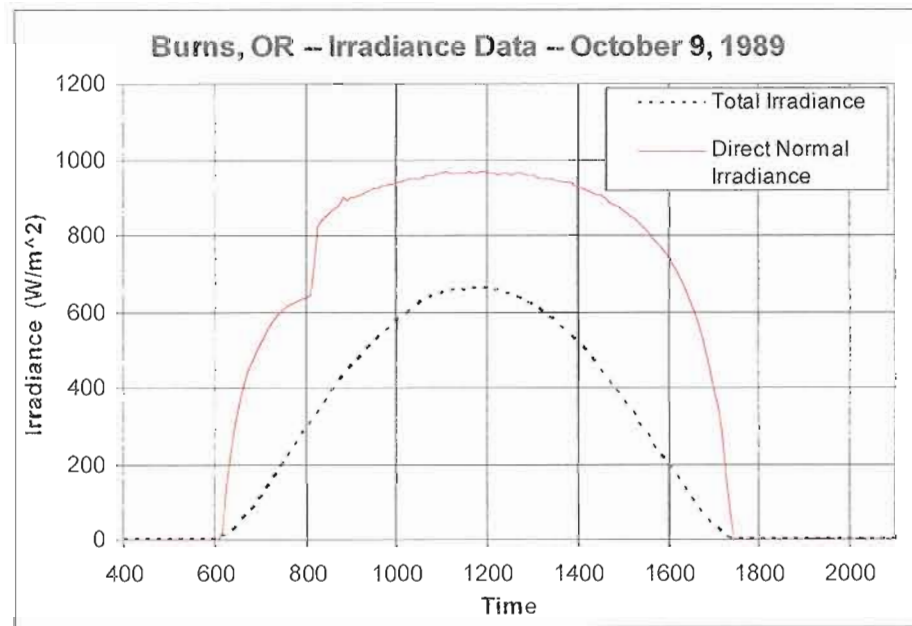


Figure 2.4. Example of NIP alignment error. The NIP was realigned just after 8:00. Note the low values before the alignment.

The additional uncertainty in the field comes primarily from alignment errors. As seen in Figure 2.4, irradiance measurements are too low when a NIP is improperly aligned. The figure shows an extreme example, but alignment errors as low as 1-2% can be seen in chart records. Personnel from the UO SRML manually inspect data, and these bad data are removed. Only errors in alignment below 1-2% are undetectable and thus

contribute to the uncertainty of the measurements. The missing data, however, leave gaps that can cause uncertainties in the long-term averages produced from the data set.

2.4.3. Diffuse Horizontal Measurements and Calculations

It is difficult to characterize the accuracy of diffuse measurements because there is no absolute standard of diffuse irradiance. Diffuse measurements made with a black and white type pyranometer are generally considered to be the most accurate [see for example, *Dutton et al.*, 2001]. Diffuse measurements are made by shading a pyranometer with a sun-tracking disc. If a PSP is used as the shaded pyranometer, the thermal offset of up to 20 W/m^2 can introduce an error of up to 40% in clear-sky diffuse measurements. In black and white type pyranometers, the difference between the temperature of the black and white painted sections of the sensor are used to determine the irradiance. As both sections are in the same thermal environment, the error caused by the IR radiation of the sensor to the sky is an order of magnitude smaller than that of the PSP sensor. Black and white type pyranometers have other uncertainties like spectral response, slower time response, uneven cosine and azimuthal response that make them poor choices for total irradiance measurements. However, the nature of diffuse radiation reduces the impact of these errors. For example, diffuse radiation comes from all directions without the strong peak of radiation from the direct beam, thus the impact of uneven cosine and azimuthal angular response is greatly reduced. Uncertainties in diffuse irradiance measured with a

black and white type pyranometer are estimated to be on the order of 3% or 5 W/m² [Dutton *et al.*, 2001].

Eugene has diffuse measurements made with a Schenk black and white type pyranometer starting in 2000. For longer records of diffuse irradiance in Eugene, and for diffuse irradiance at Burns and Hermiston, diffuse irradiance is calculated from total and direct normal measurements. The diffuse is calculated using the following equation:

$I_{dif} = I_{total} - I_{dn} \cos\theta$, where θ is the solar zenith angle and I_{dn} is the direct normal irradiance. The cosine response error of the total irradiance translates into a larger percentage error in the diffuse because the diffuse irradiance is calculated as a difference. That is, a 10 W/m² error in total irradiance is still a 10 W/m² error in the diffuse irradiance. However, instead of being a 1-3% error in the total irradiance, 10 W/m² is an error of 10% or higher in the diffuse irradiance. This leads to a systematic difference in the shape of the calculated diffuse irradiance over the day compared to the measured diffuse. This systematic error is visible on a clear day in Eugene (see Figure 2.5). The calculated diffuse is more than 20 W/m² high around noon, but in the morning and afternoon is up to 20 W/m² low. Much of this error averages out over the day, though the calculated diffuse is significantly affected on a short time interval by the cosine response of the pyranometer. The calculated diffuse is shown to be accurate enough to detect clear-skies as described in Chapter V. The error is too large, however, to use the calculated diffuse in the retrieval of aerosol optical depths (Chapter VI).

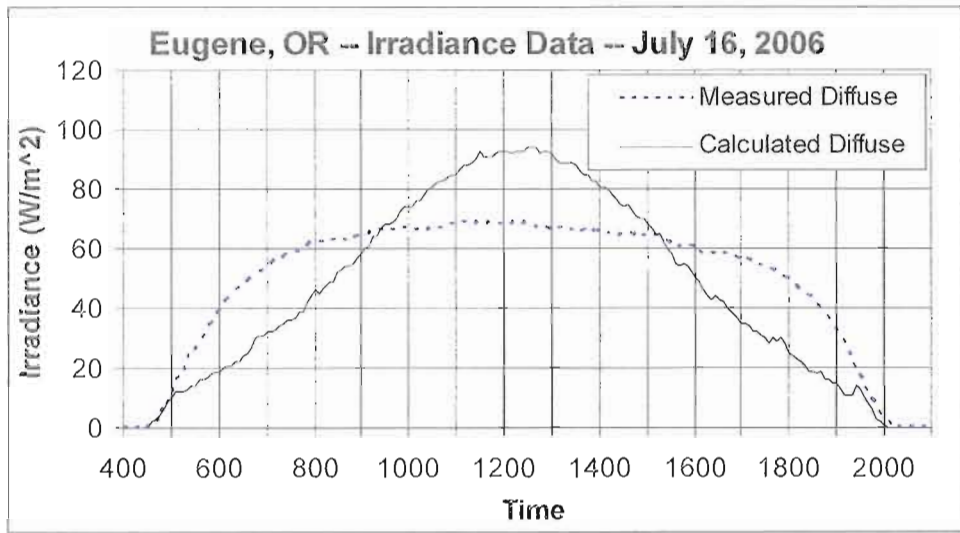


Figure 2.5. Measured and calculated diffuse irradiance on a clear day in Eugene.

2.5. Filling in Missing Data

As discussed in Section 2.4, some direct normal irradiance measurements are missing because of alignment errors. The first row of Table 2.1 shows the percentage of missing daily averages in the direct normal data set at each site. The monthly and annual averages used in the trends in Chapter IV are calculated from daily averages. In order to minimize any bias in those trends due to unequal sampling, most of the missing daily averages are filled in with measurements from other instruments.

The UO SRML has operated a Rotating Shadowband Pyranometer (RSP) in Hermiston since 1995. The RSP uses a solar cell based pyranometer to measure total and diffuse irradiance using a shadowband that shades the instrument once each minute.

Direct normal irradiance is then calculated from these two measurements. While the accuracy of this instrument is not as high as that of the thermopile instruments, corrections have been developed that correct the irradiance to within 1-3% of direct normal measurements made with an Eppley NIP between zenith angles of 20 and 75 degrees [Vignola, 2006]. Row two of Table 2.1 gives the percentage of missing daily averages filled with this method.

Table 2.1. Missing direct normal daily averages

	Hermiston	Burns	Eugene
Missing days	13.8%	11.1%	1.6%
Days filled with RSP	4.8%		
Days filled with PSP correlation	8.2%	9.9%	1.4%
Unfilled missing days	0.8%	1.2%	0.3%

Missing daily averages of direct normal irradiance are also filled using correlations between total and direct normal irradiance measurements. Correlations are calculated from daily averages normalized by the solar irradiance at the top of the atmosphere. The normalized direct normal irradiance (K_b) is equivalent to the atmospheric transmission. The normalized total irradiance (K_t), or clearness index, is equal to the total horizontal irradiance at the surface divided by the top of atmosphere solar irradiance on a horizontal surface. K_b is calculated as a cubic function of K_t plus a seasonal term as in the study by Vignola and McDaniels [1986]:

$$K_b = a_0 + a_1K_t + a_2K_t^2 + a_3K_t^3 + (a_4K_t + a_5K_t^2)\sin(2\pi(N - 20)/365), \quad (\text{Eq. 2.1})$$

where N is the day of the year. New coefficients were calculated for each site from every two years of data using least-squares regression fits. The two-year calculation was found to reduce biases due to changing aerosol concentrations and instruments. Figure 2.6 shows daily values of K_t versus K_b for each site from 2002-2007 in black \times 's. The gray regions in the center of each graph show the K_b values calculated from K_t . Differences between measured and calculated daily averages for the same years (2002-2007) are plotted in Figure 2.7. Table 2.2 gives statistics for the difference between measured and calculated daily averages for the years 2002-2007 at each site. The fit is fairly good with a mean bias error less than 1% and a standard deviation of 13-16%. Most of the remaining gaps in daily average direct normal irradiance were filled using this method as shown in (row 3 of Table 2.1). Excluding the two years when Hermiston was not operating, less than 1.6% of the daily averages at each site remained unfilled in calculating the monthly and annual averages.

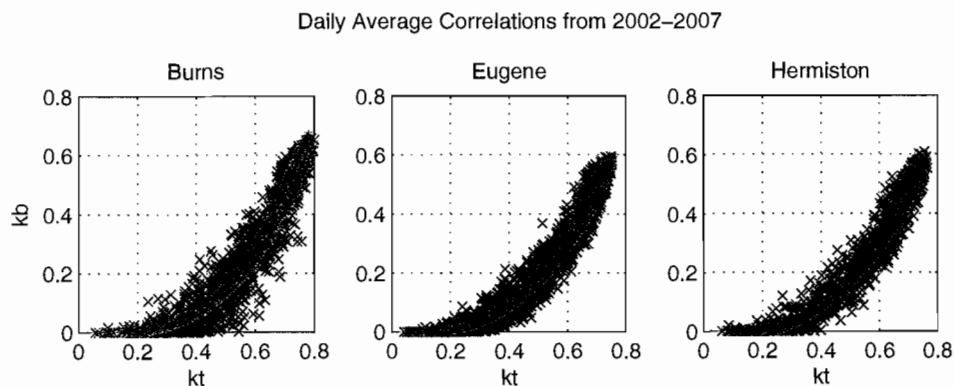


Figure 2.6. Correlations between daily average K_t and K_b for 2002-2007 at each site. The black points show measurements and the gray region plots the K_b data fitted from K_t measurements.

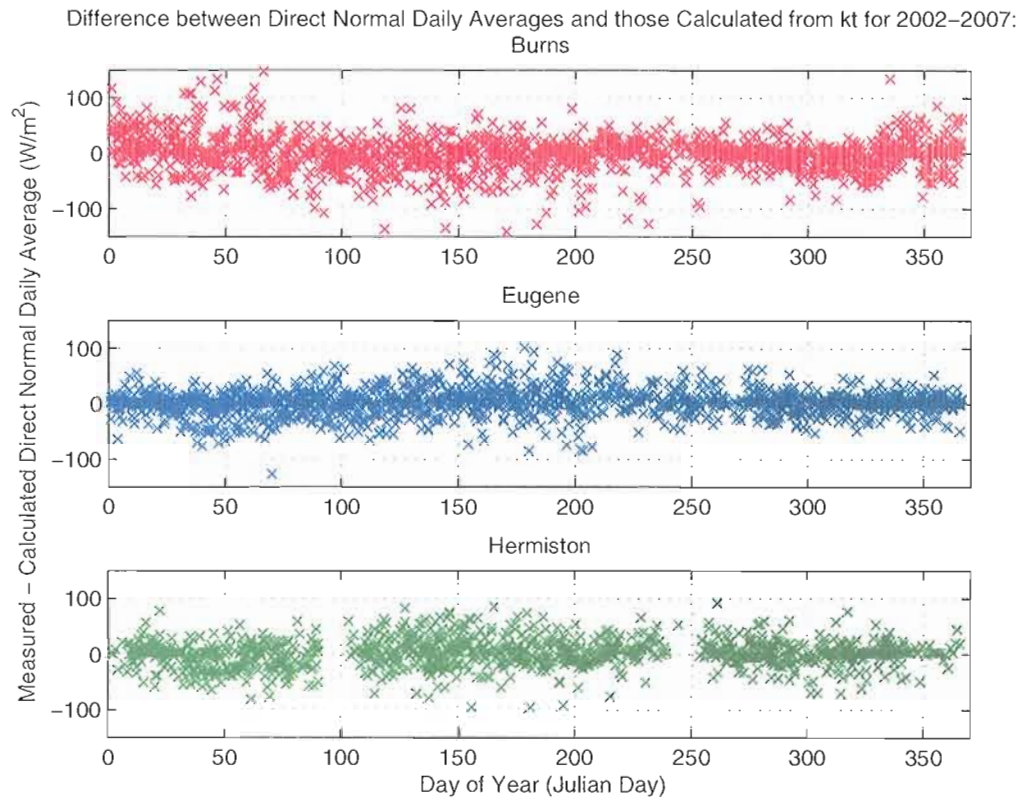


Figure 2.7. Differences between measured daily average direct normal irradiance and that calculated from K_t - K_b correlations for 2002-2007 plotted by year day.

Table 2.2. Statistical differences between measured and calculated daily average direct normal irradiance

	Burns		Eugene		Hermiston	
	W/m^2	%	W/m^2	%	W/m^2	%
Mean Bias Error	-1.47	-.66%	.10	.07%	.17	.09%
Standard Deviation	32.4	15%	23.6	16%	25.6	13%

CHAPTER III

DETERMINING CONSISTENT CALIBRATION NUMBERS

3.1. Introduction

The instruments used to measure irradiance by the University of Oregon Solar Radiation Monitoring Lab (UO SRML) output a voltage proportional to the incident solar irradiance. Conversion from voltage to irradiance is calculated by dividing the voltage measurement by a responsivity value, found by calibrating the instrument against a known reference irradiance. Over the years of UO SRML operation, calibration procedures have improved, incorporating new knowledge of systematic instrument errors. With many years of measurements, it is also now possible to better examine the change in responsivity of an instrument over the time it is used in the field. This chapter describes adjustments made to instrument responsivity values to ensure consistency of calibration over time.

Though the degradation of pyranometers is well known, it has rarely been formally documented. One study by *Nelson et al.* [1994] reported a decrease in sensitivity for Eppley Precision Spectral Pyranometers (PSPs) of 1.9% per year of exposure to

sunlight and a decrease in calibration factor for Eppley Normal Incidence Pyrheliometers (NIPs) of .37% per year of exposure. No significance values are given on the rates of decline in these studies. Visual inspection of the graphs indicates that while the decline in sensitivity of PSPs appears quite clear, that of the NIPs could be insignificant. Anecdotal evidence also indicates that no significant degradation occurs with NIPs, such as a report in the study by *El-Wakil et al.* [2001] that “no appreciable drift” is found in NIPs used in Egypt over a period of 5 years or more and calibrated annually against a reference instrument traceable to the World Radiometric Reference. UO SRML calibration records indicate that any degradation in the responsivity of NIPs is less than the uncertainty of the calibrations themselves. Thus, as described in the following sections, NIP calibration values have been kept constant throughout the instruments’ use.

PSPs, however, do degrade significantly over time. The degradation of the PSP sensor is likely caused by exposure to ultra-violet (UV) radiation. *Wilcox et al.* [2001] show that the PSP sensor degradation is more clearly correlated with the irradiance and temperature exposure of an instrument than the time a pyranometer is in the field. They also show that responsivity decline matches predictions from a model commonly used to predict the aging of paint. Two factors likely account for the difference in degradation. The coating on the surface of the PSP thermopile may degrade more than that on the NIP because the coatings are made from different lacquers. The second reason is that much of the UV radiation that reaches the surface is scattered and thus only impacts the diffuse and total components of radiation rather than the direct normal component (private communication from C. N. Long). Because of the significant degradation, PSPs must be

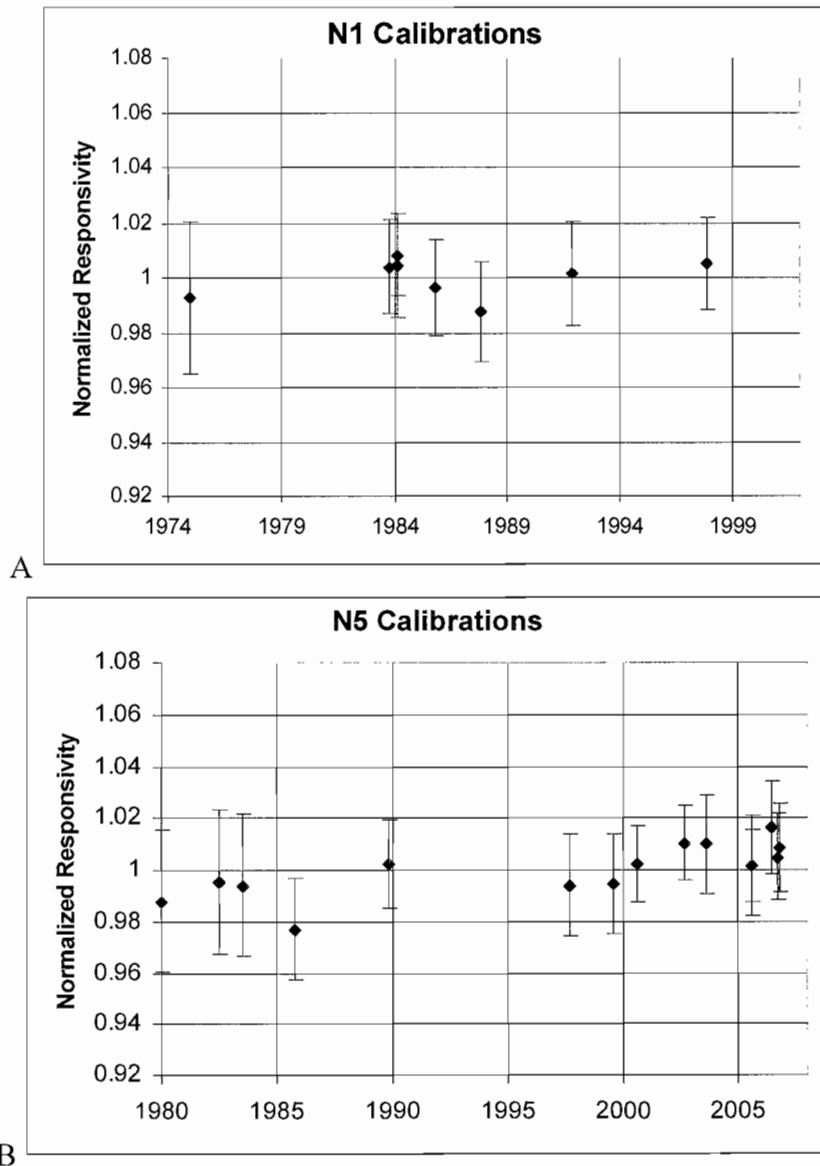
frequently calibrated to give accurate readings. Thus, as described in Section 3.3, PSP responsivity values are adjusted annually to account for changes in instrument sensitivity.

This chapter contains a description of the changes made to the responsivities of instruments and the reasons behind those changes. Section 3.2 describes NIP calibrations. Section 3.3 describes the more complicated adjustments made to PSP responsivities to adjust for instrument degradation. Details of specific changes made to instruments and plots of calibration histories are contained in the Appendices.

3.2. NIP Calibrations

To determine the correct responsivity for each NIP used in this study, the responsivities for all calibrations of each instrument were examined. As discussed in the introduction, one responsivity value for each instrument was used. As long as no outliers were present that varied significantly from the average for reasons like instrument malfunction, the average of all of these responsivities was used as the correct responsivity. Examples of the calibration histories of two of the instruments used at Eugene are shown in Figure 3.1. The ratios of responsivities from each calibration event to the mean responsivity are plotted throughout time. The responsivities vary within about 2% of the mean. The calibration histories show no discernable degradation. Figure 3.2 shows a plot of normalized values at solar noon on clear days for Eugene over its record. The different symbols represent measurements from different instruments. The measurements from

each instrument use the mean responsivity for all calibrations in the instrument's history. The figure shows no appreciable instrument degradation. The clear noon values remain constant over time.



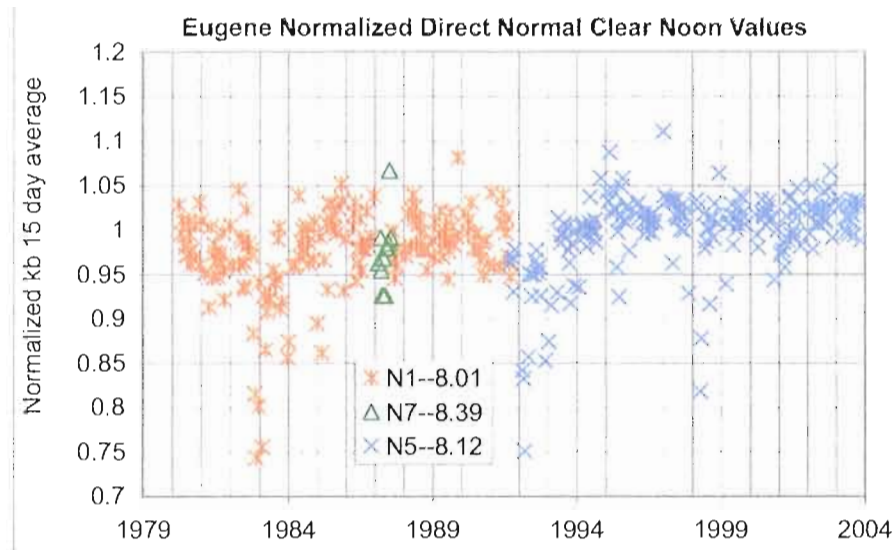


Figure 3.2. Eugene direct normal measurements at solar noon from clear days. Measurements have been divided by extraterrestrial irradiance, grouped into 15-day bins, and normalized by the average bin value over all years. Measurements made with different instruments are represented by different symbols. Besides low values from volcanic eruptions, the measurements remain fairly constant.

The responsivities of NIPs at the UO SRML come from two different calibration methods. Absolute calibrations of NIPs are done in comparison with an Absolute Cavity Radiometer whose calibration is traceable to the World Radiometric Reference. Relative calibrations are done in the field by comparing two NIPs. The absolute calibrations of UO SRML NIPs were done either at the Eppley factory or at the National Renewable Energy Lab (NREL). In order to check the consistency of NREL and Eppley calibration methods, a comparison was done between calibrations done at the two labs. NREL provided data from 19 pairs of instrument calibrations that were calibrated at both Eppley Labs and NREL before being placed in the field. Ratios of these calibration pairs are reasonably normally distributed with the mean centered around one and a standard deviation of 1.39%. A plot of the ratios is shown in Figure 3.3. Because Eppley does not

include uncertainty values with its calibrations, this study was also helpful as an estimate of the uncertainty in Eppley calibrations. Assuming an uncertainty of twice the standard deviation, the uncertainty of NIP calibrations done at Eppley Labs would be 2.78%. This is a reasonable uncertainty, though 1% higher than the 1.59% uncertainty in NREL calibrations [Myers *et al.*, 2004]. When using relative calibrations in this study, care was taken to use good responsivity values for the reference instruments. Instruments with the most complete absolute calibrations were used to calibrate other instruments.

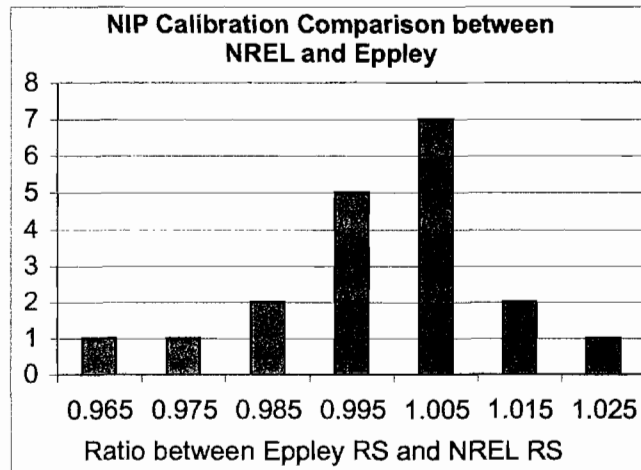


Figure 3.3. Histogram of ratio of responsivities for NIPs calibrated at Eppley and NREL. The sample size of 19 is reasonably normally distributed and centered around one.

In order to calculate the responsivity of each instrument over time, the mean of all responsivities in the instrument's calibration history was calculated. Twice the standard deviation of all responsivity records was then used as the uncertainty. This method works well for all instruments except for two instruments with a few calibrations that appear to be several standard deviations away from the rest. Appendix A includes plots of all

calibrations used in these calculations, including explanations of how these instruments were handled.

3.3. PSP Calibrations

Because of the previously mentioned calibration drift of the sensors in the Eppley Precision Spectral Pyranometers (PSPs), it is necessary to track calibrations of these instruments as accurately as possible over time. Unfortunately, the large uncertainty of the calibrations themselves limits how consistently the data can be adjusted for changing calibration constants. As was described in Chapter II, pyranometers respond differently to radiation incident at different zenith angles. Because some of that non-linearity in instrument response is due to a thermal offset from re-radiation of the sensor to the sky, calibration factors vary depending upon atmospheric conditions [see for example, *Myers et al.*, 2002]. Because of these uncertainties, the zenith angles used and the atmospheric conditions during a calibration can make responsivities for PSPs calibrated using different methods vary by several percent.

3.3.1. Adjusting PSP Calibration Methods for Consistency

Because the PSPs were calibrated using several different methods, calibration histories of the instruments reflect both changes in the instruments and in the calibration

methods. Absolute calibrations of SRML instruments have been done at three different locations: Eppley Labs, the Solar Radiation Facility at NOAA, and the National Renewable Energy Lab (NREL). Calibrations done at Eppley labs and NOAA were calculated as a composite of all zenith angles. At NREL, responsivities were given in the past for solar zenith angles of 45-55 degrees and more recently at 45 degrees. Eppley calibrates in a controlled lab setting, but NOAA and NREL calibrations are done outside, in comparison to an absolute cavity radiometer. NOAA used a shade and unshade technique to compare calculated direct normal irradiance to the reading from an absolute cavity radiometer. NREL calibrations are done using a component summation technique which compares instruments to a calculated total irradiance value by summing the direct normal irradiance measured by an absolute cavity radiometer with the diffuse irradiance measured by a shaded pyranometer. NREL has also changed its methodology over time to incorporate new research in calibration accuracy. NREL began using a black and white type pyranometer instead of an all black pyranometer (like the Eppley PSP) to measure the reference diffuse irradiance in March of 2000. Because of the thermal offset, using an all black pyranometer can introduce errors into the diffuse irradiance of about 15 W/m^2 [Myers *et al.*, 2002]. NREL estimates this change to make responsivity values calculated before 2000, 2.5-3% higher than the current method.

All calibration methods were adjusted to be consistent with a “reference” method. Though the recent calibrations from NREL use one of the best methods available, the NREL calibrations give responsivity values 2-3% lower than those found in Eugene. Eugene calibrations are done against a reference total irradiance found by

summing measured diffuse and direct normal irradiance. The difference between calibrations done in Eugene and NREL is likely caused by the thermal offset due to sky temperature. The different altitudes of Eugene and the Golden, Colorado NREL site lead to different sky temperatures on clear days. Also, in processing the data, the UO SRML subtracts the negative nighttime values from the values during the day to correct some of the thermal offset. Nighttime offsets are not subtracted in calibrations at NREL which could lead to systematic differences in the calibrations done by NREL and the UO SRML. In order to check the impact of using responsivity values calibrated at these two locations, diffuse irradiance was calculated in Eugene by subtracting the direct irradiance projected onto a horizontal surface from the total irradiance measurement. This calculated diffuse irradiance was then compared to that measured by a black and white type pyranometer. Using the responsivity calculated at NREL gave errors of larger than 10 W/m^2 in the calculated diffuse irradiance at a zenith angle of 45° . Because the UO SRML does not have infrared radiation measurements at our sites, corrections for the thermal offset cannot be calculated in field measurements. Thus, the differing sky conditions between Eugene and the high altitude lab of NREL along with the SRML data processing method of subtracting nighttime negative values make the responsivities calculated in recent years at NREL too low for use in Eugene. All other calibration methods were adjusted to calibrations done at Eugene for a reference total irradiance calculated by summing measurements projected onto a horizontal surface from a NIP and a shaded black and white pyranometers at a zenith angle of 45° .

Responsivities calibrated at NREL after March of 2000 were shifted up by 2.5% to make them match the “reference” responsivities calculated in Eugene. As was discussed earlier, responsivities found at NREL before 2000 were 2.5-3% higher than those done recently because of different diffuse measurements. In this study, NREL calibration records before 2000 were not adjusted, making them consistent with both recent NREL calibrations and Eugene calibrations. Early responsivities calibrated at NREL were originally determined for zenith angles between 45-55°. To be consistent, the responsivity value at 45° was found from the calibration reports and used instead.

To check the consistency of Eppley calibrations with those of NREL, sixty-nine instrument calibration records with pairs of responsivities found by Eppley and NREL BORCAL calibration events were provided by NREL. Ratios between the two responsivities were calculated. (The NREL calibrations used were done before 2000, so they are consistent with the responsivities used by the UO SRML.) The results showed surprising variation. As shown in Figure 3.4, the distribution of differences appears bimodal. The mean of the ratios is 1.023, meaning that Eppley gives larger responsivity values using its calibration method than does NREL. However, as shown in the graph, there appear to be two distributions, one centered around 1.01 and another centered around 1.035.

In order to examine this further, the responsivity ratios are plotted by date of calibration at NREL (date of their BORCAL calibration events). The red ×'s and green o's in Figure 3.5 show the range of the Eppley calibrations. All of these points were calibrated at the same time at NREL, so the sky conditions and methods should be the

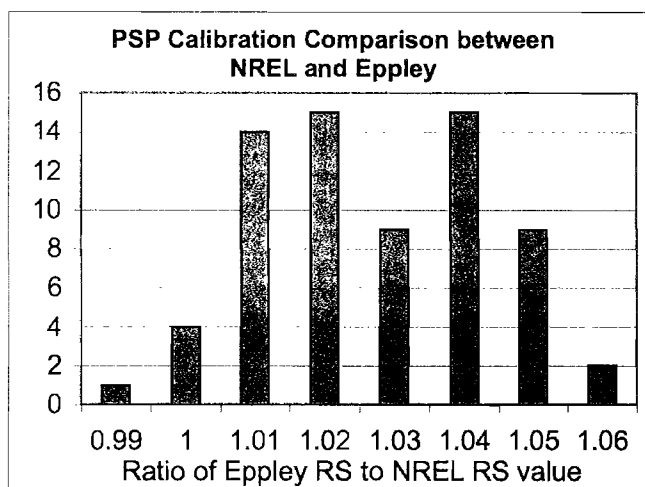


Figure 3.4. Histogram of ratios of PSP responsivities calibrated by Eppley and NREL. Sixty-nine ratios show a bimodal distribution.

same. However, the instruments plotted with o's were calibrated at Eppley Labs in September of 1995, and those represented by x's were calibrated at Eppley Labs in March of 1996. The Eppley responsivities of the two groups of instruments are about 3% different between the two groups compared to NREL responsivities, though each group shows a spread of only 2%. The small spread indicates that the 3% gap between the two groups does not likely come from the calibration process at NREL. Thus the methodologies are different enough to make it difficult to compare them directly. It does appear, however, that the responsivities calculated at Eppley Labs are generally higher than those calculated at NREL, so all Eppley calibrations were shifted down by the average offset between the calibration methods, 2.3%.

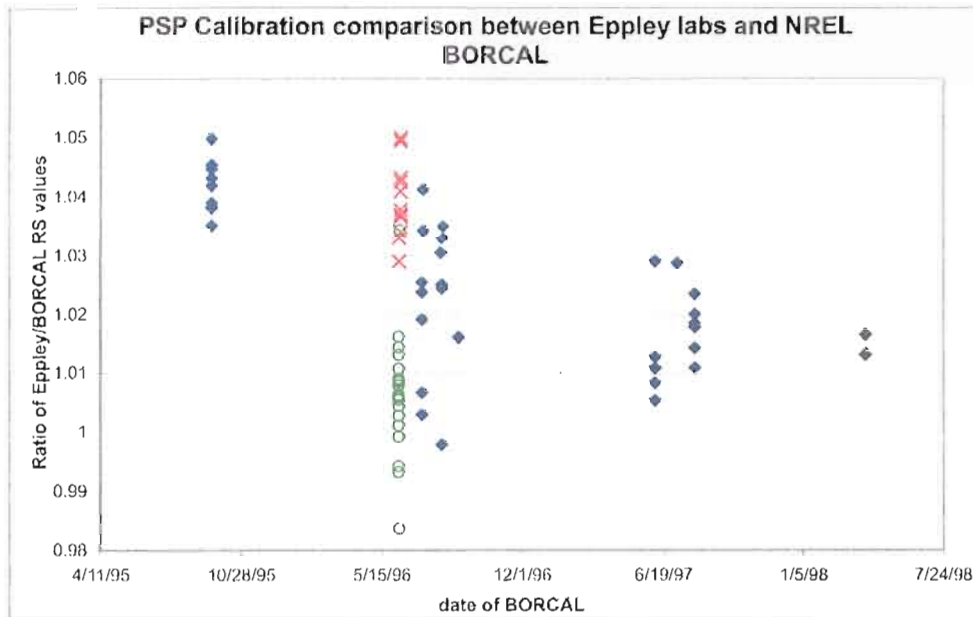


Figure 3.5. Ratio of PSP responsivities from Eppley labs and NREL, plotted by NREL calibration date. Two groups of instruments (red \times 's and green o 's) calibrated at Eppley at two different times but at the same time at NREL are offset by 3%.

No data set was available to compare calibrations from NOAA and NREL, though a UO SRML study found Eppley calibrations to be 1% higher than the responsivities calculated at NOAA. The comparison was based on a sample of sixty-seven calibration record pairs (Vignola and McDaniels, unpublished manuscript, 1999, available at <http://solar.dat.uoregon.edu/PacNWSolarRadiationDataBook.html>). The NOAA method of calibration should be quite similar to the methods used at NREL and Eugene because it involves comparing a calculated direct normal value from shaded and unshaded pyranometer measurements to an absolute cavity radiometer direct normal measurement. The NOAA method differs from the reference method in that NOAA calculated its values as an average over all zenith angles rather than at a zenith angle of 45° . Thus, NOAA responsivity values should be 1-2% higher than the reference. For the purposes of this

study, NOAA calibration values were shifted down by 1% to compensate somewhat for this difference in zenith angles. This makes the change consistent with the results found in the study comparing NOAA and Eppley responsivities.

Table 3.1 gives a summary of the adjustments made to responsivity values depending on the method of calibration. Calibrations in Eugene of PSPs against a sum of diffuse and direct normal measurements were used as the reference. Responsivities found at NREL before 2000 were chosen at a zenith angle of 45° instead of $45\text{-}55^\circ$. And responsivities from calibrations done at NREL after 2000, Eppley Labs, and NOAA are all shifted up or down by the percentage indicated in the table.

Table 3.1. Adjustments made to responsivities from different calibration methods

Cal. method:	Responsivity Adjustment
Eugene	None
NREL before 2000	changed to zenith angle 45°
NREL after 2000	\uparrow 2.5%
Eppley	\downarrow 2.3%
NOAA	\downarrow 1%

3.3.2. Using Adjusted Calibration Records to Find Instrument Responsivities

Because of the uncertainties in the consistency of different calibration methods, measurements taken on clear days at solar noon were used in addition to calibration records to correct historical PSP responsivities. To obtain these clear-sky data, clear solar noon periods were identified by visual inspection of continuously plotted back up charts.

The charts give more knowledge of short-term variability caused by clouds than 5-minute resolution data. The clear-sky solar noon values from each year were then grouped into 25, 15-day bins and normalized to improve statistics. An example of these clear day values is plotted in Figure 3.6. The figure shows Eugene normalized clear noon values when each instrument keeps the same responsivity value for the entire time it is in use. Note how different the inter-annual change in clear-sky total irradiance is from the clear-sky direct normal values for the same site shown in Figure 3.2. The total irradiance clear noon values clearly decline over time.

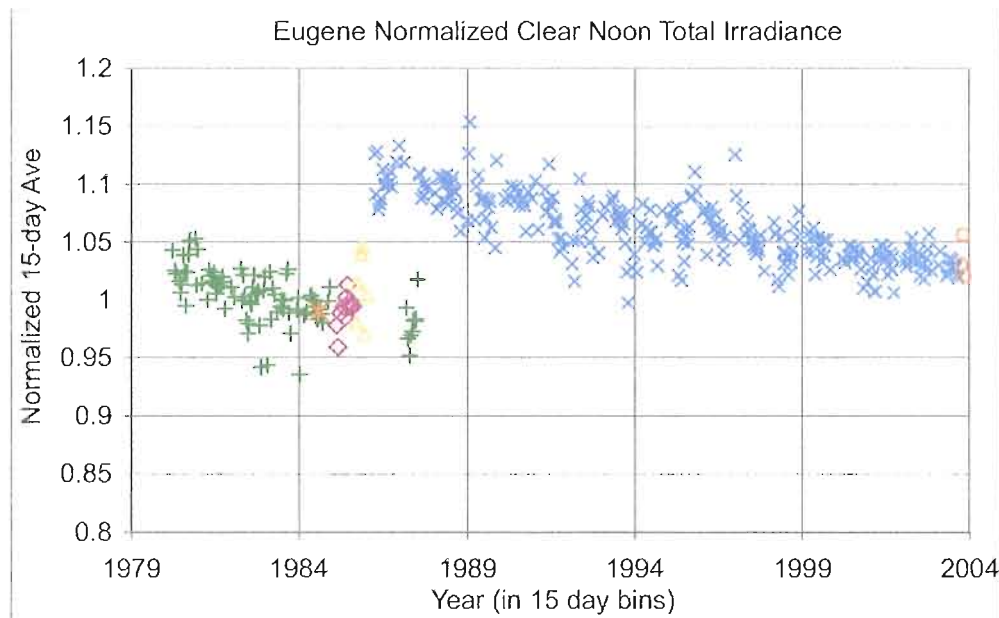


Figure 3.6. Clear noon total irradiance values processed as described in Figure 3.2. Each symbol represents measurements made with a different instrument. Measurements have been adjusted so that each instrument uses a constant responsivity value for all time at this site.

Special attention was given to the Eugene instruments labeled P1 and P3 because they have been the primary reference instruments for all relative calibrations done in

Eugene and in the field. As a result, these instruments were the most frequently calibrated against absolute cavity radiometers. The responsivity values for the two instruments were determined by fitting regression lines to the responsivities from historical calibration records. Following the convention of *Wilcox et al.* [2001], calibration changes were examined based on accumulated exposure to radiation.

Figure 3.7A shows the responsivities of P1 by MWhr/m^2 of irradiance exposure at the time of calibration. The dotted line shows a linear regression fit to the calibration records. The orange \times 's show the annually adjusted responsivity that was used with the instrument. These values were calculated from the linear regression fit of the responsivities until 1989. After 1989 (around 13 MWhr/m^2 in Figure 3.7A), responsivity values were fit only using calibrations from the period 1989 to 2007. This was done because the instrument is an important calibration reference during this period, and many more calibration records were available after 1989 than before, giving more accurate responsivity values between 1989 and the present. The red triangles in Figures 3.7 show corrected responsivities calculated by fitting a linear regression line to the clear noon data in Figure 3.6 (green \times 's). The remarkable agreement between responsivity corrections calculated from a linear fit to calibration records and clear noon values confirms that the decrease seen in Figure 3.6 is due primarily to a change in the sensitivity of the instrument to incoming radiation.

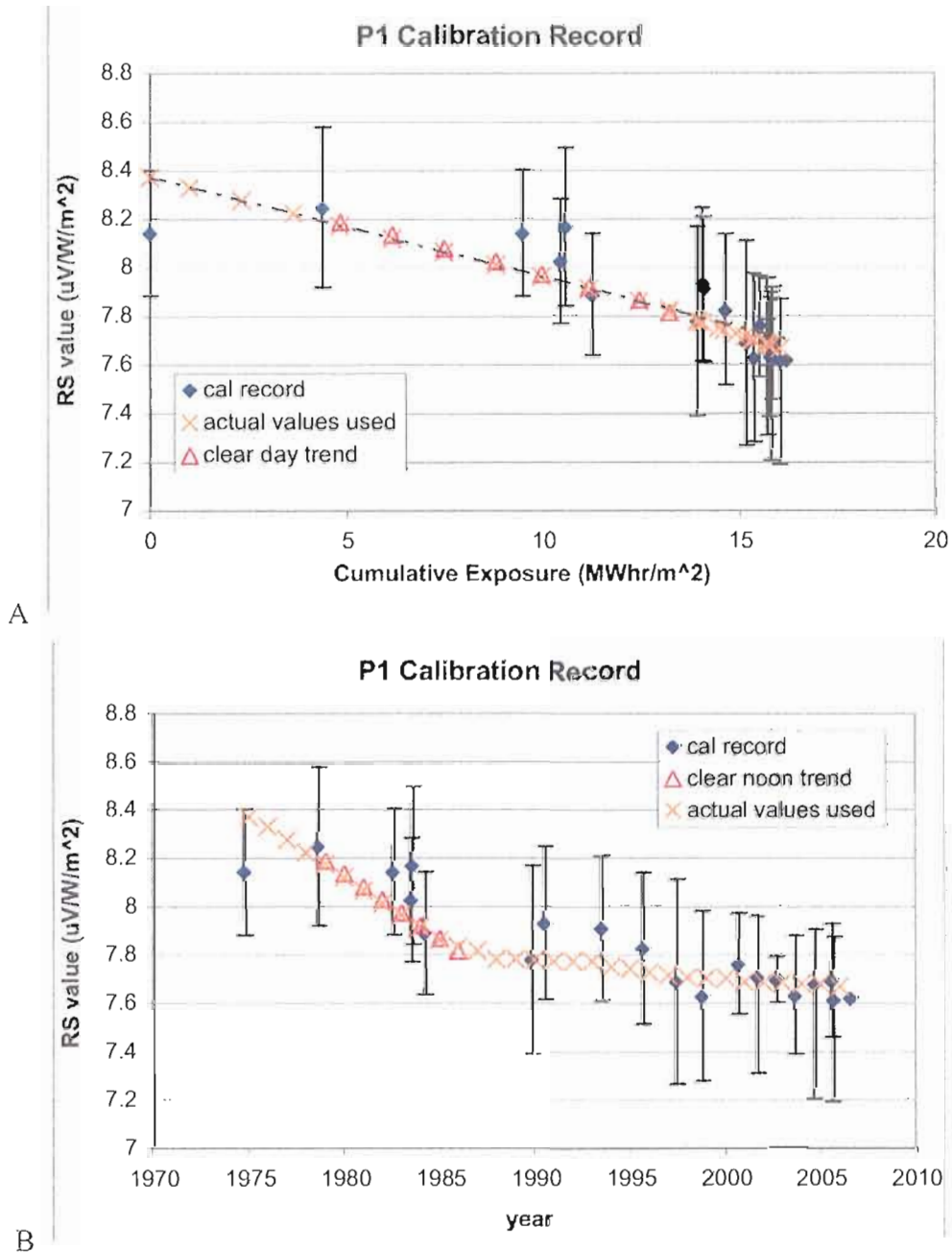


Figure 3.7. Calibration record for PSP P1 used at Eugene and as a reference. Note that a linear fit to the responsivities plotted by cumulative exposure to radiation (A), gives two distinct slopes when the responsivities are plotted by year (see the orange \times 's in (B)). These two different slopes correspond to times when the instrument was in the field until 1987, and the following years when the instrument has been used as a calibration reference.

Figure 3.7B shows how important it is to look at irradiance exposure rather than simply the age of the instrument in determining responsivity change. In this plot, the responsivities from different calibrations are plotted by the date of calibration. Plotting the adjusted responsivities in orange \times 's again, shows two distinct slopes when the instrument was being used in the field (until 1987) and when it has been used as a reference instrument only.

Having determined accurate values for P1 over time, relative calibrations with P3 were determined along with corrected absolute calibrations. Figure 3.8A plots these responsivities against cumulative radiation exposure. Like P1, corrected responsivity values for P3 were determined from the linear regression fit of the corrected responsivities shown by the orange \times 's in Figure 3.8A.

The remaining responsivity values for instruments used in Eugene were calculated similarly from corrected calibration records. Details can be found in Appendix B. The clear noon values were then adjusted by these new responsivities and are plotted in Figure 3.9. The corrected responsivity values eliminate the trends seen in Figure 3.6.

The clear day values and the calibration histories give consistent changes over time. P3 shows this particularly well as it was used in Eugene over a period of almost 20 years and has one of the most complete and accurate calibration histories of all the instruments. Figure 3.8 also shows the consistency between the trend in clear day values and the calibration records. The corrections calculated from a fit to the clear noon trend (red triangles) and the responsivity corrections calculated from a fit to the calibration history (orange \times 's) are nearly identical. The percent per year decrease calculated from

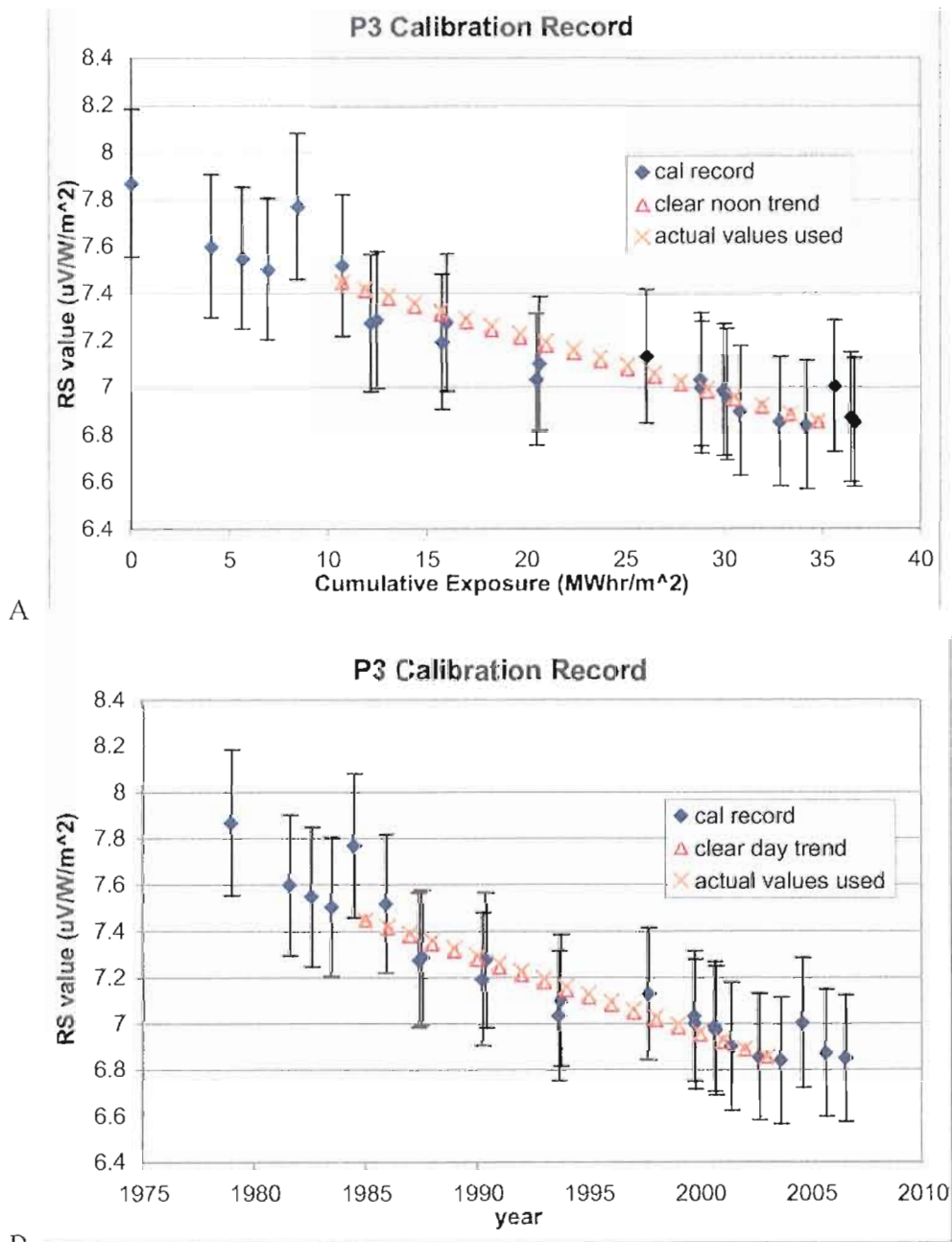


Figure 3.8. The calibration history of P3 shows a very good fit between corrected responsivities calculated by a linear fit to the records (orange \times 's) and a fit to the clear day data in Eugene (red triangles). As the instrument was used in the field for almost its entire history, the plot of responsivities by cumulative exposure and time are very similar.

the clear day values is .44%. The percent per year decrease calculated from the calibration history plotted by cumulative exposure is on average .46% per year. That similarity in annual responsivity change implies that there is no significant change in the clear-sky values at solar noon beyond calibration changes of the instruments.

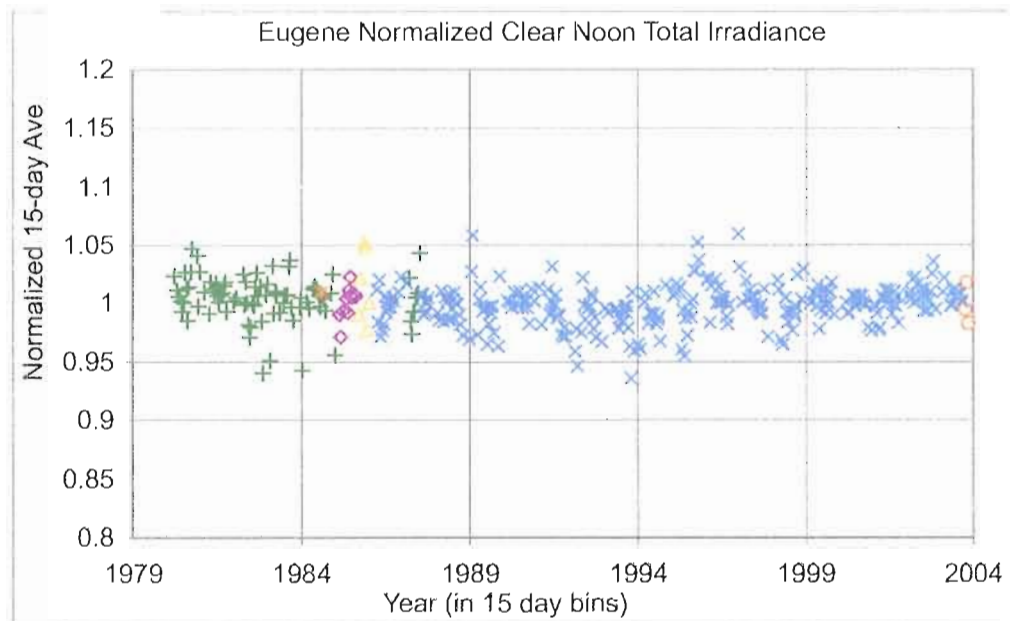


Figure 3.9. Eugene normalized clear noon measurements using annually adjusted responsivity values determined by a linear regression fit of responsivities from the calibration records.

The lack of a significant trend in clear-sky direct normal values at solar noon (Figure 3.2) supports the conclusion that there is no significant clear-sky change in total irradiance. The primary changes viewed in Figures 3.2 and 3.9 are from the dips caused by volcanic events. Figure 3.10 plots Eugene clear-sky measurements using the UO SRML's original calibration record for the PSPs. The instruments were calibrated using different methods that had not been adjusted for consistency. The changes in calibration

methods over time cause an increase of over 6% in clear noon values over the last 20 years. That calibration-caused trend highlights the importance of accurately calibrating PSPs.

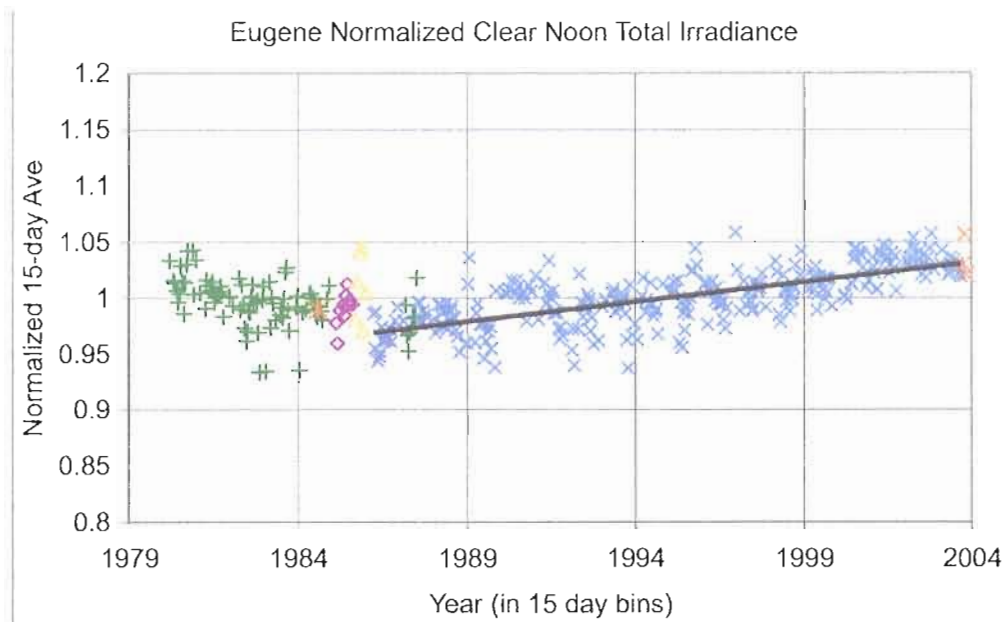


Figure 3.10. Eugene normalized clear noon measurements using responsivities from calibration events every 2-3 years. Note the 6% increase over 20 years seen in the blue \times 's compared with no change found in Figure 3.8.

Because clear-sky trends give the same annual responsivity change as calibration records, instrument responsivities at other sites were calculated using clear day records. Using the clear day records is much less work than calculating the cumulative exposure for calibration events, though it shows a similar level of accuracy in responsivity corrections. Using clear-sky corrections may also be more accurate for the instruments that were only calibrated a few times over their period of use at a particular location. Correcting the responsivities based on these clear noon measurements also removes any trend in clear-sky measurements caused by aerosol changes. The lack of a trend in clear-

sky direct normal irradiance and the removal of the clear-sky total irradiance trend by calibration corrections in Eugene indicates that any trend in clear-sky total irradiance is too small to detect. Even if a real trend was removed, the analysis to determine any possible change in aerosols is done primarily using direct normal irradiance in Chapters V and VI, and so does not change the conclusions of the study.

Except for P20, used recently in Burns, instruments used for a significant portion of time at Burns and Hermiston were corrected using clear day data. (P20 changes were calculated based on calibration records because there was not enough clear day data.) To make corrections from clear noon measurements, first all the measurements made by a particular instrument were adjusted so that they were calculated from the same responsivity. The annual change in responsivity was calculated from these normalized values. The absolute values of these responsivities were then checked to make sure they matched corrected calibration records and neighboring clear day measurements from other instruments. The clear day values over time resulting from these corrections are plotted in Appendix B for Burns and Hermiston along with calibration records for each instrument.

CHAPTER IV

ANALYSIS OF ALL-SKY IRRADIANCE MEASUREMENTS

4.1. Introduction

Global dimming studies found decreases in total surface solar irradiance at monitoring sites worldwide of approximately 2-5 W/m² per decade or 1-3% per decade between 1960 and 1990 [Gilgen *et al.*, 1998; Stanhill and Cohen, 2001; Liepert, 2002]. Total surface irradiance trends are positive at most of those monitoring stations since 1990 [Wild *et al.*, 2005]. In this chapter, linear trends are calculated in UO SRML all-sky total horizontal and direct normal irradiance in order to compare the changes in Oregon with those reported in the dimming and brightening studies. Both components of radiation increase at the three Oregon stations used in this study over the period from 1980 (or earlier in Eugene) until 2007. The magnitude of the direct normal trend is reduced when the years most heavily impacted by volcanic eruptions are removed. Seasonal trends show the strongest increases in the summer. The increases in direct normal irradiance are supported by comparisons with satellite-derived direct normal irradiance at the surface.

Section 4.2 gives a description of the method of trend calculation and its uncertainty. The magnitudes of annual average, monthly average, and seasonal trends are given in Section 4.3. The last section, 4.4, contains a summary of the results of a study comparing the surface measurements with satellite-derived irradiances for the same region.

4.2. Method of Calculating Trends and Uncertainties

Linear trends are calculated for annual averages of daily average total irradiance, and for monthly, seasonal, and annual averages of daily average direct normal irradiance. Monthly averages are calculated from 24-hour, daily average irradiance. Missing direct normal daily averages are filled in with correlations from other instruments as described in Section 2.5. The annual and seasonal averages are calculated as means of monthly averages. Averaging each longer time step from the previous one weights each month equally, minimizing the impact of any remaining missing data.

Trends are calculated using standard least squares regression line fits to the data, so that the irradiance values, y_i , can be described by an equation of the form:

$$y_i = a + bx_i + \varepsilon_i, \text{ (Eq. 4.1)}$$

where ε_i are residuals. While changes in aerosols and clouds are not likely to exhibit purely linear behavior, a linear fit to the data is a simple calculation that is consistent with

the other global dimming and brightening studies described in Chapter I. Thus, linear trends give a basis of comparison to other studies of surface irradiance change.

In addition to determining the uncertainty of a given trend due to the inherent “noise” of a data set, the autocorrelation, or persistence, of the dataset can make a trend look statistically significant that isn’t. Least squares regression calculations assume the data being fit are independent, but this is not generally the case for consecutive time steps in meteorological time-series. *Weatherhead et al.* [1998] discuss the impact of including autocorrelation on the uncertainty of a trend in monthly averages. Their method assumes a time series model with a linear trend and noise that is autoregressive of order 1, AR(1). This same assumption was made for the trend calculations in this study.

Following standard practice, trend uncertainties calculated in this chapter, Chapter V, and Chapter VI are based on the standard error of the slope coefficient, b . The standard error of b is calculated as:

$$SE(b) = \frac{\sqrt{\frac{\sum (y_i - (a + bx_i))^2}{\sum (x_i - \bar{x})^2}}}{\sqrt{df}} \quad (\text{Eq. 4.2}),$$

where df is the number of degrees of freedom of the dataset, and a bar signifies an average quantity. When the data are linearly independent, df is the number of data points minus two. When autocorrelation is a factor, then the number of degrees of freedom is reduced. Assuming first order autocorrelation, df is approximately equal to:

$$df = (N - 2) \frac{(1 - \phi)}{(1 + \phi)} \quad (\text{Eq. 4.3}),$$

where N is the number of data points and ϕ is the first order auto-correlation coefficient of the residuals after removing the linear trend. The equation for the degrees of freedom is based on personal communications with Halstead Harrison. An unpublished memo on the subject can be found at <http://www.atmos.washington.edu/~harrison/reports/df.pdf>.

The trends and their uncertainties have units of W/m^2 per year or percent change per year. The trend uncertainties are given in Tables 4.1 and 4.2 as twice the standard error of the slope coefficient, an estimate of the 95% confidence interval. Trends greater in magnitude than this uncertainty are considered to be significant.

4.3. Trends in Direct Normal and Total Irradiance

The regression fits to annual averages of total horizontal irradiance indicate an increase of .1-.2% per year or .2-.3 W/m^2 per year at the three stations (see Table 4.1). The trends for Burns and Hermiston are calculated from annual average irradiance for the years 1980-2007, and the trend for Eugene is calculated over the longer period of 1976-2007. The annual averages and their trends are plotted in Figure 4.1. The solid black lines in the plot are the trend for all years of data. The increase is statistically significant at the 95% confidence level, using the definition of significance described in the previous section. The magnitude of the increase in total irradiance in Oregon (1-2% per decade) is the same order of magnitude of the decrease reported in global dimming studies (1-3% per decade) [Gilgen *et al.*, 1998; Stanhill and Cohen, 2001; Liepert, 2002].

Table 4.1. Surface irradiance trends and uncertainties

	Eugene		Burns		Hermiston	
	<i>% per yr</i>	<i>W/m² per year</i>	<i>% per yr</i>	<i>W/m² per year</i>	<i>% per yr</i>	<i>W/m² per year</i>
<i>Direct Normal Irradiance</i>						
Monthly	0.53% ±0.35%	0.82 ±0.54	0.48% ±0.24%	1.10 ±0.54	0.48% ±0.27%	0.75 ±0.43
Annual	0.54% ±0.34%	0.83 ±0.53	0.49% ±0.41%	1.10 ±0.93	0.48% ±0.35%	0.75 ±0.56
Winter	0.40% ±0.91%	0.23 ±0.53	0.25% ±1.07%	0.28 ±1.21	0.81% ±1.21%	0.56 ±0.83
Spring	0.36% ±1.06%	0.52 ±1.56	0.29% ±0.66%	0.63 ±1.44	0.05% ±0.55%	0.10 ±1.16
Summer	0.64% ±0.62%	1.76 ±1.71	0.54% ±0.38%	1.93 ±1.37	0.49% ±0.40%	1.67 ±1.36
Fall	0.57% ±0.74%	0.81 ±1.05	0.75% ±0.56%	1.61 ±1.21	0.35% ±0.48%	0.62 ±0.86
<i>Total Horizontal Irradiance</i>						
Annual	0.20% ±0.14%	0.31 ±0.21	0.13% ±0.09%	0.29 ±0.21	0.10% ±0.07%	0.19 ±0.14

Table 4.2. Surface irradiance trends after removing volcanic years (1982-1985; 1991-1994)

	Eugene		Burns		Hermiston	
	<i>% per yr</i>	<i>W/m² per year</i>	<i>% per yr</i>	<i>W/m² per year</i>	<i>% per yr</i>	<i>W/m² per year</i>
<i>Direct Normal Irradiance</i>						
Monthly	0.43% ±0.34%	0.67 ±0.52	0.22% ±0.27%	0.49 ±0.61	0.36% ±0.30%	0.57 ±0.47
Annual	0.43% ±0.32%	0.66 ±0.49	0.22% ±0.28%	0.50 ±0.63	0.36% ±0.30%	0.57 ±0.46
Winter	0.30% ±1.05%	0.17 ±0.61	-0.06% ±1.13%	-0.07 ±1.28	1.08% ±1.52%	0.74 ±1.04
Spring	0.41% ±0.93%	0.59 ±1.35	0.11% ±0.68%	0.24 ±1.48	0.09% ±0.59%	0.19 ±1.26
Summer	0.52% ±0.50%	1.44 ±1.37	0.32% ±0.43%	1.16 ±1.55	0.53% ±0.75%	1.82 ±2.58
Fall	0.23% ±0.80%	0.33 ±1.13	0.33% ±0.56%	0.71 ±1.20	0.02% ±0.70%	0.04 ±1.25
<i>Total Horizontal Irradiance</i>						
Annual	0.19% ±0.15%	0.29 ±0.23	0.08% ±0.12%	0.18 ±0.28	0.08% ±0.09%	0.16 ±0.19

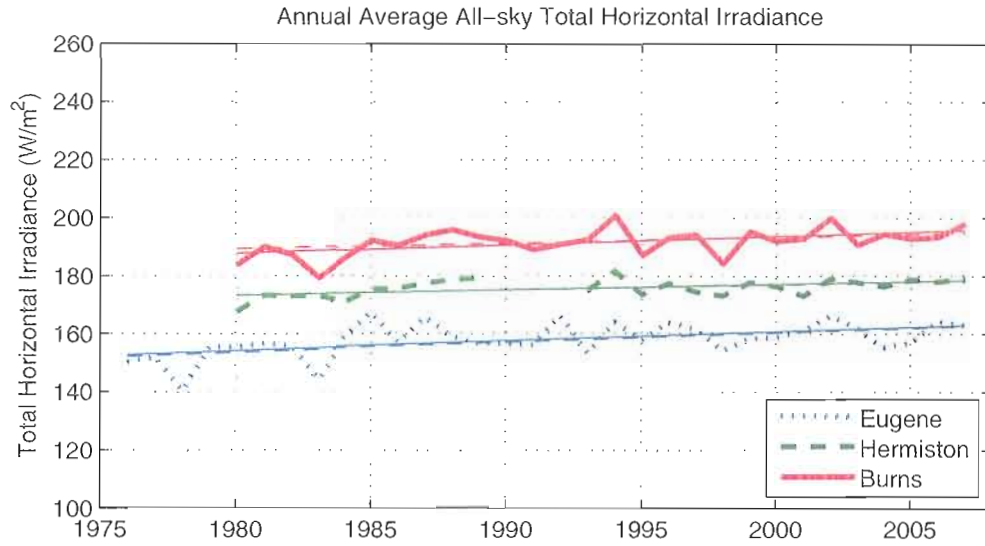


Figure 4.1. Annual average daily total horizontal irradiance with linear trends. Solid trend lines show linear fits to all years of data at each site. Dashed trend lines show linear fits after removing the years most heavily impacted by volcanic eruptions (1982-1985, 1991-1994).

The positive trend in direct normal irradiance is stronger than that in total irradiance, as expected because direct normal irradiance is more sensitive to scattering by clouds and aerosols. The first two rows of Table 4.1 give the magnitudes of the trends and uncertainties for monthly average anomalies and annual averages of direct normal irradiance. Trends in annual average and monthly average anomalies of direct normal irradiance are also plotted with solid lines in Figures 4.2 and 4.3 respectively. Anomalies of monthly averages are calculated by subtracting a typical monthly average from each individual monthly average in order to deseasonalize the data. The magnitudes of the trends in annual averages and monthly average anomalies match at each of the three sites. Only Burns has a different uncertainty in the slope of trends calculated from annual and monthly averages. The agreement between monthly and annual averages confirms that

the trends in monthly averages are not impacted by seasonal, but inter-annual changes.

Seasonal averages of direct normal irradiance also increase, though only the summer trends are statistically significant at all sites. At Burns, both fall and summer increases are statistically significant. These seasonal trends are plotted in Figure 4.4.

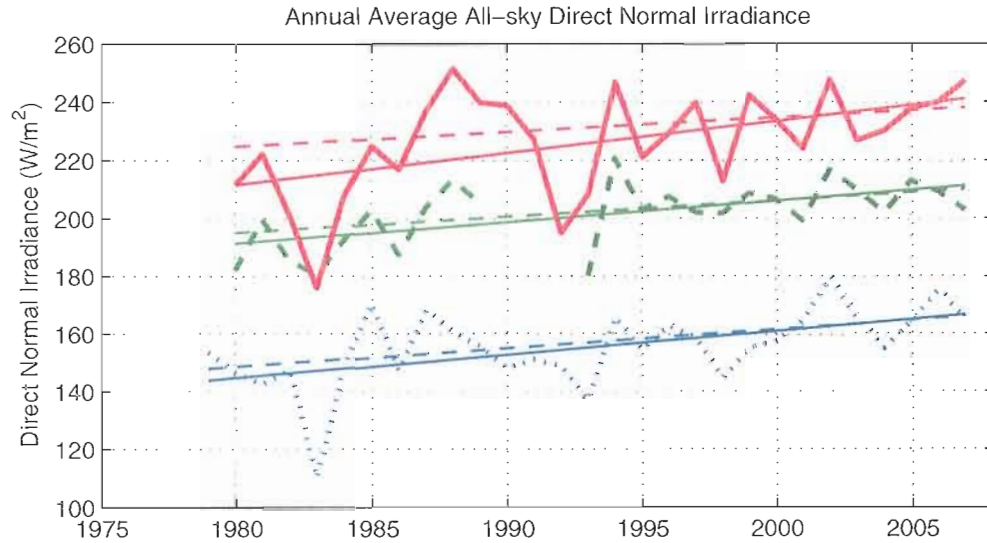


Figure 4.2. Annual average daily direct normal irradiance with linear trends. Solid trend lines show linear fits to all years of data at each site. Dashed trend lines show linear fits after removing the years most heavily impacted by volcanic eruptions.

The decrease of atmospheric transmission worldwide following the volcanic eruptions of El Chichón in Mexico (March 1982) and Mt. Pinatubo in the Philippines (June 1991) is well known [see for example, *Sato et al.*, 1993; *Schwartz*, 2005]. The impact of these eruptions can be seen in the strong decreases of direct normal irradiance in 1982 and 1991 in Figure 4.2. To estimate the impact of the volcanic eruptions on the trends seen in direct normal irradiance, the trends are recalculated for each data set after removing the periods most impacted by the eruptions (March 1982 to December 1985,

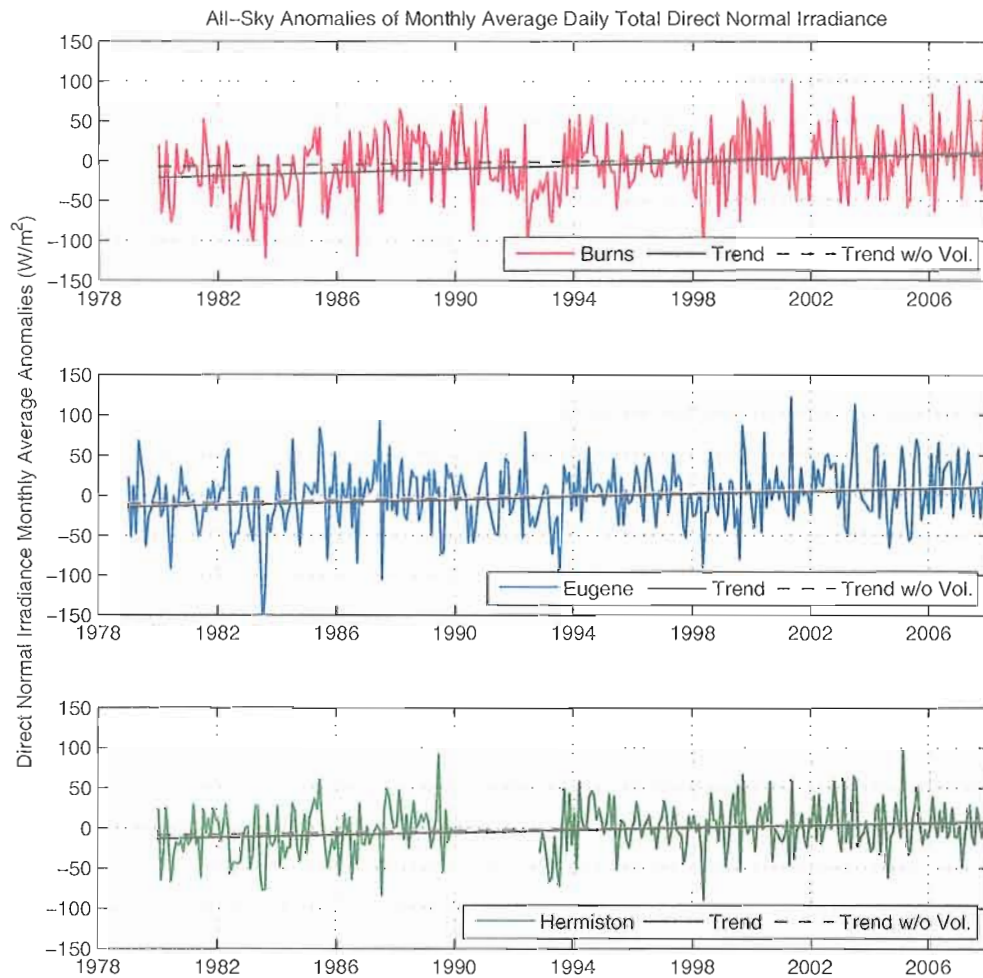


Figure 4.3. Monthly average anomalies of daily direct normal irradiance with linear trends. As with annual averages, solid lines show trends from all years and dashed lines show trends with volcanic periods removed.

and June 1991 to December 1994). Table 4.2 lists the results of the trend calculations without volcanic years. The thin dashed lines in Figures 4.1-4.3 show the trends visually. Removing the volcanic years reduces the trend in direct normal irradiance at Eugene by about 20%, at Hermiston by 24%, and at Burns by over 50%. The trends at Eugene and

Hermiston remain significant, but the trend at Burns has a higher uncertainty than the other sites. This high uncertainty may be due to missing data in 1988. Removing the volcanic years from the total irradiance time series reduces the magnitude of the trend by about 6% at Eugene, 16% at Hermiston, and 38% at Burns. The lower reduction in Eugene data, the only trend that remains significant with the removal of volcanic years, is due to the longer time series available at that site. Of the seasonal trends calculated, only the summer trend at Eugene remains significant.

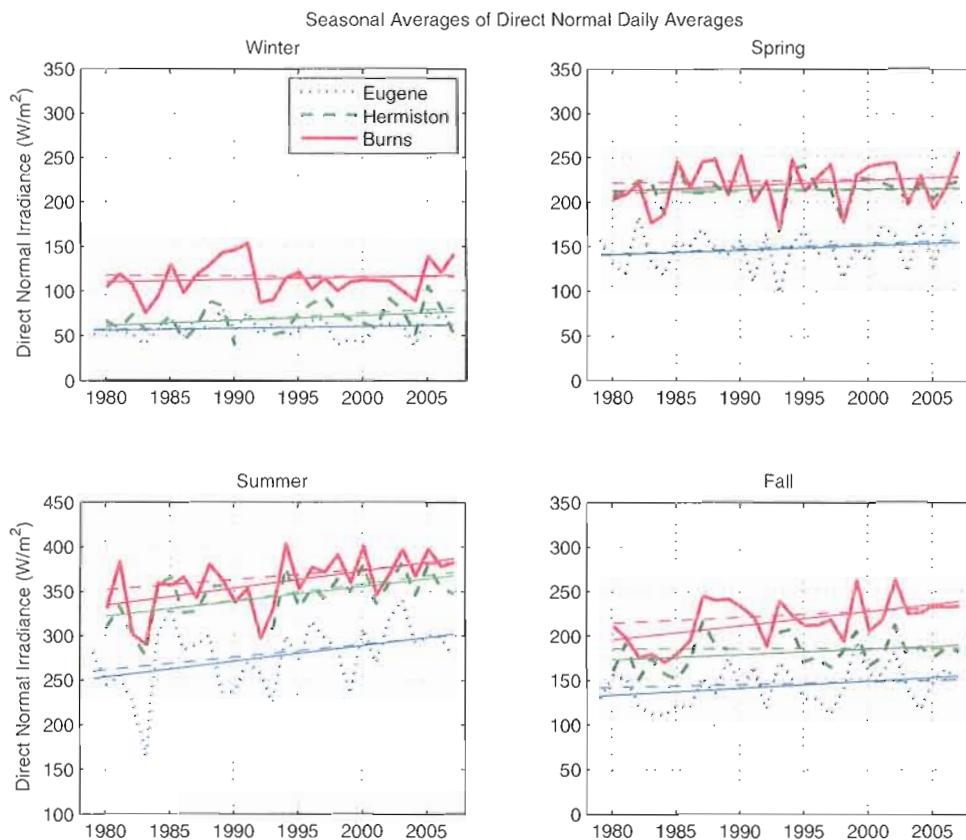


Figure 4.4. Seasonal average daily direct normal irradiance and linear trends with (solid line) and without (dashed line) volcanic years.

4.4. Comparing Measurements to Satellite-Derived Direct Normal Irradiance

The positive direct normal trends match trends found in a satellite-derived surface irradiance dataset, called DLR-ISIS [Lohmann *et al.*, 2007]. The spatial resolution of the DLR-ISIS dataset is large, with grid boxes of 280 km per side. This is on the order of the spacing between the three ground measurement sites. The positive trends in the DLR-ISIS data confirm that the trends are regional and not just local. The magnitude of the direct normal irradiance trends in DLR-ISIS grid boxes corresponding to the ground stations range between .17 and .41 W/m² per year, compared to a range of .20-.47 W/m² per year in measurements from the three ground stations. Unlike the full trends in Section 4.1, for the shorter available time period of 1984-2004, none of the trends is statistically significant at the 95% confidence level.

The DLR-ISIS time series uses input data that includes temporal fluctuations in cloudiness and stratospheric aerosols, however, it only includes monthly climatologies of tropospheric aerosols. Yet the trends in direct normal annual average anomalies are of similar magnitude to those of the SRML surface measurements. This suggests that, at least for the shorter time period of 1984-2004, the trends in all-sky averages are not caused primarily by changes in tropospheric aerosols.

The volcanic eruptions appear to be the strongest factor in direct normal irradiance trends from 1984-2004 in both ground measurements and the DLR-ISIS satellite-derived data set. Eliminating the years most heavily impacted by volcanic aerosols (1984, and 1991-1993) in the DLR-ISIS time series gives negative trends of 0 to

-0.13 W/m^2 per year. Removing those same years in the SRML measurements gives trends between -0.38 and 0.19 W/m^2 per year. That is, removing the volcanic years reduces the trends in the DLR-ISIS by between 0.3 and 0.4 W/m^2 per year, and in the surface measurements by between 0.2 and 0.6 W/m^2 per year. The volcanic aerosols have an impact on trend calculations in direct normal all-sky irradiance on the order of the trends themselves. The impact of volcanic eruptions on direct normal irradiance will be seen more clearly in Chapters V and VI.

Total irradiance trends from the UO SRML were also compared to the DLR-ISIS data. While the SRML measurements increase slightly, 0.01 - 0.18 W/m^2 per year, the DLR-ISIS total irradiance trends show statistically significant decreases of 0.13 - 0.41 W/m^2 per year where all trends [Riihimaki *et al.*, 2006]. These results are curious. They could be indicative of a lack of change in tropospheric aerosols in the DLR-ISIS data. That seems unlikely, however, as trends in surface measurements of direct normal irradiance do not increase more strongly than the DLR-ISIS data. The differences in trends could also be related to a difference in the spatial scales or errors in the atmospheric measurements input into the DLR-ISIS calculation. The comparisons between UO SRML and DLR-ISIS total irradiance illustrate how difficult it is to determine a change in aerosols from total irradiance.

CHAPTER V

ANALYSIS OF CLEAR AND CLOUDY SKY IRRADIANCE

5.1. Introduction

Clouds modulate shortwave irradiance at the earth's surface with the most variability of any atmospheric component. On a cloud-free day, the solar irradiance at the surface varies regularly depending primarily on the solar zenith angle as seen in the first half of the day in Figure 5.1. Clear-sky atmospheric constituents, like gases, water vapor, and aerosols, usually vary little over the course of the day. A cloud, on the other hand, can change the total shortwave irradiance by several hundred W/m^2 in a few seconds. That variability can be seen in the last half of the day in Figure 5.1. This deviation from smooth variations under clear skies allows surface measurements to be separated into clear and cloudy skies.

Because this study is primarily examining the impact of aerosol changes on the atmosphere, the data were analyzed in a way that would maximize the impact of aerosols. First, clear and cloudy skies were separated in order to examine only clear skies. The method of identifying clear skies is described in the following section. Section 5.3

describes the small positive trend seen in clear-sky data and its possible causes. The last section of this chapter describes analysis of possible changes in clouds that contribute to trends and also to the statistics of clear-sky analysis.

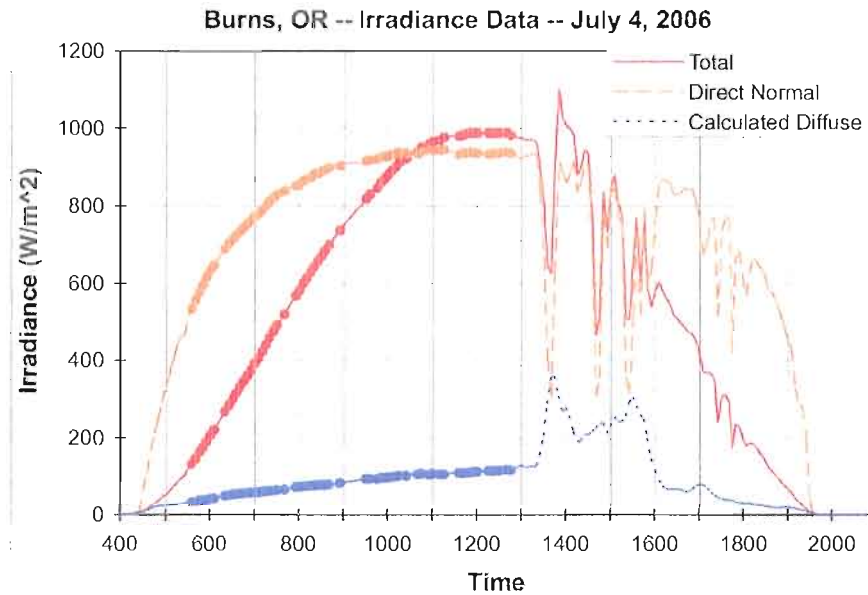


Figure 5.1. Daily plot for Burns with example of periods identified clear by the *Long and Ackerman* [2000] method. Clear measurements are plotted with large dots for total, direct normal, and diffuse irradiance. The lines show all measurements for the three components as identified in the legend. The smoothly varying period before 1300 is identified as clear. After 1300, the more rapidly varying irradiance shows the impacts of clouds.

5.2. Method of Detecting Clear Skies

Long and Ackerman [2000] developed an automated system to detect clear skies from total and diffuse shortwave irradiance measurements. The *Long and Ackerman* method (hereafter called the SWC method or algorithm) is now well established and has

been used to analyze data from various radiometer networks [e.g., *Wild et al.*, 2005; *Augustine et al.*, 2003]. The algorithm was originally developed using total and diffuse irradiance measurements at 1-minute time resolution, though has been tested with 3 and 5-minute resolution data as well. The long-term data available in the SRML network consists of 5-minute measurements of total and direct normal irradiance. Diffuse irradiance can be calculated from the difference in total and direct irradiance, but this calculated diffuse has larger errors than measured diffuse.

Thus, in addition to giving a brief description of the SWC method used to identify clear skies (5.2.1), a discussion of the differences between using calculated and measured diffuse with the SWC algorithm is given in Section 5.2.2. Using the calculated diffuse irradiance does not erroneously identify clear periods, but it does reduce the number of data points identified as clear. (Appendix C describes a comparison between the manually identified clear skies used for calibration correction in Chapter III and the automated process used here as another check on the accuracy of the SWC method.)

5.2.1. Description of Long and Ackerman Method

The *Long and Ackerman* [2000] clear-sky identification algorithm (SWC algorithm) screens data to remove cloudy periods using four criteria. The criteria are explained in more detail in the noted reference, but are summarized here. A determination of clear sky for a given time interval requires a positive conclusion on each of four criteria about the total or diffuse irradiance. First, the total irradiance (normalized

by a function of zenith angle) must fit between maximum and minimum limits for clear-day values. Second, the diffuse irradiance must fit below a maximum limit. Clouds increase scattering so they decrease direct irradiance and increase diffuse irradiance. The total irradiance is a sum of both the direct and diffuse components, and is generally also lowered by the presence of clouds as more radiation is reflected into space. A positive cloud effect can occur in ground radiometer measurements, however, when clouds do not block the direct beam, yet the diffuse irradiance is still large from partially cloudy-sky scattering and reflection. Thus, total irradiance has maximum and minimum clear-sky bounds but diffuse irradiance only needs a maximum limit. Besides magnitude tests, variability is also an important criterion in differentiating clear and cloudy skies. The third test compares the variability between consecutive total irradiance measurements of the smallest time interval available (1 minute or 5 minutes) to the corresponding top of atmosphere down-welling irradiance variability for the same time step. At any given point at the top of the atmosphere, the change in flux between time steps is caused primarily by the changing solar zenith angle. That change is large in the morning and evening, but small around noon. The change in surface irradiance is modulated both by the changing zenith angle and the presence of elements of the atmosphere that absorb and scatter solar radiation. Cloudy periods have higher variability than clear periods. Thus, to be defined as clear, the rate of change of the total irradiance must fit into an envelope around the top of atmosphere variability. The fourth and final screen for clouds examines the diffuse ratio (diffuse/total irradiance) normalized by a power law function of the cosine of the zenith angle. The exponent is determined by fitting the diffuse ratio values

from clear periods over the course of a day. The standard deviation of the ratio over the 15-minute interval (or 11 minutes for 1 minute data) surrounding the measurement must remain below a maximum limit to be labeled clear. This is essentially measuring the variability of the diffuse, which is more sensitive than the total irradiance to thin or scattered clouds. The results of this test with calculated diffuse irradiance is discussed more in Section 5.2.2.

The limits set on the screening criteria, particularly the limits set on the magnitude and variability of the diffuse irradiance, determine what is considered clear. This study used limits recommended to work well with 5-minute irradiance data by C.N. Long (personal communication). The maximum clear-sky diffuse limit was set to $170 (\cos\theta)^{1/2}$ in W/m^2 , where θ is solar zenith angle. The maximum limit set to the standard deviation of the normalized diffuse ratio was .0012. This diffuse ratio is defined as the diffuse irradiance divided by the total irradiance. It is normalized by fitting the daily clear values of the diffuse by a power law function of the cosine of zenith angle. The limit on the standard deviation is subjective, but was found to work well with multiple data sets [see discussion in section 3.4 in *Long and Ackerman, 2000*]. Validation of the identification algorithm showed that it matched human observations, Whole Sky Imager data, and lidar cloud property retrievals within the limitations of these measurement methods [*Long and Ackerman, 2000*]. The algorithm may identify conditions of haze or sub-visual cirrus as clear. Clouds on the horizon may also be identified as clear because these clouds have too small an impact on the total irradiance to detect. Thus, *Long and Ackerman* describe the algorithm as identifying clear-sky

measurements for a field of view of 160° rather than the complete, 180° , field of view of the instrument.

5.2.2. Checking the Accuracy of Clear-sky Identification Using Calculated Diffuse Irradiance

The data used in developing the clear-sky identification algorithm differ in two ways from the data used in this study. The SWC algorithm was developed using one-minute measured total and diffuse shortwave irradiance. The data available for this study are primarily 5-minute resolution measured total irradiance and diffuse irradiance calculated from total and direct normal measurements. The time resolution introduces some additional difficulties in screening for variability, but algorithm settings have been determined that would be equivalent for 5-minute resolution measurements [*Long and Gaustad, 2004*]. Using calculated instead of measured diffuse irradiance has a larger impact on the ability to detect clear skies with this method. Diffuse irradiance is easily calculated from the difference of the other two components. However, because the calculation is a difference, the errors propagate in such a way in the calculation that relatively small percentage errors in the total and direct measurements can produce much larger percentage errors in the diffuse irradiance. Of particular importance is the systematic error in the cosine response of the pyranometer. As described in Chapter II, this produces a systematic difference between measurements at different zenith angles. When this error is transferred to the calculated diffuse irradiance, it can change the shape

of the curve over the day. Because part of the clear-sky algorithm uses a fit to the ratio of the diffuse to the total irradiance, the cosine response error impacts the accuracy of the clear-sky identification. Eugene has measurements at one-minute resolution of diffuse as well as total and direct normal irradiance since 2001. The one-minute measured diffuse irradiance was used to compare the impact of the measured and calculated diffuse on the accuracy of clear-sky identification.

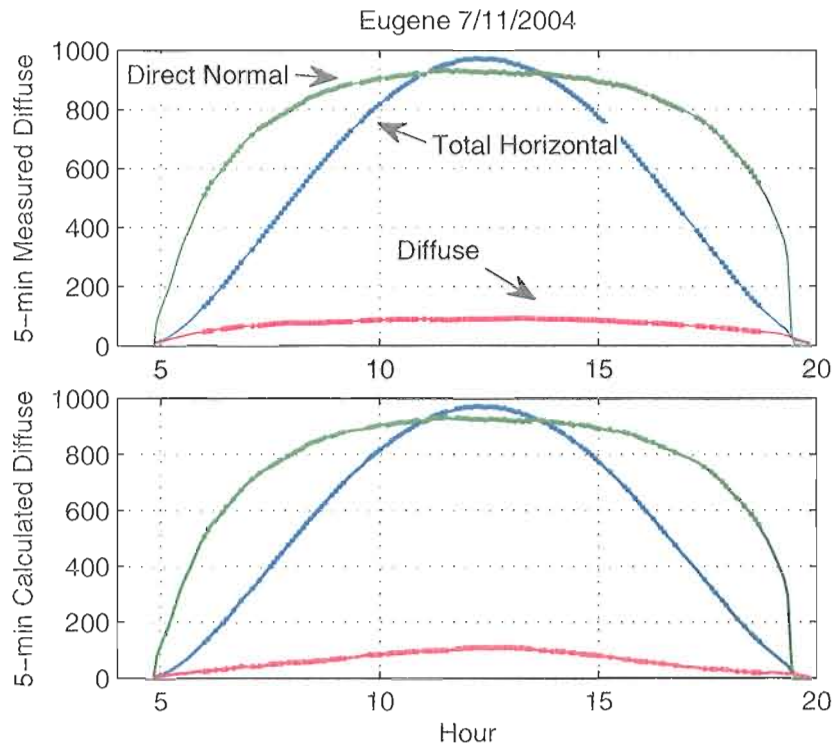


Figure 5.2. Total, direct normal, and diffuse irradiance for July 11, 2004 at Eugene. More clear periods (plotted as solid circles) are identified with the SWC algorithm when using measured diffuse irradiance (top) than calculated diffuse irradiance (bottom).

The calculated diffuse does not appear to introduce erroneously defined clear-sky measurements, though it eliminates some periods defined as clear with the measured diffuse. This can be seen in Figure 5.2 where total, direct normal, and diffuse irradiance

are plotted from July 11, 2004 at Eugene. Solid circles indicate periods that have been identified clear. Using measured 5-minute diffuse irradiance (top plot) with the SWC algorithm finds more periods clear than using calculated 5-minute diffuse (bottom plot). Note the different shape between the measurements of diffuse in the two plots. Using the measured diffuse, the algorithm identifies all the same periods clear as with the calculated diffuse, but also identifies additional clear periods. The reason for this difference is based on the standard deviation of the normalized diffuse ratio.

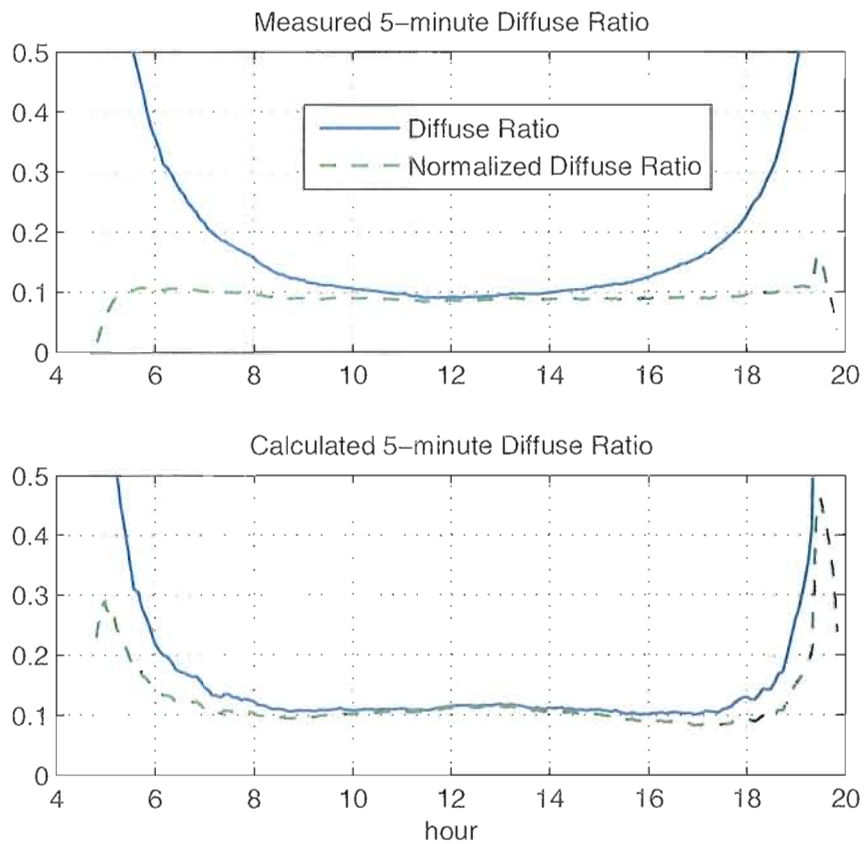


Figure 5.3. Ratio of diffuse irradiance to total irradiance measurements (diffuse ratio) shown in solid lines. The dashed lines show the diffuse ratio normalized by a power law fit of the cosine of the zenith angle. The diffuse ratio and normalized diffuse ratios have different shapes when using measured (top) or calculated (bottom) diffuse. Data from same day as Figure 5.2.

Figure 5.3 plots the diffuse ratio and normalized diffuse ratio for the day, once again using both the measured and calculated diffuse. The curve of the diffuse ratio using calculated diffuse has a different shape, which makes the normalization not as effective. Figure 5.4 plots the standard deviation of the normalized diffuse ratio for a 15-minute period centered on each data point. Many more points from the calculated diffuse data set are above the cutoff line of .0012, and are not identified as clear.

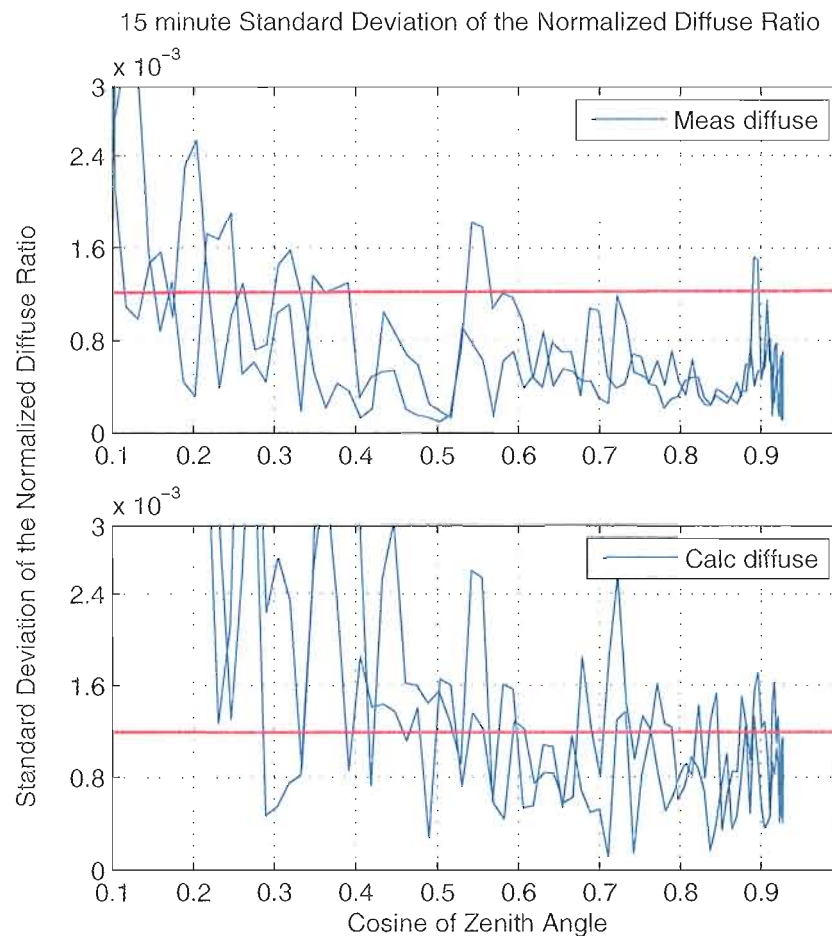


Figure 5.4. The standard deviation of the normalized diffuse ratio for calculated diffuse (bottom) is sometimes higher than that of the measured diffuse (top) leading to fewer periods identified as clear. The maximum standard deviation allowed for a measurement to be declared clear is plotted with a red horizontal line in each plot. Data for same day as Figure 5.2.

Figure 5.5 shows a graph of all direct normal measurements identified as clear during 2004 between the zenith angles of 65 and 75 degrees. Fewer points are identified clear using the calculated diffuse, but overall, the data represents the same range without adding outliers.

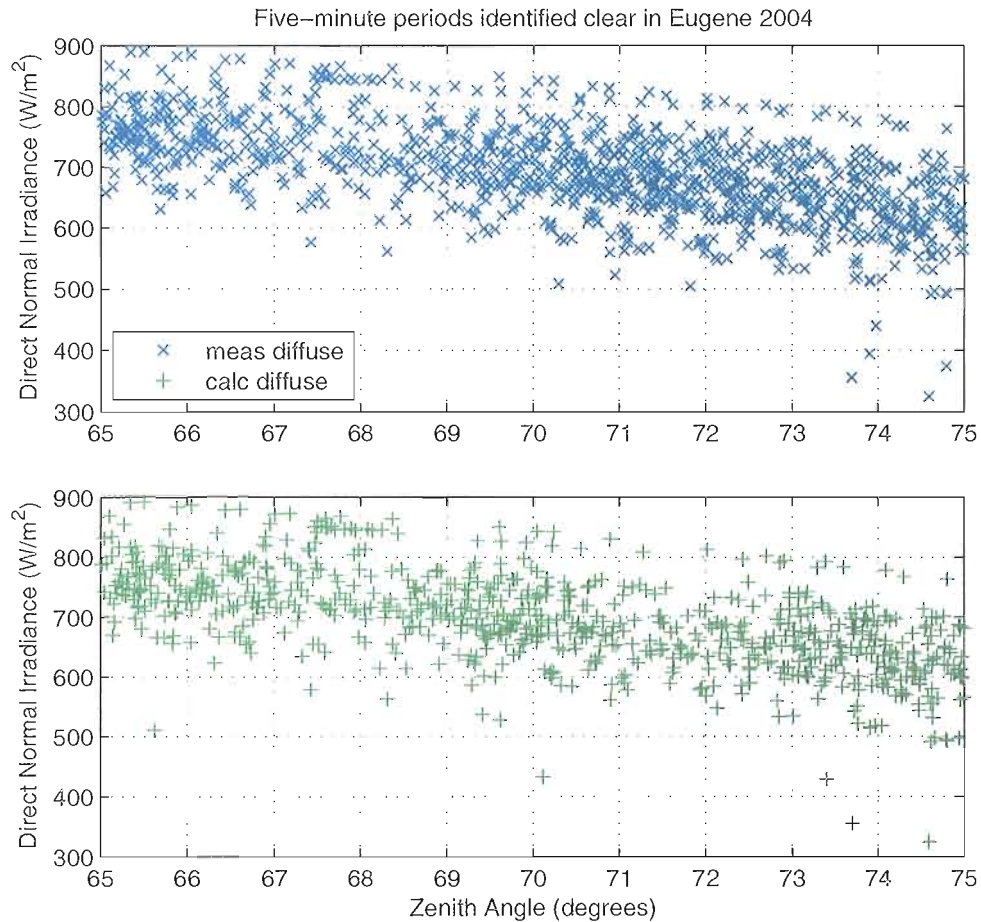


Figure 5.5. Direct normal irradiance measurements identified as clear in Eugene in 2004 between zenith angles of 65-75°. More clear periods are found using the measured diffuse, but no erroneous points are found using the calculated diffuse.

Monthly average clear-sky direct normal irradiance was calculated for clear periods between zenith angles of 65-75 degrees using periods identified clear from 1-

minute measured diffuse and 5-minute calculated diffuse. The comparison of the two was used to evaluate the uncertainty of identifying clear periods using calculated diffuse on the analysis that will be done in the following sections. The anomalies of these monthly averages from typical values are plotted in Figure 5.6. The difference between the two time series is shown in the lower part of the figure. The standard deviations for both time series and the differences between the two time series are given in Table 5.1. The standard deviation of the differences is about half of the variation of the monthly average time series used in this study. The largest differences occur in the winter as would be expected because winter has the fewest clear periods.

Table 5.1. Standard deviations of clear-sky monthly average anomalies

<i>Zenith angle</i>	<i>Meas. 1-min diffuse</i>	<i>Calc. 5-min diffuse</i>	<i>Difference</i>
65-75	23.6 W/m ²	24.5 W/m ²	12.2 W/m ²
25-35	9.0 W/m ²	8.5 W/m ²	4.1 W/m ²

Figure 5.7 shows monthly averages of clear-sky direct normal irradiance determined using 1-minute measured and 5-minute calculated diffuse for zenith angles between 25-35 degrees. The standard deviations of the monthly anomalies and the differences between the two time series are smaller in this zenith angle range, but the standard deviation of the differences is still about half of the variation.

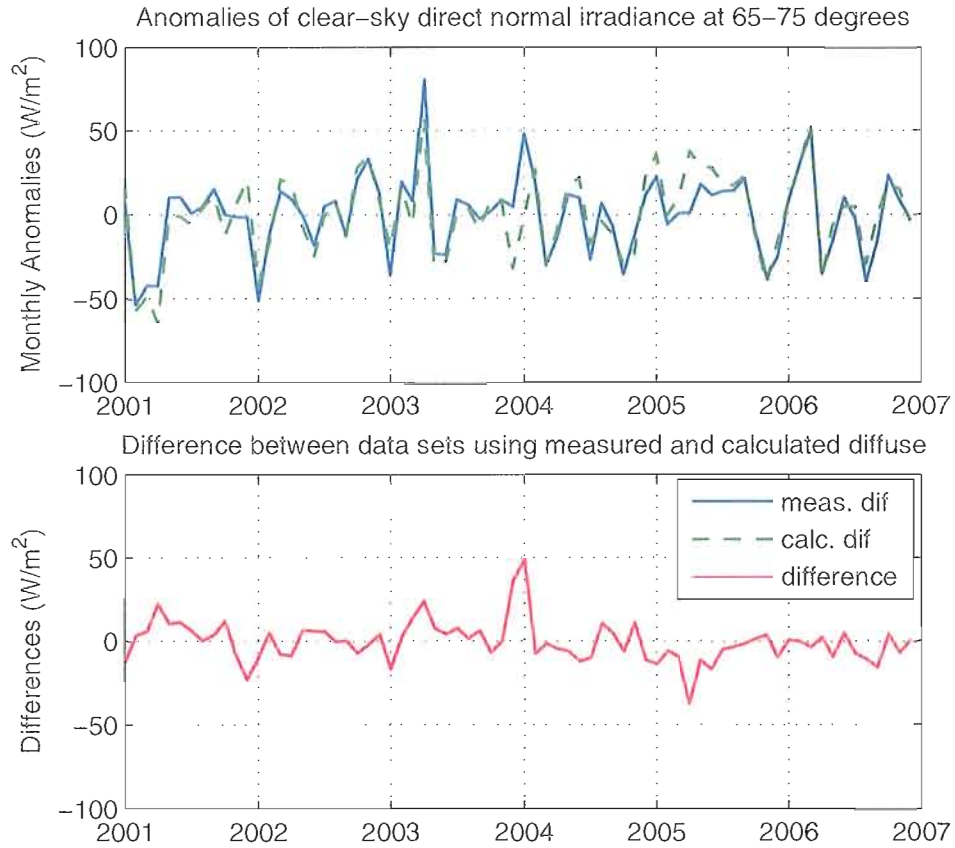


Figure 5.6. Monthly average anomalies of clear-sky direct normal irradiance for zenith angles 65-75°. Clear periods are determined using measured (solid line) and calculated diffuse (dashed line) in the SWC algorithm. The difference between the two time series is shown in the lower plot.

5.3. Clear-sky Data Analysis

Clear-sky direct normal irradiance is used to look for changes in aerosol concentrations. Several features can be seen that may be related to aerosols. The impact of the volcanic eruptions of El Chichón and Mt. Pinatubo are clearly seen in the clear-sky irradiance time series. All measurement sites also show low clear-sky irradiance values in

the years preceding the eruption of El Chichón (1980-1981). Linear trend lines fit to Eugene and Burns data from 1987-2007 (excluding June 1991-December 1994) are positive and significant, indicating a decrease in aerosol loads over the time period. Clear-sky direct normal irradiance measurements in Hermiston do not follow the same change, but appear to decrease in a step-function-like fashion around June of 2003.

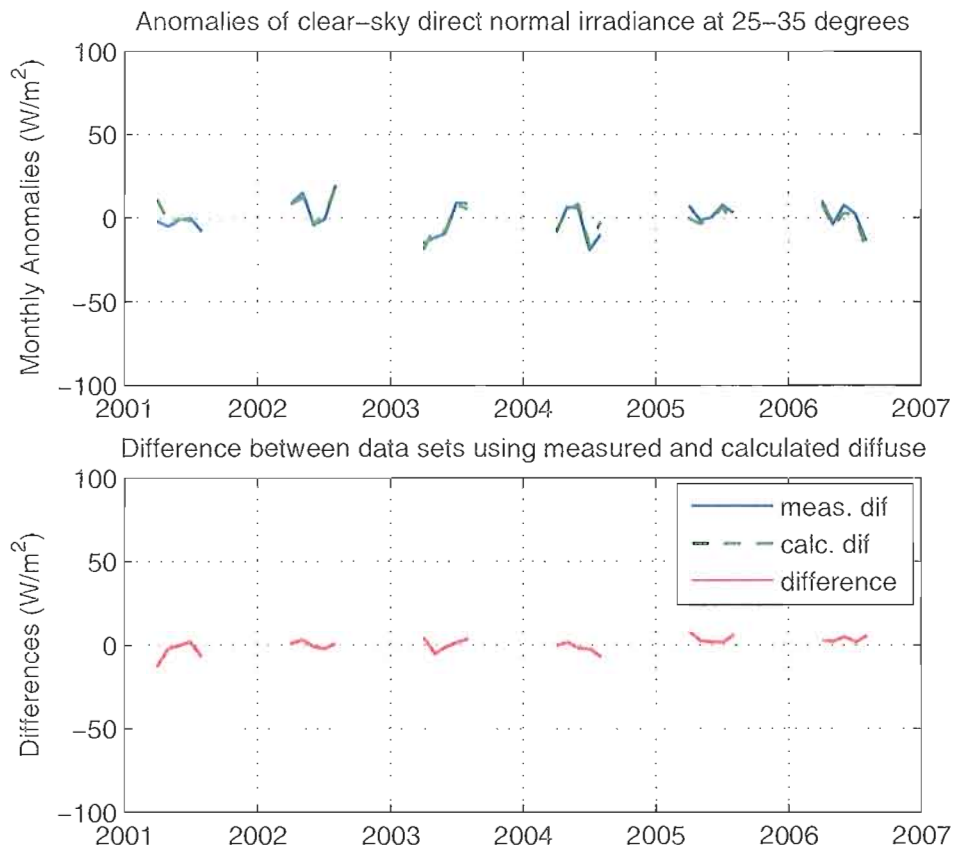


Figure 5.7. Monthly average direct normal irradiance from clear periods for zenith angles of 25-35°. Same method as Figure 5.6. Because the solar zenith angle only moves above 35° in the summer months at these latitudes, there are fewer points to compare.

5.3.1. Method of Analysis

Analyzing clear-sky irradiance measurements allows a more careful examination of the impacts of changes in aerosols on surface irradiance than looking at all-sky data. In order to maximize any signal from aerosol changes, two other choices were made in the analysis. First, direct normal data was used because it is more sensitive to scattering than the total irradiance as it measures only what comes directly from the sun and not what is scattered outside the incident beam. It is also a good choice because the instrument measuring direct normal irradiance does not show significant degradation, as described in Chapter III. Second, the analysis is restricted to high zenith angles because the long atmospheric path lengths at these angles increase scattering. The zenith angle range of 65-75 degrees was chosen for trend analysis because those angles are well represented in all months. The minimum winter zenith angle at the winter solstice at these latitudes is slightly less than 65°.

Monthly averages of the clear-sky direct normal irradiance from zenith angles of 65-75° are then deseasonalized by subtracting typical monthly values. The typical values are calculated as the long-term mean of monthly averages, excluding the months most strongly impacted by volcanic eruptions (March 1982-December 1985 and June 1991-December 1994).

5.3.2. Clear-sky Results

The monthly anomalies plotted in Figure 5.8 show clearly the impact of the volcanic eruptions of El Chichón and Mt Pinatubo. The eruptions cause decreases of the direct normal irradiance at these zenith angles of up to 200 W/m^2 . This is equivalent to a percentage decrease of up to 25%. The large drop from volcanic eruptions is clear evidence of the sensitivity of these monthly anomalies to events of known large aerosol concentrations. It is also clear from Figure 5.8 that those volcanic events impact the clear-sky solar radiation much more strongly than any changes in anthropogenic aerosols and, in fact, 20-55% (depending on the site) of the trends in annual averages of direct normal irradiance under all-sky conditions seen in Chapter IV can be explained by these events.

Any change in background aerosols is also of interest. Trends are fit to the time series after removing measurements from March 1982-December 1985 and June 1991-December 1994. The trends are calculated for three time periods, 1980-2007, 1987-2007, and 1997-2007. Table 5.2 shows the results of those trend calculations and their uncertainties. Uncertainties are calculated as twice the standard error of the trend including the assumption of autocorrelation of order one as described in Chapter IV. The trends from 1980-2007 and 1987-2007 are both positive and significant at Eugene and Burns. While the trends for those two time periods at Hermiston are positive, they are much smaller in magnitude than at the other two sites and not statistically significant. As seen in the trend calculations from 1997 to 2007, the Hermiston time series significantly decrease in the last decade. The 1987 to 2007 trend lines are plotted in Figure 5.8. This

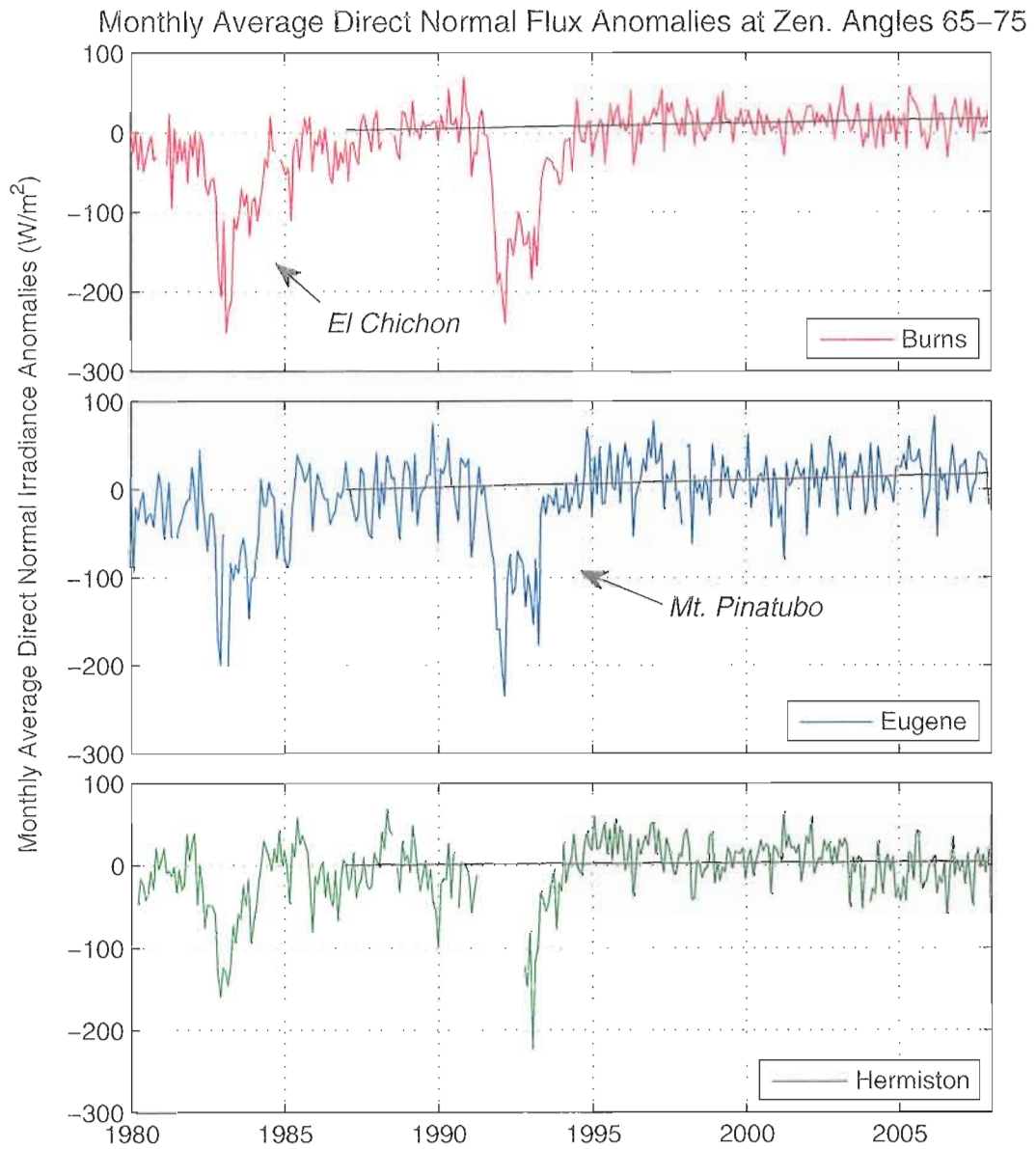


Figure 5.8. Monthly anomalies of clear-sky direct normal irradiance for solar zenith angles of 65-75 degrees. Trends are calculated for the years 1987-2007 without including 1991-1994, the years most heavily impacted by the volcanic eruption of Mt. Pinatubo. All three sites show positive trends, though at Hermiston, the trend does not represent the data well, as recent years appear to decrease.

period of time is of particular interest because it corresponds to the timing of worldwide reports of increasing solar radiation [e.g., *Wild et al.*, 2005] and decreasing globally averaged anthropogenic aerosol emissions [*Streets et al.*, 2006]. The portion of this trend attributed to anthropogenic aerosols is investigated in Chapter VI.

Table 5.2. Trends in background clear-sky direct normal irradiance anomalies 65-75° (in W/m²/year)

	<i>Burns</i>	2σ	<i>Eugene</i>	2σ	<i>Hermiston</i>	2σ
1980-2007	1.43	.38	1.37	.48	.51	.63
1987-2007	.80	.52	.88	.68	.11	.89
1997-2007	-.22	1.01	.85	1.52	-2.15	1.53

Systematic measurement error is not a likely cause of any of the trends given in Table 5.2. The strongest systematic pyrheliometer error is calibration. As was described in Chapter III, however, these pyrheliometers remain remarkably constant over time and so no change in calibration number was made to the instruments in their time in the field. Thus, any calibration error from a particular instrument would result in a decreasing trend, meaning the positive trends in Table 5.2 would be underestimated rather than overestimated. Introducing a new instrument at a site could cause a step function that might appear as a positive trend. That is not likely the case here, however, as the changes seen do not correspond with changes in instruments. At Burns, in particular, the same NIP was used in the field from July 1987 to the present. Thus the direct normal irradiance from 1987-2007 at Burns is almost entirely measured with one instrument. The dip in Hermiston data in 2003 is also not caused by an instrument change because the same NIP was used there from 1999 to 2007. The data logging system was changed in 1995 at all

three sites, though both the data logging system used prior to and that used after 1995 were estimated to contribute an uncertainty of less than .5% to the measurements.

To better compare the data between sites, monthly average data was smoothed to look for overall structure. Figure 5.9 shows an example of this smoothing for the data at Burns, with the red dotted line showing the monthly average deviations from typical values at 65-75°, and the black solid line showing the smoothed data. The smoothing is done with a MATLAB robust lowess filter with a span equivalent to a year. The lowess smoothing technique replaces each point with a least squares linear regression over the span surrounding that point, with the contribution of the neighbors within the span weighted by their distance from the point of interest. The filter also uses a robust screening that removes outliers from the linear regression beyond six median absolute deviations from an initial smoothing iteration.

Figure 5.10 shows the smoothed curves from all three sites together. At times, two or three of the datasets have very similar structures. For example, both Eugene and Burns show high values in the summer of 2005, possibly from a very clear summer.

One of the most notable features that all three sites share is the comparatively low values at the beginning of the time series (1980-1981). These low values explain much of the strong positive trends from 1980-2007 given in Table 5.2. The causes of these low values are unknown, but the existence at all three sites suggests a regional cause, possibly high aerosol loads. No systematic change in instrumental setup has been found that would cause all three of these sites to give low values in those years because systematic instrument errors tend to decrease over time rather than increase.

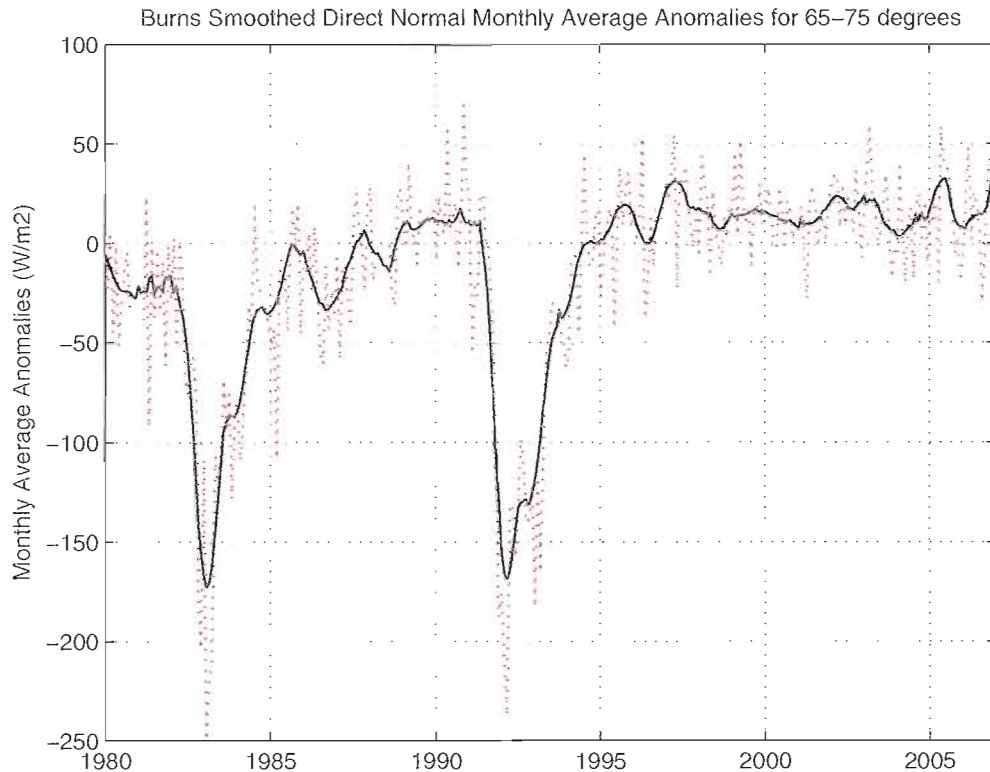


Figure 5.9. Example of smoothing the monthly average Burns data from Figure 5.11 with a robust lowess filter with a one-year span.

One possible cause for the low values is the eruption of Mt. St. Helens in 1980, though the eruption is not thought to have impacted atmospheric transmission for a long period of time. *Michalsky and Stokes* [1983] found that the baseline turbidity returned to levels consistent with 1979 turbidity on the order of days to a few weeks after eruptions of Mt. St. Helens in 1980. Their analysis was based on direct normal spectral measurements in Richland, Washington, ~50 miles north of the Hermiston station. Stratospheric lidar measurements in Germany, however, indicate an increase in backscatter following the eruption of Mt. St. Helens in May of 1980 and the eruption of Alaid in 1981 [*Jäger*, 2005]. More careful comparisons between measurements of these

volcanic emissions and solar irradiance would be needed to determine whether the low values in the Oregon data could be caused by these volcanic eruptions.

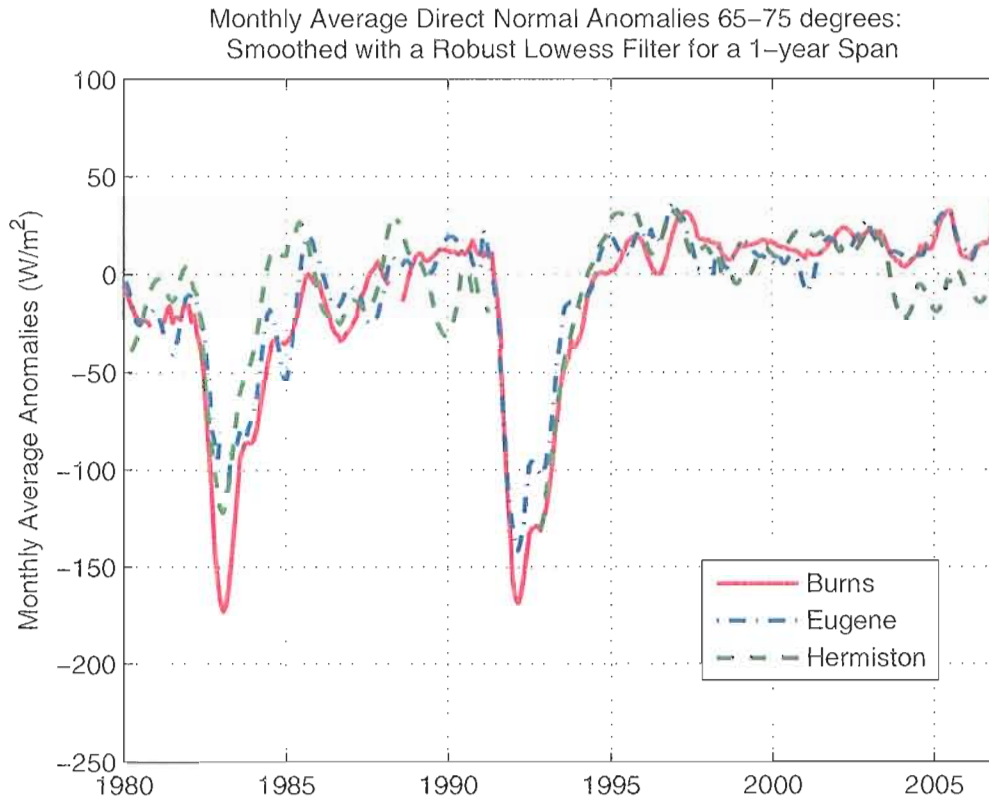


Figure 5.10. Smoothed monthly average time series from Figure 5.8 for all three sites.

Figure 5.10 also shows that Hermiston has lower values at the end of the time series compared to the other sites, explaining the smaller trend from 1987-2007 at this site compared to the other two. The Hermiston time series steps down around June of 2003. Some problems have been found in Hermiston measurements in recent years caused by a decreased frequency of station maintenance. Less frequent cleanings or alignment could cause a decrease in irradiance, though no sudden change happened with station maintenance in 2003. To confirm that maintenance issues did not cause the

decrease in irradiance, the measurements were compared to direct normal irradiance calculated from a rotating shadowband pyranometer (RSP) at the site. Clear-sky RSP measurements also show lower irradiance values around 2003, and do not appear to deviate systematically from the direct normal NIP measurements in June of 2003. Thus, instrument maintenance does not appear to be the cause of the 2003 decrease at Hermiston.

A second possible explanation for the decrease in irradiance at Hermiston is an increase in local aerosol concentrations. According to information from the Oregon Department of Environmental Quality, a number of possible particulate sources exist in the region surrounding Hermiston, including a coal fired power plant in Boardman, two natural gas driven electricity and steam generation plants, a food processing plant in Hermiston, and incineration at the Umatilla Chemical Depot (<http://www.deq.state.or.us/umatilla/factsheets/MaximumPermittedAirEmissions.pdf>). Hermiston is also an agricultural area, with sources of dust and other particulates. Direct comparisons of irradiance data with emissions from these sources or aerosol concentration measurements would be helpful to determine whether the decrease in irradiance is caused by particulates.

No changes have yet been found for any of these particulate sources that correspond directly to the apparent timing of the step function in the measurements, though two of these sources began operating within a year of June 2003. According to the Calpine website, the natural gas powered steam and electricity generation plant in Hermiston began operations in August of 2002

(<http://www.calpine.com/power/plant.asp?plant=62>). The Department of Environmental Quality's website reports that the Umatilla Chemical Depot (located 8 miles west of Hermiston) conducted trial burn operations in the beginning and end of 2003 and more continuous incineration sometime afterwards (<http://www.deq.state.or.us/umatilla/cdp.htm>). It is not known whether the emissions from these sources would be sufficient to impact the clear-sky direct normal irradiance in the manner observed at Hermiston.

Clear-sky direct normal time series from high and low zenith angles are compared to further investigate whether the changes in the clear-sky time series are caused by aerosols. Average monthly anomalies in the summer (June and July) are plotted in Figure 5.11 for zenith angles of 65-75 degrees and also 25-35 degrees. Table 5.3 gives the magnitudes and uncertainties of trends calculated for these time series. The trends are not strong enough at the lower zenith angles to produce significant trends except in Eugene from 1980-2007. Comparison of the impact of aerosol concentration changes between the two zenith angle slices should give stronger variation for the higher zenith angle range. In the years 1982 and 1992 the dips in direct normal irradiance are stronger at 65-75 than the lower zenith angles, which is expected from the impact of volcanic aerosols. Clear-sky direct normal irradiance is lower than average in the first two years of data (1980-1981) for both zenith angle ranges. The greater decreases in irradiance at the higher zenith angle range than the lower zenith angle range is consistent with aerosol concentrations causing the low values.

Table 5.3. Trends in summer clear-sky direct normal irradiance anomalies (in $W/m^2/year$)

	<i>Z. Ang.</i>	<i>Burns</i>	2σ	<i>Eugene</i>	2σ	<i>Hermiston</i>	2σ
1980-	25-35	.53	.87	1.02	.49	.12	1.12
2007	65-75	1.71	.83	1.25	.86	.37	1.33
1987-	25-35	-.48	.92	.70	.79	.32	1.57
2007	65-75	.55	1.21	.63	.75	-.41	1.55

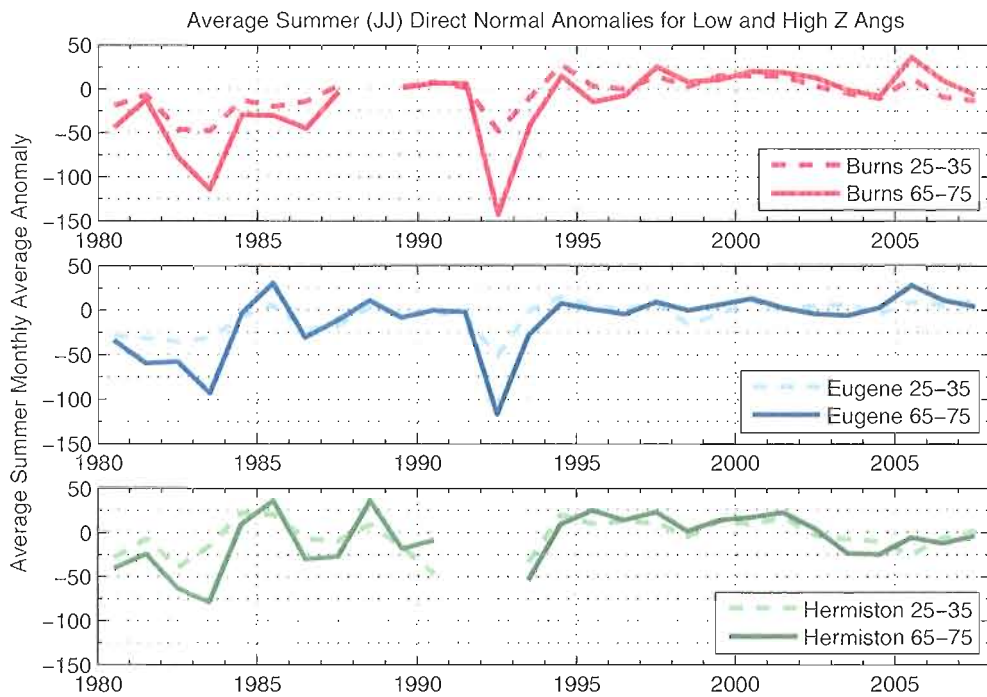


Figure 5.11. Summer averages of 5-minute resolution clear-sky direct normal irradiance for zenith angle ranges of 65-75 degrees and 25-35 degrees at each site. The averages are calculated for June and July.

5.4. Cloud Fraction Calculations

The increase in solar radiation described in Chapter IV may be due in part to changes in clouds. In addition to identifying clear periods, the *Long and Ackerman* [2000] algorithm has been expanded to estimate the fraction of the sky covered by clouds, or cloud fraction, from irradiance measurements [*Long et al.*, 1999]. Seasonal and annual average cloud fraction decreases at Eugene and Burns, coming primarily from a decrease in cloud fraction in the summer.

Cloud fraction is calculated using a previously defined correlation fit between the normalized diffuse cloud effect (D_n) and measured fractional sky cover. D_n is defined as the difference between diffuse irradiance measurements and the estimated clear-sky diffuse irradiance found by a fit to clear periods, normalized by the total irradiance. Screening algorithms are applied for overcast and clear skies, and then cloud fraction is determined from a correlation relationship with D_n . The result is an accuracy of 10% for 15-minute average cloud fraction [*Long et al.*, 1999].

As with the clear-sky identification, the impact of the cosine response errors of the calculated diffuse impacts these cloud fraction retrievals. Cloud fraction determined with calculated diffuse irradiance deviates from the cloud fraction determined by measured diffuse irradiance according to zenith angle. To minimize that effect, daily average cloud fraction was used in this analysis. The period from January 1, 2001 to December 17, 2006 in Eugene, which contains both measured and calculated diffuse, was used to determine the magnitude of the bias introduced by using calculated diffuse

irradiance in the cloud fraction calculations. In Figure 5.12, the distribution of the difference between daily average cloud fraction determined with the two different diffuse data sets shows a slightly biased average with a small spread. The average offset of the ratio between the two is -0.01, meaning that the cloud fraction determined with calculated diffuse is slightly low compared to that of the measured diffuse. The standard deviation is 0.03. The cloud fraction retrievals are only considered accurate to 0.1. Thus, the offset is an order of magnitude smaller than that uncertainty.

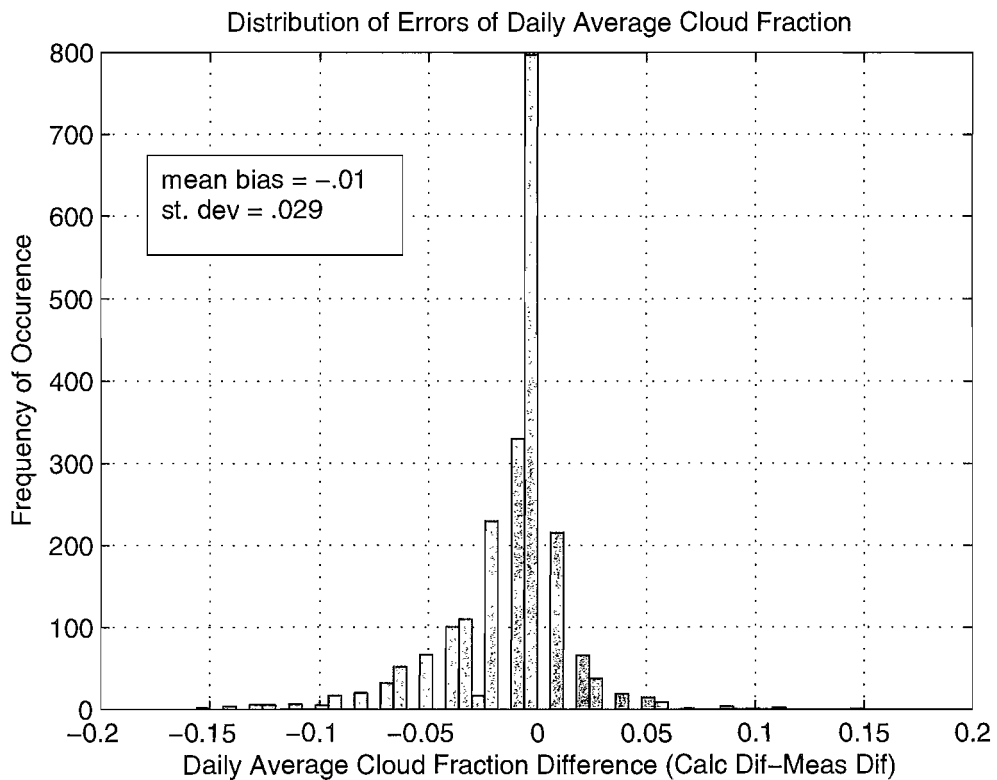


Figure 5.12. Histogram of difference between daily average cloud fraction determined using one-minute measured-diffuse and five-minute calculated diffuse. Cloud fraction is calculated using the SWC algorithm.

Because of the seasonal zenith angle dependence, cloud fraction derived from calculated diffuse measurements also has seasonal biases. Table 5.4 shows the mean bias and standard deviation of seasonal comparisons between cloud fraction determined using measured and calculated diffuse in Eugene for the period 2001-2005. The seasonal biases are also small, with the largest bias in summer. This is expected because summers have the most frequent clear skies, when the error of the cloud fraction calculation is the highest. The percentage standard deviations are small, less than 2% for all seasons.

Table 5.4. Seasonal bias and standard deviations between cloud fraction determined from calculated and measured diffuse irradiance at Eugene, 2001-2005

	Winter	Spring	Summer	Fall
Mean bias	-.0013	-.0160	-.0174	-.0084
Std Dev.	.0084	.0051	.0058	.0050
% St. Dev	1.0%	.8%	1.7%	.8%
Mean Cloud Fraction	.8295	.6726	.3440	.6002

Table 5.5. Cloud fraction trends from 1980-2007 (in cloud fraction per year)

	<i>Burns</i>	<i>Eugene</i>	<i>Hermiston</i>
Winter	-0.0024 ± 0.0031	0.0011 ± 0.0019	-0.0020 ± 0.0031
Spring	-0.0016 ± 0.0051	-0.0010 ± 0.0047	0.0010 ± 0.0042
Summer	-0.0078 ± 0.0045	-0.0042 ± 0.0037	-0.0031 ± 0.0049
Fall	-0.0059 ± 0.0029	-0.0006 ± 0.0038	-0.0004 ± 0.0042
Annual	-0.0042 ± 0.0018	-0.0012 ± 0.0016	-0.0002 ± 0.0013

Figure 5.13 and 5.14 show the annual and seasonal average daily cloud fraction values for all three sites. Decreases in cloud fraction can be seen in Eugene and Burns annual averages and summer averages. Table 5.5 gives the values of the trends and the

uncertainty for each season calculated from 1980 to 2007. As in previous trend calculations, the uncertainty is calculated as $2\sigma_{trend}$, where σ_{trend} is the standard error of the slope coefficient including autocorrelation as described in Chapter IV. Of the three sites, only Burns has a stronger annual decrease in cloud fraction than the uncertainty. Using this definition of significance, the summer and fall decreases in cloud fraction at Burns are significant, and the summer decrease at Eugene is significant. Hermiston also shows the strongest decrease in summer, but the trend is not statistically significant.

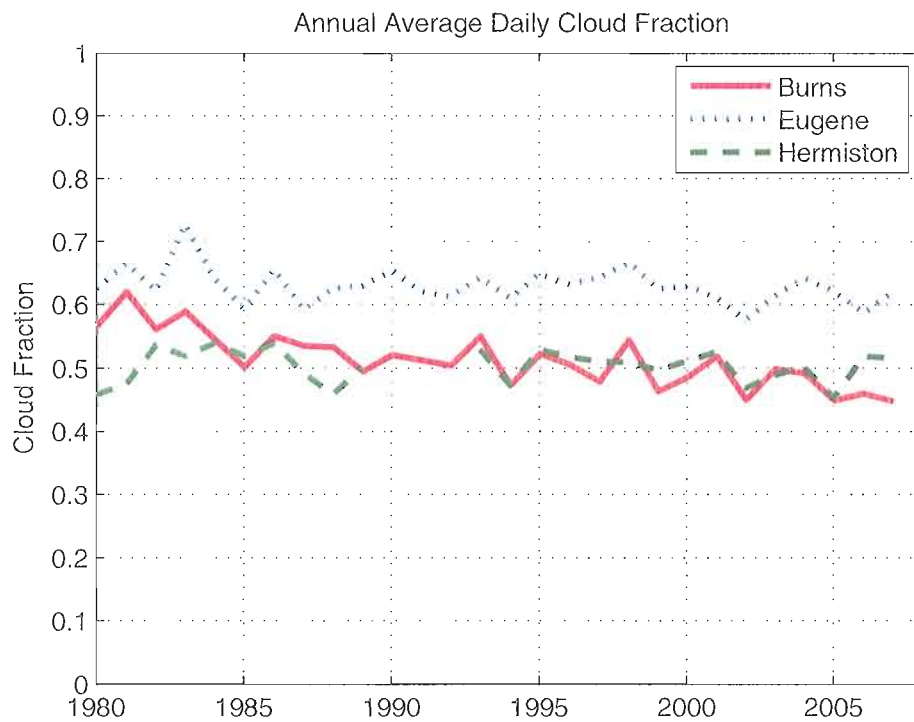


Figure 5.13. Trends in annual average daily cloud fraction.

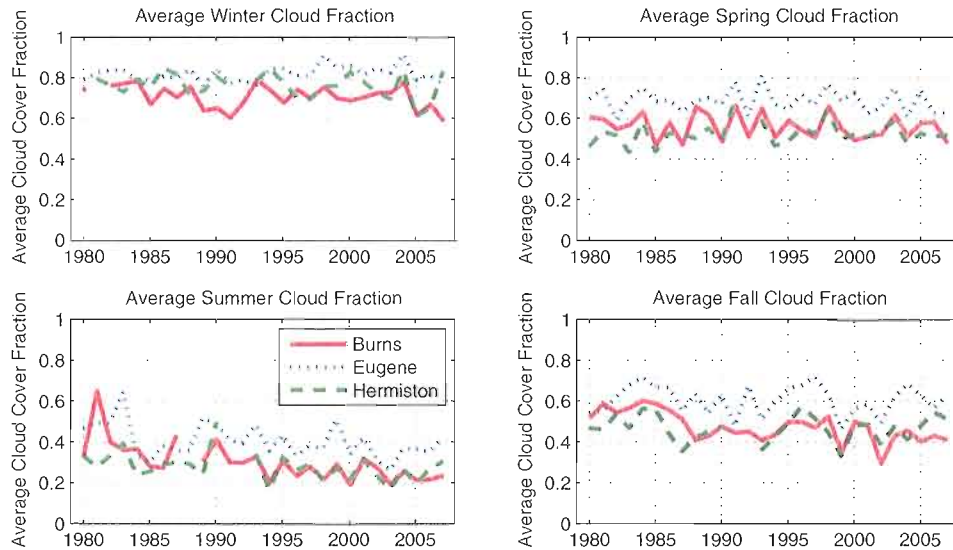


Figure 5.14. Seasonal average daily cloud fraction at the three sites. The strongest change is in the summer where cloud fraction is decreasing at all three sites.

A decrease in cloud cover frequency in the summer time is consistent with the stronger all-sky trend in summer that was found in Chapter IV. It also matches trends from 1971-1996 from human observers. *Warren et al.* [2007] have synthesized cloud observations from surface observations worldwide to determine cloud type and total cloud amount over the period 1971-1996. Two of the surface stations in Oregon were Eugene and Pendleton, which is located about 30 miles southeast of Hermiston. Seasonal trends in total cloud cover for Eugene from 1971-1996 are negative, with a range of -1.34 to -3.43% per decade depending on the season (R.M. Eastman, personal communication). The strongest decrease is in the fall with -3.43%, followed by summer with a decrease of -2.21%. Pendleton also shows a strong decrease in cloud fraction during the fall, -2.99% per decade. The other seasons at Pendleton have weak cloud fraction trends ranging from -.99% per decade to +.06% per decade. The directions of these trends match the cloud

fraction calculations from solar irradiance measurements. The stronger negative trends in Eugene than Pendleton are consistent with the stronger cloud fraction trends derived from Eugene SRML data than Hermiston data. These cloud fraction calculations suggest that a decrease in total cloud amount could be a partial cause of the positive trends seen in all-sky surface solar irradiance, though more accurate cloud measurements are needed to determine how much.

CHAPTER VI
USING RADIATIVE TRANSFER CALCULATIONS TO DISTINGUISH BETWEEN
POSSIBLE CAUSES OF CLEAR-SKY IRRADIANCE CHANGES

6.1. Introduction

To calculate the radiative impact of aerosols, at least three pieces of information are needed: how many particles there are, how big the particles are, and whether they absorb radiation. In practice, many aerosols of different sizes and properties are mixed together in the atmosphere and so aggregate radiative properties of these aerosol concentrations are more useful. One way to include this information, as is done in these calculations, is with wavelength dependent values of aerosol optical depth, single scattering albedo, and the asymmetry parameter. In this study, aerosol extinction information is retrieved from broadband solar irradiance measurements. Only two independent pieces of information are available, the direct normal and total irradiance, and these measurements are broadband rather than at particular wavelengths. This information is not sufficient to determine the size distribution of the particles.

To compensate for the lack of information on particle size, typical aerosol distributions were used from the OPAC model of *Hess et al.* [1998]. *Hess et al.* used the results of many observational studies to define typical properties of several aerosol types like soot, water-soluble land aerosols, sea salt, etc. They then combined these aerosol properties into 10 mixes found in continental and marine environments. The three continental mixes were used in this study that gave results closest to measurements. The continental aerosol mixes differ by the percent of soot they contain, representing different levels of anthropogenic pollution. Varying only the level of soot essentially changes the single-scattering albedo (amount of absorption) but leaves the asymmetry parameter constant (a measure of the scattering size distribution) as most of the scattering is due to the non-absorbing particles.

Radiative transfer calculations were performed to retrieve aerosol optical depth (AOD) at a reference wavelength of 550 nm. Section 6.2 describes the inputs and calculation methods of the radiative transfer model. Significant variation was found between AOD retrievals using the different aerosol mixes. Diffuse irradiance was used to distinguish which mix was the most accurate. This was complicated, however, by the errors in the diffuse irradiance calculated from total and direct normal irradiance measurements. Only measured diffuse was accurate enough to distinguish between mixes. These accurate diffuse measurements were only available in Eugene since 2000, and not available at all at the other sites. As described in Section 6.3, the diffuse irradiance measurements were used to determine an average continental aerosol mix for Eugene in 2001.

As accurate retrievals were not possible with the available data, limits were estimated on the possible change in aerosols represented by the trends calculated in clear-sky direct normal irradiance in Chapter V. The limits were determined by calculating the impact of stratospheric aerosol optical depth and water vapor changes from other input data sets. This work is described in Section 6.4. Estimates of clear-sky annual averages were made using these input data sets and compared to measurements in Section 6.5. Finally, the last section contains a summary of the results of the study.

6.2. Description of Radiative Transfer Calculations

6.2.1. Integro-differential Radiative Transfer Equation

Solar radiation interacts with the atmosphere through scattering and absorption. A typical way to write the equation of radiative transfer is in terms of the single scattering albedo and the optical depth. The single-scattering albedo, ω , is the ratio of the scattering coefficient to the total extinction coefficient. It is a measure of the probability that incoming radiation will be scattered rather than absorbed. The optical depth, τ , is a dimensionless measure of the extinction path length of radiation through the atmosphere. It can be defined as the integral of the extinction coefficient over the height of the atmosphere from the top of the atmosphere to the height of interest:

$$\tau = -\int_{\infty}^z dz' \kappa_{ext}(z'). \quad (\text{Eq. 6.1})$$

For a given wavelength in the solar spectrum, the infinitesimal change in radiance, $dI(\phi, \mu)$, as it passes through a portion of the atmosphere with infinitesimal change in optical depth, $d\tau$, can be described by a radiative transfer equation of the form,

$$\mu \frac{dI(\phi, \mu)}{d\tau} = I(\phi, \mu) - \frac{\omega}{4\pi} \int_0^{2\pi} d\phi' \int_{-1}^1 d\mu' p(\phi', \mu'; \phi, \mu) I(\phi', \mu'), \quad (\text{Eq. 6.2})$$

where μ is the cosine of the zenith angle, ϕ is the azimuthal angle, and $p(\phi', \mu'; \phi, \mu)$ is the scattering phase function. Emission by the atmosphere is negligible at wavelengths of solar radiation associated with significant scattering and absorption by aerosols.

The transfer equation is valid only for monochromatic radiation. The broadband irradiance is calculated by integrating over the entire solar spectrum. This process is very computationally intensive, however, and so instead, the solar spectrum is divided into six wavelength bands in this study. The first of these wavelength intervals is further divided into 10 subintervals. This divides the ultraviolet and visible spectrum into 10 sub-bands. The remaining five intervals divide the near infrared part of the solar spectrum into intervals useful for absorption and scattering. Table 6.1 shows both the wavenumber and wavelength values for these intervals.

Table 6.1. Wavelength intervals used in the radiative transfer calculations

Interval	Subinterval	Wavenumber interval (cm^{-1})		Wavelength interval (nm)	
1	1	57000	44500	175.4	224.7
	2	44500	41000	224.7	243.9
	3	41000	35000	243.9	285.7
	4	35000	33500	285.7	298.5
	5	33500	31007.8	298.5	322.5
	6	31007.8	27972	322.5	357.5
	7	27972	22857.1	357.5	437.5
	8	22857.1	20100.5	437.5	497.5
	9	20100.5	16806.7	497.5	595.0
	10	16806.7	14440.4	595.0	692.5
2		14500	7700	689.7	1298.7
3		7700	5250	1298.7	1904.8
4		5250	4000	1904.8	2500.0
5		4000	2850	2500.0	3508.8
6		2850	2500	3508.8	4000.0

6.2.2. Atmospheric Inputs to the Radiative Transfer Model

The radiative transfer calculations used in this study include the effects of Rayleigh scattering, absorption by atmospheric gases, and absorption and scattering by aerosols. The radiative transfer equation is solved at four layers as listed in Table 6.2. The height of the ground is set to .15 km to match the altitude of the Eugene measurement station. Aerosol properties are defined as homogeneous within these layers. For the aerosol optical depth retrievals described in Section 6.3, aerosols are placed only in the lowest layer, representing tropospheric aerosols, and the third and fourth layers are

combined. When calculations of varying stratospheric aerosol concentrations are considered in Section 6.4, a fourth layer is defined all stratospheric aerosols are assumed to be in the top layer of 15 km to the top of the atmosphere. Net optical depths for atmospheric absorption are calculated for each layer based on atmospheric profiles of pressure, temperature, and absorber densities. Rayleigh scattering properties are defined for each layer depending on the amount of gas in each level. A combined optical depth, single scattering albedo, and scattering phase function is then derived for each layer, and is used to calculate the radiative flux at the boundaries of each layer.

Table 6.2. Model layers

<i>Layer</i>	<i>Aerosol Inputs</i>
.15 km – 2 km	Continental type aerosols
2 km – 15 km	--
15 km – 30 km	Sulphates (in section 6.4)
30 km – TOA	--

Scattering depends only on the relative size of the wavelength and scattering target. Molecular absorption, however, impacts only specific wavelengths. This is further complicated because pressure and Doppler broadening spread the range of wavelengths that are absorbed depending on the atmospheric conditions. In order to calculate the absorption coefficients for atmospheric conditions, a correlated k -distribution is used as described in the work by *Fu and Liou* [1992]. For each wavenumber band and gaseous absorber, atmospheric transmission is converted to a function of absorption coefficients instead of wavenumber. That is, instead of knowing the amount of radiation absorbed at each wavenumber, all that must be known is the fraction of the wavenumbers in a wavenumber band that absorb with a particular absorption coefficient. This correlates an

effective absorption coefficient in a wavenumber band with the temperature, pressure, and density of a particular absorber in the profile.

The main absorbers in the solar spectrum are ozone and water vapor. A summer mid-latitude ozone profile is used throughout the radiative transfer calculations of this study. Water vapor mixing ratio, pressure, and temperature profiles are taken from NCEP Reanalysis data [Kalnay *et al.*, 1996]. The profiles are interpolated to include at least one level for every kilometer of the first 25 km of the atmosphere, and every 5 km thereafter. These profiles are used with the Guo and Coakley [2008] adaptation of the NASA Langley Fu-Liou absorption code to determine an optical depth for each computational layer from gaseous absorbers in each wavenumber band.

In addition to absorption, the scattering by atmospheric molecules must be taken into account. This scattering may be described by the Rayleigh approximation. This approximation is an accurate description of scattering when the wavelength of the incoming radiation is much larger than the size of the scattering particles. The phase function of Rayleigh scattering is proportional to $(1 + \cos^2 \Theta)$, where Θ is the angle between the incoming radiation and the scattered radiation. It is symmetric about the direction of propagation of the radiation, with equal forward and backward scattering. Thus the asymmetry factor is 0. The Rayleigh optical depth has been parameterized by wavenumber interval, and is then determined for each layer by multiplying a wavenumber coefficient by the pressure change per level normalized by the surface pressure.

Aerosol scattering properties are calculated from the aerosol mixes described by *Hess et al.* [1998]. User-provided aerosol optical depths are specified at a reference wavelength of 550 nm. Aerosol properties are then adjusted according to the relative humidity of the profile by parameterizations of single scattering albedo, asymmetry factor, and extinction cross sections at different relative humidities. These aerosols are considered in this model to be tropospheric and in the first 2 km of the atmosphere. When stratospheric volcanic aerosols are used, these are considered to be at a level of 15 km to 30 km. Because particle diameters are on the order of a wavelength or larger, the henye-greenstein phase function is used here to describe the scattering.

6.2.3. Discrete Ordinate Method of Solving the Equation of Radiative Transfer.

In order to calculate the irradiance, Eq. 6.2 must be solved for the radiance of each wavenumber band and model level, and then the radiances are used to derive the irradiance. The equation cannot be solved analytically, so it must be solved numerically. In this study, an 8-stream discrete ordinate (disort) calculation is used to solve the equation [*Stamnes et al.*, 1988]. This method uses Gaussian quadrature to approximate the integral by a system of eight, coupled differential equations that can be solved for an arbitrary stack of homogeneous atmospheric layers. The radiance is broken into direct and diffuse components, such that

$$I(\tau, \mu, \phi) = F_0 e^{-\frac{\tau}{\mu_0}} \delta(\mu - \mu_0) \delta(\phi - \phi_0) + I_{diffuse}(\tau, \mu, \phi), \quad (\text{Eq. 6.3})$$

where F_0 is the solar spectral flux incident at the top of the layer.

Only the surface solar irradiance is of interest in this study. Because only this flux is needed and a plane-parallel model of the atmosphere is assumed, azimuthally-averaged radiances can be used and Eq. 6.2 becomes:

$$\mu \frac{dI(\mu)}{d\tau} = I(\mu) - \frac{\omega}{2} \int_{-1}^1 d\mu' p(\mu', \mu) I(\mu') - \frac{\omega}{4\pi} F_0 e^{-\frac{\tau}{\mu_0}} p(-\mu_0, \mu), \quad (\text{Eq. 6.4})$$

where $I(\mu)$ is the diffuse radiance.

The phase function is expanded in terms of Legendre polynomials. The radiance will also be expanded in terms of Legendre polynomials in the Gaussian quadrature expansion. The advantage of using Legendre polynomials for both expansions is that the sum of all the cross-terms between the product of the expanded phase function and radiance will remain normalized. This normalization ensures that energy is conserved in the approximation. The phase function expansion calculations also use the $\delta - M$ method [described in *Wiscombe, 1977*] of separating off the strong forward scattering peak from the rest of the phase function expansion in order to make the solution accurate with less computational demands. The phase function becomes:

$$\hat{p}_\delta(\mu', \mu) = 2f\delta(\mu' - \mu) + (1 - f) \sum_{l=0}^{2N-1} (2l+1) \hat{\chi}_l P_l(\mu') P_l(\mu), \quad (\text{Eq. 6.5})$$

where $\hat{\chi}_l$ is the moment of the scaled phase function, and f is a scaling factor determined by equating the first two moments of the original and scaled phase function. The asymmetry parameter, single scattering albedo, and optical depth can then be rescaled so that the radiative transfer equation has the same format as the original equation. For the

sake of clarity, Equation 6.6 does not use notation with rescaled $\delta - M$ values, but the mathematics is the same.

Each computational layer is taken to be homogenous. Within each layer and wavenumber band, a cumulative optical depth, single scattering albedo, and phase function expansion coefficient is calculated by combining the molecular absorption, Rayleigh scattering, and aerosol parameters. For Rayleigh scattering, the phase function expansion coefficient is zero for all but the zeroth and second orders of expansion of the phase function because only a $(1 + \cos^2 \Theta)$ term is needed. For Mie scattering with aerosols, the henyeey-greenstein phase function approximation is used, and the coefficient of the k th order expansion of the phase function is the asymmetry parameter to the k th power. These phase functions are combined into a total effective set of expansion coefficients using weighted averages.

The 8-stream discrete ordinate approximation of the radiative transfer equation can then be written as a system of 8 equations for $i=1 \dots 8$:

$$\begin{aligned} \mu_i \frac{dI(\tau, \mu_i)}{d\tau} = & I(\tau, \mu_i) - \frac{\omega}{2} \sum_{j=-N; j \neq 0}^N w_j \sum_{l=0}^{2N-1} (2l+1) g^l P_l(\mu_j) P_l(\mu_i) I(\tau, \mu_j) \\ & - \frac{\omega}{4\pi} F_0 \sum_{l=0}^{2N-1} (-1)^l (2l+1) g^l P_l(-\mu_0) P_l(\mu_i) e^{-\frac{\tau}{\mu_0}} \end{aligned} \quad (\text{Eq. 6.6})$$

where $N = 4$ for an 8-stream calculation and w_j are the quadrature weights for the Gaussian quadrature expansion of the radiance. These equations are then solved for each

atmospheric layer and wavenumber interval, and used to calculate the irradiance at the surface.

6.3. Aerosol Optical Depth Retrievals

6.3.1. Possibility of Retrieving Aerosol Optical Depths with Available Measurements

The radiative transfer calculations were used to retrieve aerosol optical depths from the broadband measurements. Because broadband irradiance is the sum of the irradiance from many wavelengths, the calculated direct normal flux depends on the aerosol size distribution and absorption properties and not just on the optical depth. Since no specific information was available to describe the aerosol size distribution at these sites, a constant continental aerosol size distribution was assumed according to the typical aerosol mixes described by *Hess et al.* [1998]. Three aerosol mixes were used that varied in the amount of absorbing particles present. Figure 6.1 shows radiative transfer calculations of direct (top row) and diffuse (bottom row) irradiance using these three mixes. Each graph shows five different aerosol optical depths at 550 nm. For the same aerosol optical depth, the direct irradiance can vary over 100 W/m^2 between the different models. Thus, without more information on the nature of the aerosols, aerosol optical depths cannot be retrieved from broadband direct irradiance alone.

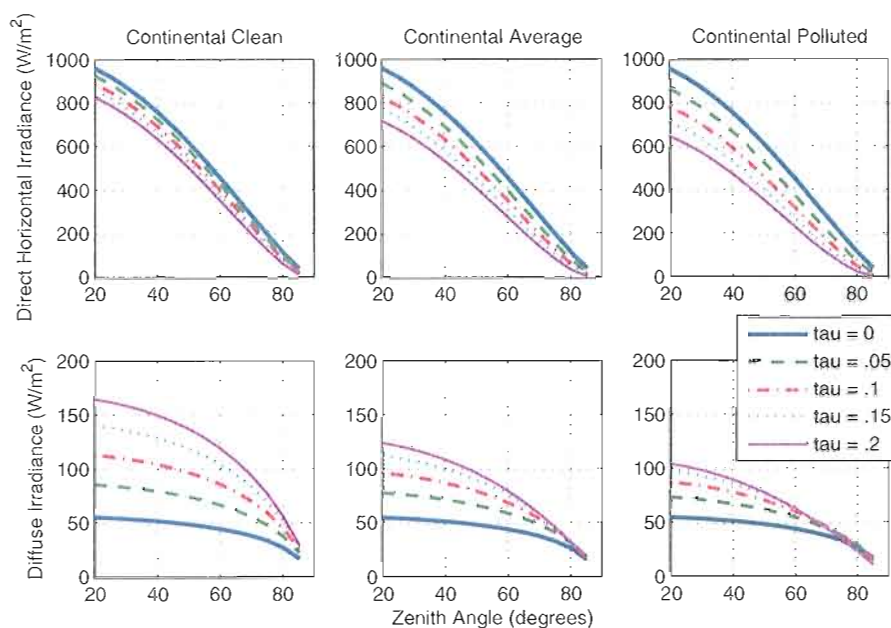


Figure 6.1. Radiative transfer calculations of direct horizontal and diffuse irradiance plotted by zenith angle for three aerosol types. Each line shows calculations for a different AOD at 550 nm. Note how the difference between the direct irradiance for the same AOD with different aerosol types can be over 100 W/m^2 different. This difference requires additional information in order to retrieve aerosol optical depths from these broadband direct measurements.

The other measurement available to help determine the correct aerosol mix is the diffuse irradiance. At Burns and Hermiston, and for many years in Eugene, the only available diffuse measurement is calculated from the difference between the total and direct horizontal irradiance. It was found that the cosine response errors in these calculated diffuse values are too large to be useful in distinguishing between the aerosol mixes. Since 2000, diffuse measurements have been made in Eugene with a black and white type pyranometer. As described in Chapter II, this method of measurement is currently considered the most accurate way to measure broadband diffuse irradiance. Figures 6.2 and 6.3 show daily measurements for clear periods of direct and diffuse

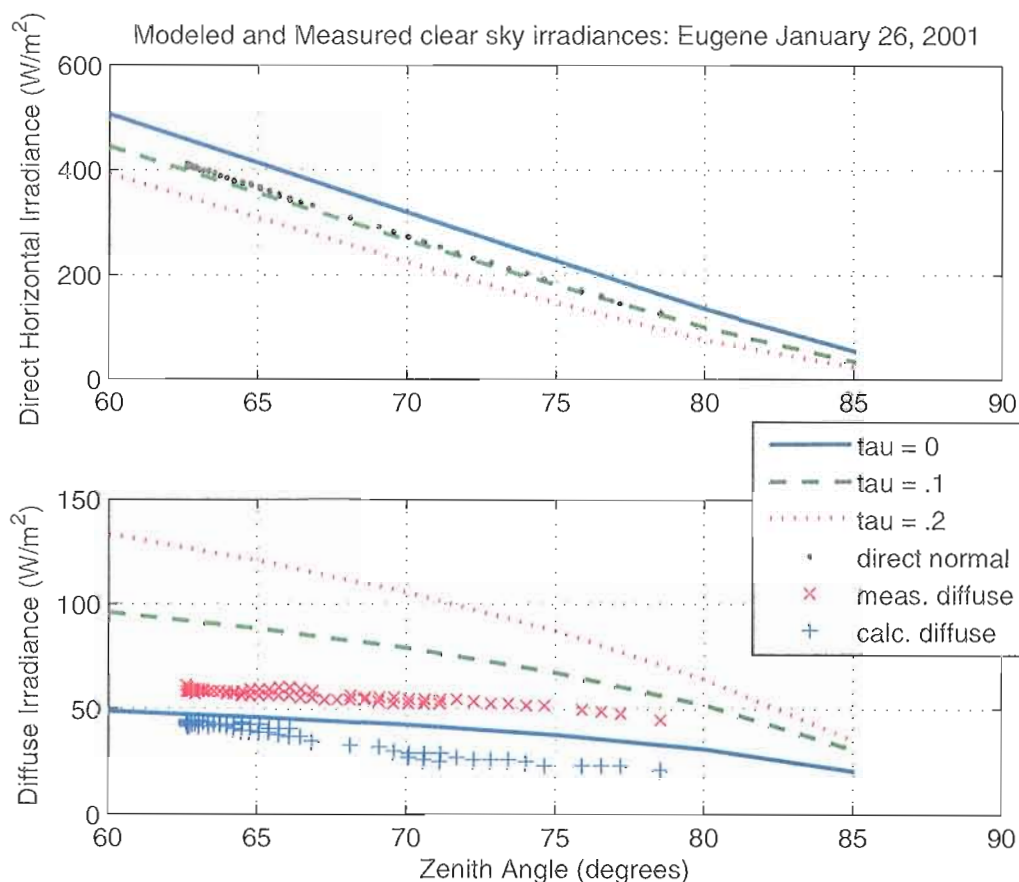


Figure 6.2. Modeled and measured direct horizontal and diffuse irradiance for January 26, 2001 in Eugene. The radiative transfer calculations use a continental clean aerosol type. The calculated diffuse (+’s) is too low at these zenith angles to be useful in distinguishing between aerosol models, as it is even below calculations without any aerosol content.

irradiance for a day in winter and summer respectively. Radiative transfer calculations of the direct horizontal and diffuse irradiance for a Continental Clean type aerosol mix at different aerosol optical depths are also plotted. The diffuse irradiance is plotted in the bottom graph of each figure. The +’s show the calculated diffuse and the x’s mark the measured diffuse for that day. It is easy to see how the errors in the calculated diffuse make it difficult to distinguish the correct aerosol optical depth. At the high solar zenith

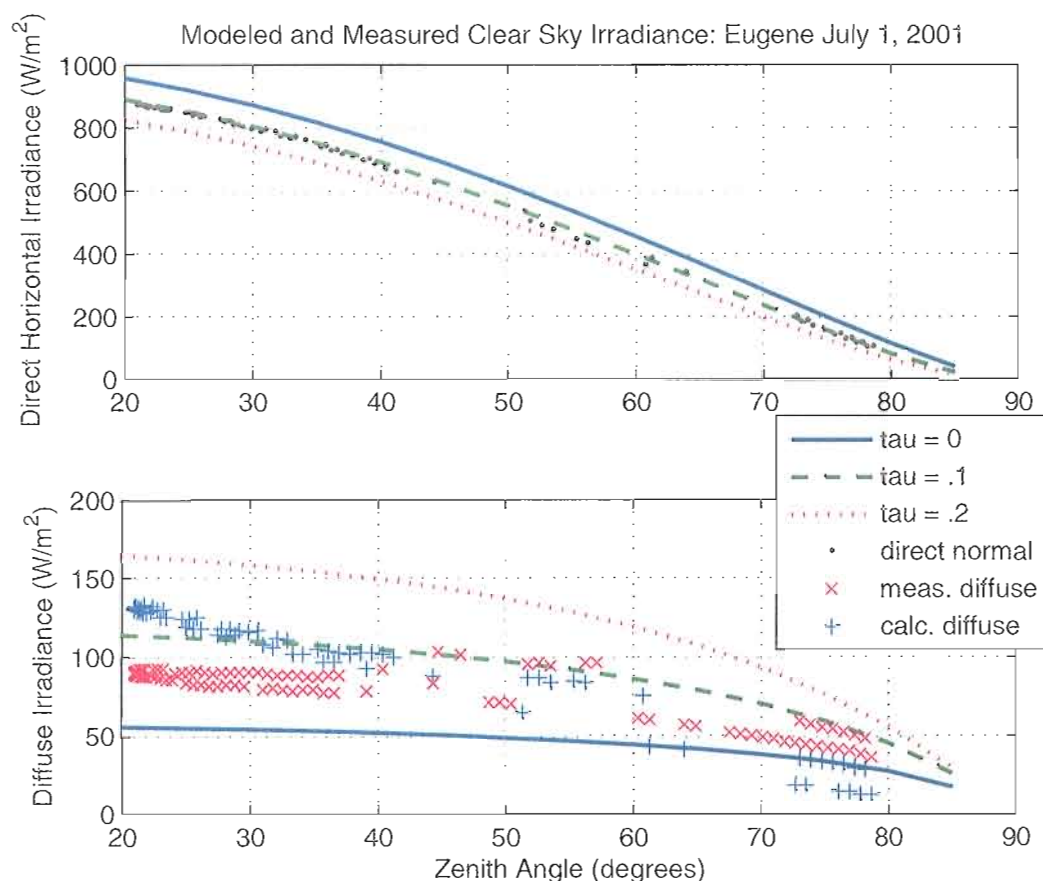


Figure 6.3. Modeled and measured irradiance for clear skies on July 1, 2001 in Eugene as described in Figure 6.2. The zenith angle dependent systematic error of the calculated diffuse irradiance (+'s) can be clearly seen. Because this error depends on both instrument and sky conditions, it cannot be corrected with the data available at the UO SRML stations. The measured diffuse irradiance, on the other hand, will improve the ability to distinguish the correct aerosol type and AOD.

angles in winter, the calculated diffuse is below modeled values that do not include any scattering by aerosols (see Figure 6.2). The larger zenith angle range in the summer shows how the shape of the curve of the calculated diffuse differs from the measured diffuse (Figure 6.3). At high solar zenith angles, the calculated diffuse is lower than the measured diffuse, but at low zenith angles the calculated diffuse is higher than the measured diffuse. The calculated diffuse matches the measured diffuse around a zenith

angle of 45 degrees, the zenith angle where the total irradiance instrument is calibrated. This systematic error in the zenith angle response comes primarily from the cosine response error in the total irradiance measurement. As it depends on both the instrument and the atmospheric conditions, it cannot be corrected for with the measurements available at the SRML monitoring stations. Thus, the calculated diffuse will not have sufficient accuracy to distinguish between aerosol mixes. The measured diffuse irradiance in Eugene from recent years, however, can be used to retrieve aerosol optical depths and better understand the characteristics of the background aerosol at this site.

6.3.2. Daily Retrievals

Only the days with enough clear measurements to be fitted by the *Long and Ackerman* [2000] algorithm were used to retrieve aerosol optical depths. This requires at least 22 5-minute periods to be identified clear from a wide range of zenith angles during the day. Using only these days should screen out less clear periods, and also give clear periods at a wide range of zenith angles to better see the temporal stability of aerosol optical depth. These clear days were determined from the year 2001. The direct horizontal irradiance rather than the direct normal irradiance was used for AOD retrievals. The direct horizontal irradiance is calculated by multiplying the direct normal irradiance by the cosine of the solar zenith angle.

Daily lookup tables were created using the radiative transfer model for broadband irradiance using NCEP Reanalysis water vapor and temperature profiles at 10:00 PST.

The highest resolution available for the NCEP meteorological fields is at 6-hour intervals. The irradiances at 16:00 PST were also calculated, but because the water vapor changes little over the course of a day and the difference in water vapor between 10:00 and 16:00 is much smaller than the difference between aerosol models, only the values at 10 are shown here for convenience. The irradiance was calculated for zenith angles at every 5 degrees between 20 and 85 degrees. Aerosol optical depths were calculated at intervals of .05 for each of five different aerosol mixes.

The AOD retrievals were done by first linearly interpolating modeled irradiance values at the zenith angle of interest from the lookup table. The correct AOD was then chosen using a linear interpolation of the log of the irradiance. This was done for each of the three aerosol mixes: continental clean, continental average, and continental polluted aerosol types. These three differ by including progressively greater amounts of soot in the mixes to describe the impact of anthropogenic emissions. Figure 6.4 shows AOD retrievals for the three mixes on July 1, 2001 in Eugene. The AOD from direct and diffuse irradiance does not match in any of the three calculations. For the continental clean aerosol type, the AOD retrieved from the diffuse irradiance is lower than that retrieved from direct irradiance. Oppositely, the AOD retrieved from the diffuse irradiance is higher than that from direct in the other two aerosol types. Direct and diffuse retrievals seem to match the best on this day with the continental average aerosol type. Figure 6.5 shows AOD retrievals from a day in October, and on this day, the AOD retrievals from direct and diffuse irradiance agree with the observations for the continental average aerosol mix.

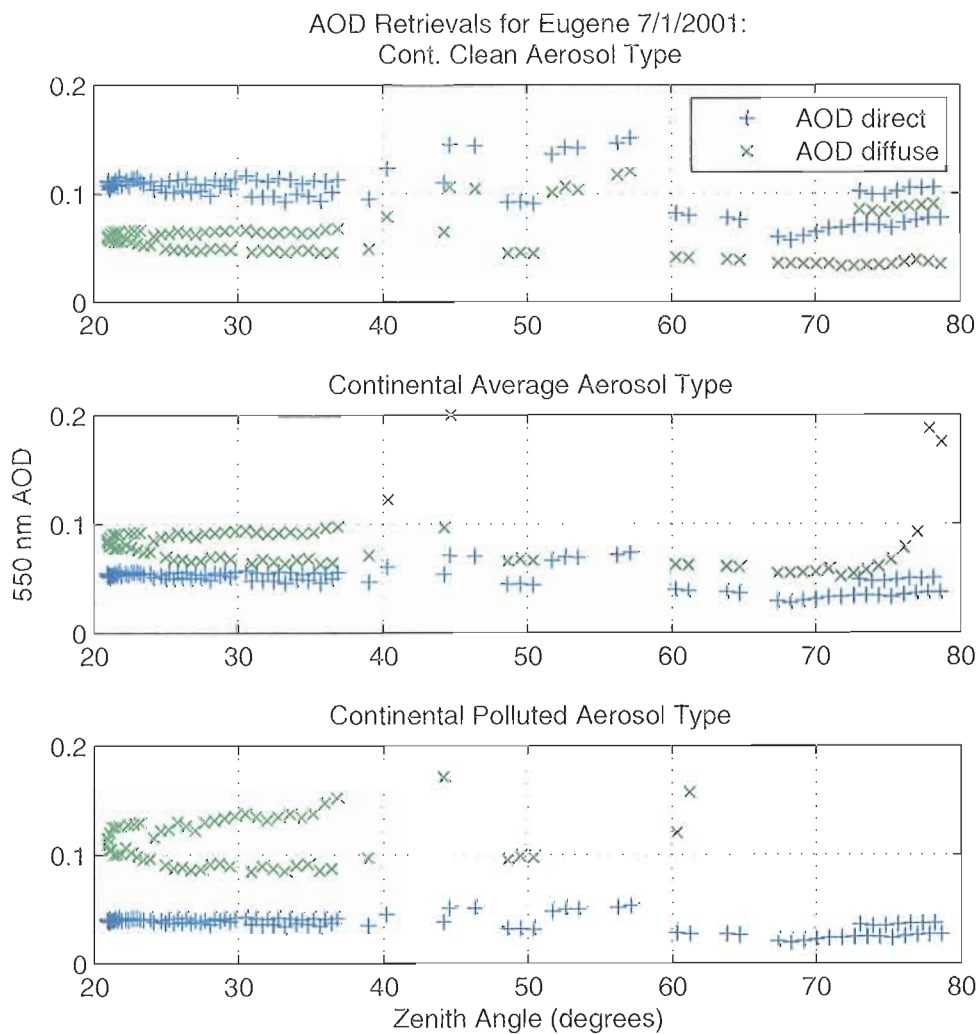


Figure 6.4. Aerosol optical depth (550 nm) retrievals for 3 aerosol types in Eugene. AOD is retrieved from both direct horizontal and diffuse measurements. As the aerosol type changes from a continental clean to polluted aerosol mix the AOD changes from being larger in the direct retrieval to the diffuse. For this day, the continental average aerosol mix gives the most consistent results for direct and diffuse irradiance retrievals.

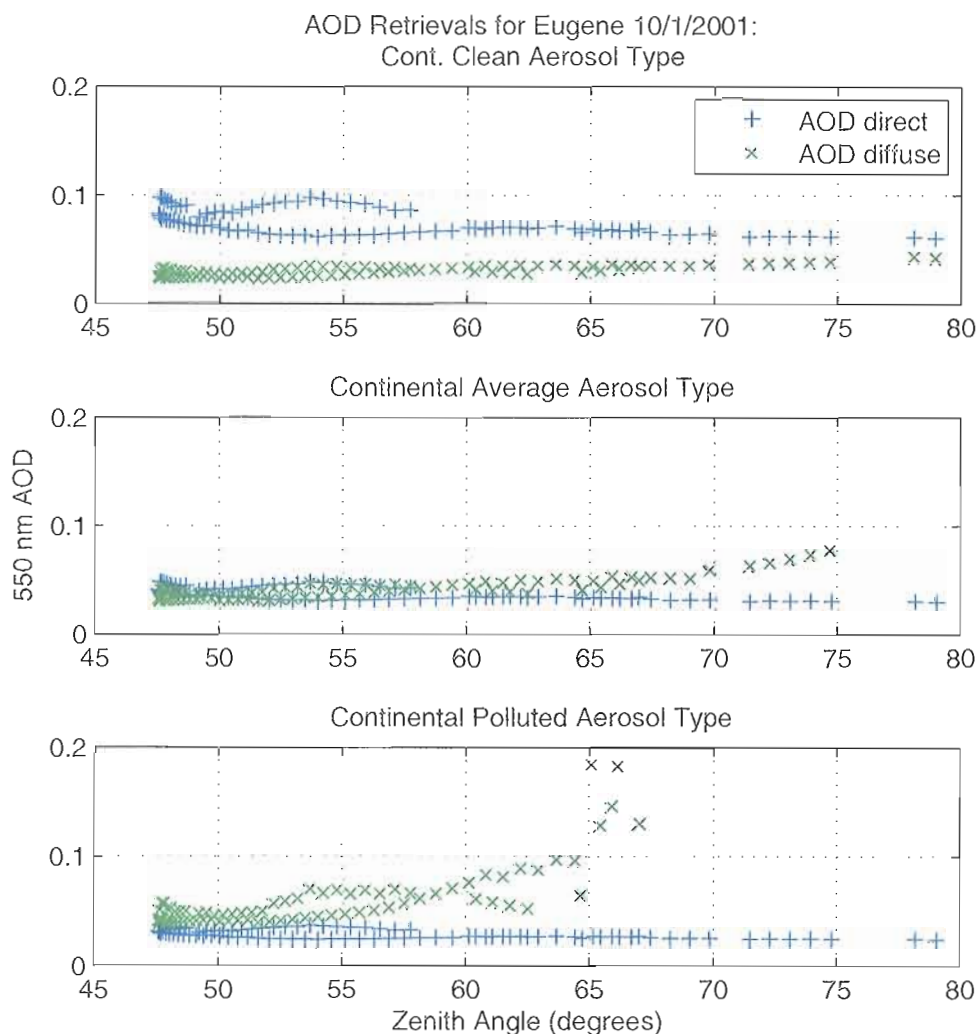


Figure 6.5. AOD retrievals as described in Figure 6.4, but for October 1, 2001. Note how on this day the retrievals from direct and diffuse irradiance fit very well for the continental average aerosol type.

Figure 6.6 shows daily average retrieved AOD in Eugene in 2001 for both diffuse and direct irradiance. The top graph shows the retrievals assuming a continental clean aerosol mix and the bottom graph shows a continental average aerosol mix. These two mixes were chosen because they give AOD retrievals that are the closest for direct and diffuse irradiances. Over the course of the year the continental clean aerosol type gives

diffuse AODs consistently lower than direct AOD retrievals. The opposite is true for the continental average mix, though in the latter half of the year, the AOD retrieved from direct and diffuse irradiance matches well on some days.

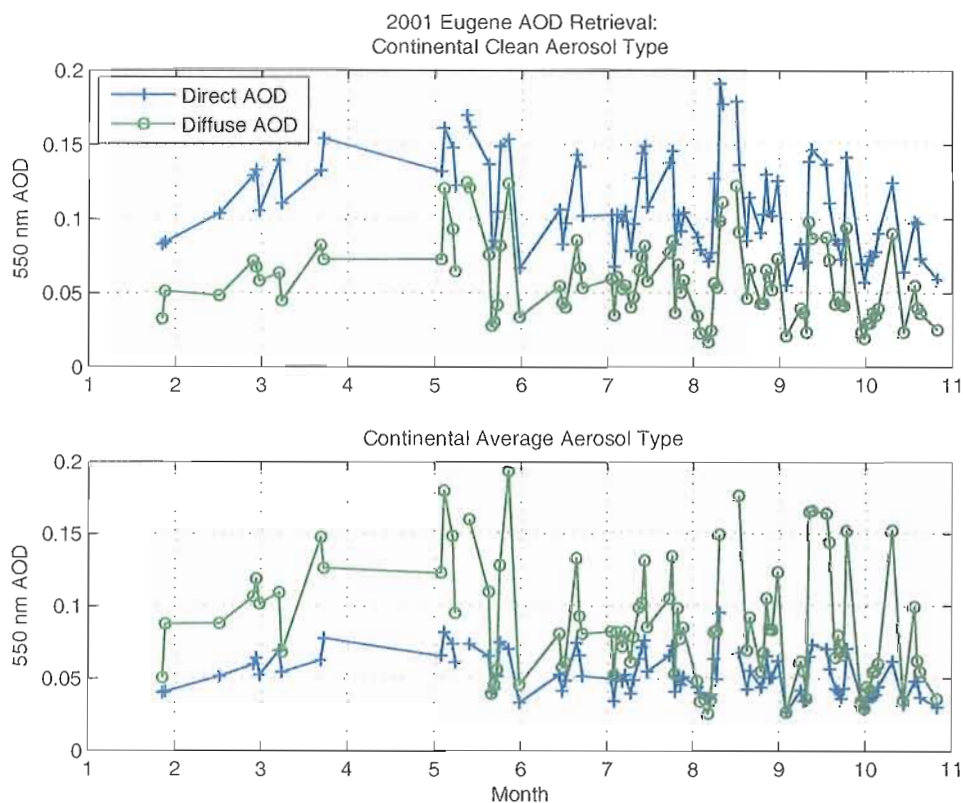


Figure. 6.6. Daily average AOD retrieved from direct (+'s) and diffuse irradiance (o's). The top graph shows AOD for a continental clean aerosol type and the bottom graph for a continental average aerosol type.

Figure 6.7 shows another comparison between the retrieved direct and diffuse aerosol optical depths for different models. None of the aerosol mixes fit the absorption on average. An aerosol mix with the correct amount of absorption should give a correlation with a slope of 1 that goes through the origin. The slope of lines fit to each

data set in Figure 6.7 indicates that the best aerosol mix contains a level of soot between that of the continental clean and average aerosol mixes defined by *Hess et al.* [1998]. The intercepts of lines fit to the correlation data sets indicates, however, that AOD retrieved from direct irradiance is consistently higher than AOD retrieved from diffuse irradiance. The cause of this bias is unknown, but a likely possibility is errors in the measurements.

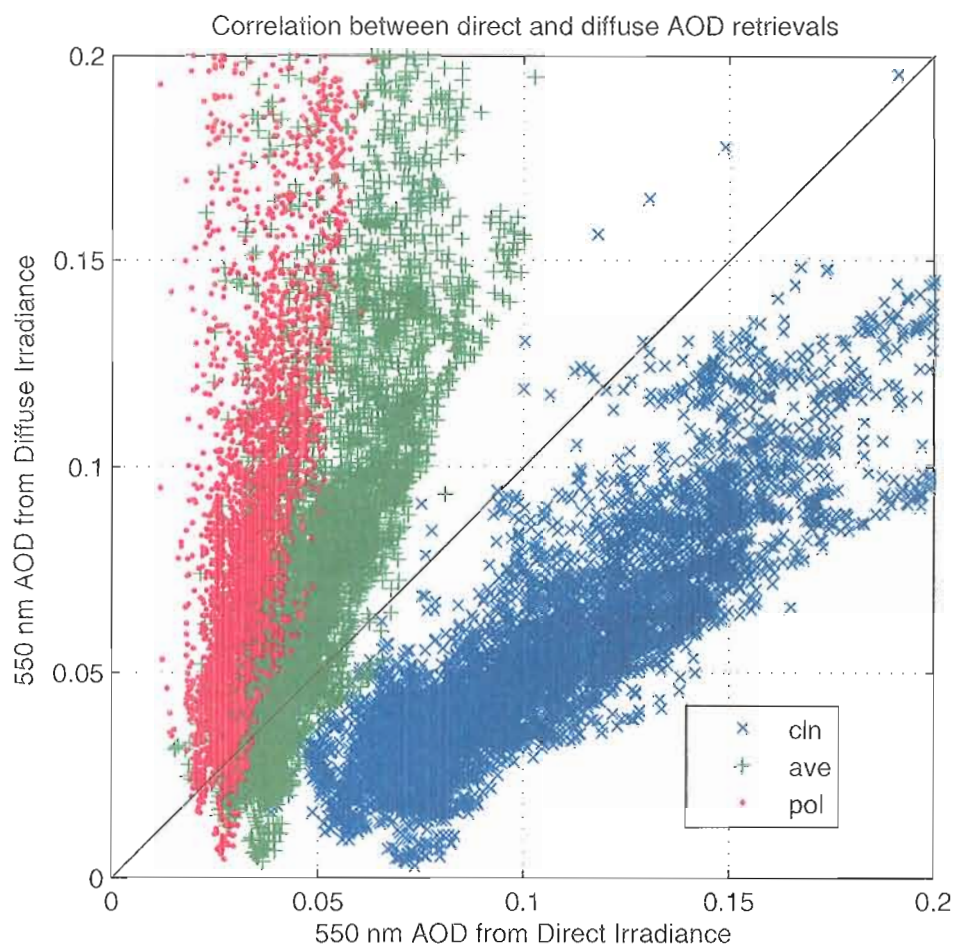


Figure. 6.7. Correlations between AOD retrieved from direct and diffuse irradiance. Data are from 5-minute values for Eugene in 2001. Note the three aerosol types here show consistently different behavior, though none is always the preferred type.

A new aerosol mix was calculated using a mix of one-third of the continental average and two-thirds of the continental clean aerosol types. Twelve percent of the particles in this mix are soot particles. The correlation for diffuse and direct AOD retrieved from 2001 Eugene data is plotted in Figure 6.8. The slope of the correlation data is now about 1, but the intercept is -0.026 . That is, AOD retrieved from direct irradiance is consistently about $.026$ higher than that retrieved from diffuse irradiance.

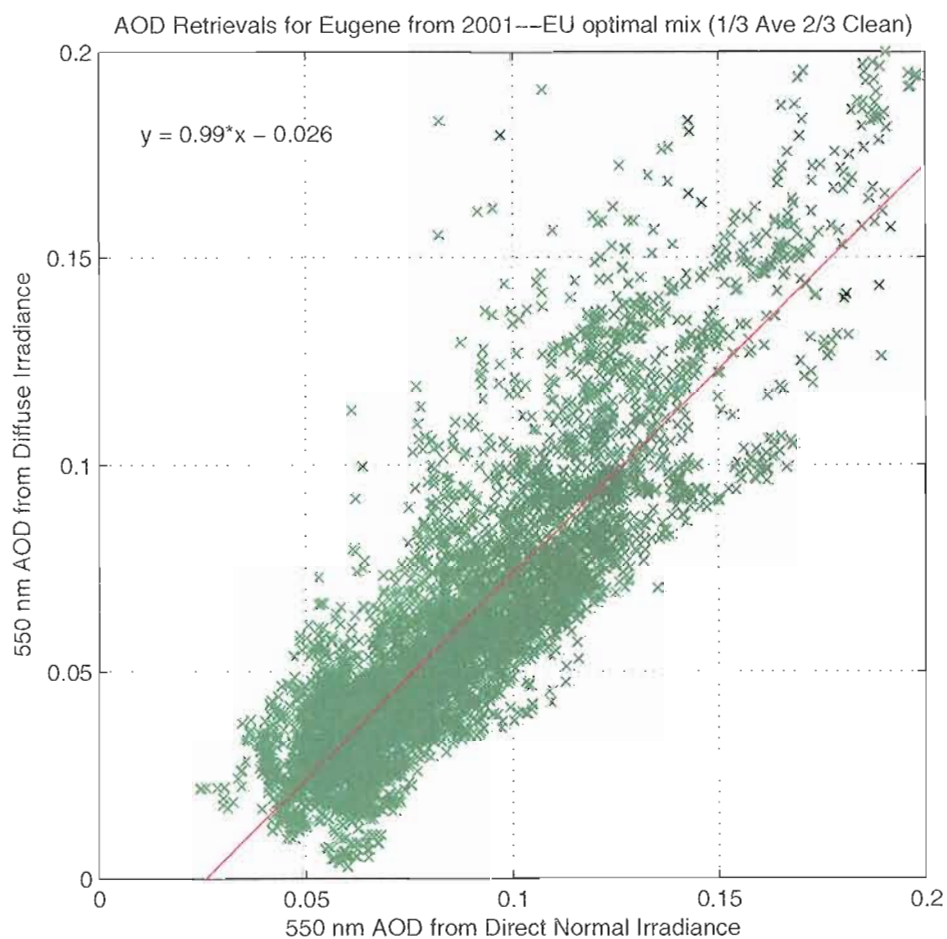


Figure. 6.8. Correlations between AOD retrieved from direct and diffuse irradiance for an aerosol mixture of 1/3 continental average and 2/3 continental clean.

The bias between AOD retrieved from direct and diffuse irradiance cannot be fixed by changing the absorption of the aerosols. Increasing the direct irradiance measurements by 3% before using them to retrieve aerosol optical depth reduces the bias from .026 to .009. Likewise, increasing the diffuse measurements before using them to retrieve aerosol optical depth reduces the bias. Given the lack of an absolute reference for diffuse irradiance (as discussed in Chapter II), a 3-4% calibration bias between diffuse and direct normal irradiance measurements is possible. Further study would be needed to identify the cause of this bias.

6.4. Setting Limits on the Possible Amount of Change in Tropospheric Aerosols

Another way to determine what change in tropospheric aerosols has occurred in Oregon is to eliminate the contribution of several possible factors to the clear-sky direct normal trends found in Chapter V. The trends in direct normal irradiance from zenith angles of 65-75° found in Chapter V were .80, .88, and .11 W/m² per year for Burns, Eugene, and Hermiston respectively from 1987-2007. The atmospheric changes considered in this study are volcanic aerosol clearing, changes in water vapor, and tropospheric aerosol changes. To get a more realistic idea of what part of the positive trend in clear-sky irradiance comes from anthropogenic aerosols, monthly average direct normal irradiance is calculated using inputs of water vapor and stratospheric aerosols.

Figure 6.9 plots monthly average stratospheric aerosol optical depths for a zonal mean at 43° N latitude. The data comes from the global stratospheric aerosol data set described by *Sato et al.* [1993]. For this time period, the data set is based on satellite measurements of stratospheric aerosol optical depth from the SAM II and SAGE satellite instruments. The wavelength dependence and asymmetry parameter for the calculations were taken from the sulphate aerosol type in the *Hess et al.* [1998] aerosol model assuming a constant stratospheric relative humidity of 5%. Thus, no change in the aerosol size distribution was considered in the calculations, only in the concentration. The aerosols were assumed to be completely scattering with no absorption. After the year 2000, the AOD was kept constant at the 2000 level of 0.0005. In addition to the

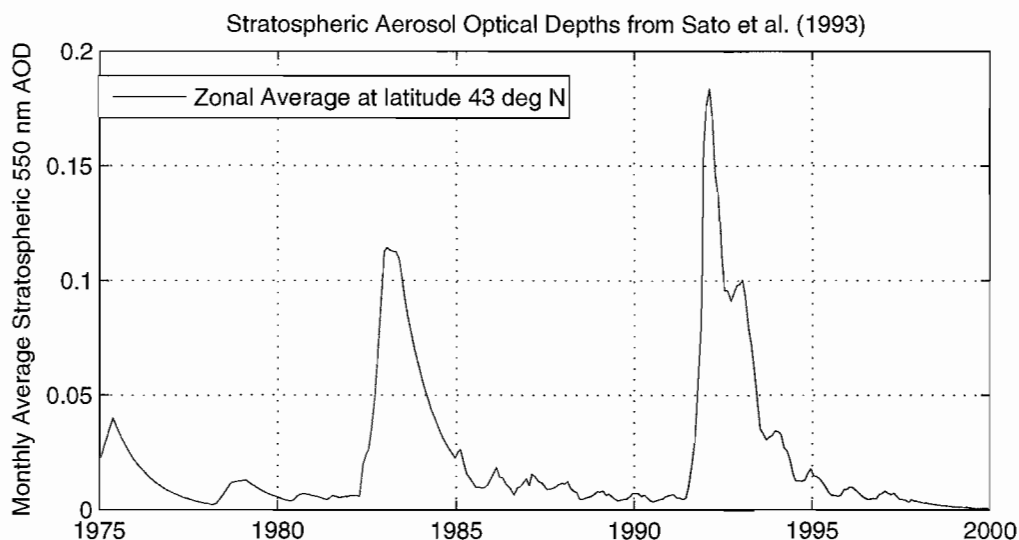


Figure 6.9. Zonal average monthly stratospheric aerosol optical depth at 43° N latitude from Sato et al (1993). These stratospheric AODs are based on SAGE and SAM measurements. These AOD values will be used to calculate how much of the trend in clear-sky data from 1987 to the present can be explained by a clearing of stratospheric aerosols after Mt. Pinatubo.

stratospheric aerosols, a continental average tropospheric aerosol mix was used with a constant AOD of 0.05. The AOD values were used along with monthly average NCEP Reanalysis water vapor and temperature profiles in the radiative transfer model to calculate clear-sky monthly average direct normal irradiance at zenith angles of 65-75°.

The results of the model calculations are plotted in Figure 6.10 along with monthly average clear-sky direct normal measurements. The annual cycle is much stronger in the measurements than the modeled values. This is expected, as there is also a seasonality to tropospheric aerosol loads that is not included in the model inputs. Neglecting this difference, the modeled values are in a reasonable range and they fit the variation in the volcanic aerosols well. The top graph in Figure 6.11 shows the monthly average anomalies for both the modeled and measured data sets at Eugene. The measured and modeled monthly average irradiance anomalies agree following the volcanic eruptions. The bottom graph in Figure 6.11 plots the difference between the measured monthly average anomalies and the modeled anomalies. No detectable impact from the volcanic eruptions remains in the difference plot. The stratospheric AODs used in the modeled data do not explain the low values in 1980 and 1981 seen in the measurements, however.

Of particular interest is how much of the increase in clear-sky direct normal irradiance between 1987 and 2007 (excluding June 1991 to December 1994) is caused by anthropogenic aerosols. Figure 6.12 plots measurements and modeled monthly anomalies for this time period. Each graph in Figure 6.12 plots monthly average anomalies of clear-sky direct normal irradiance for zenith angles of 65-75 degrees. Two modeled data sets

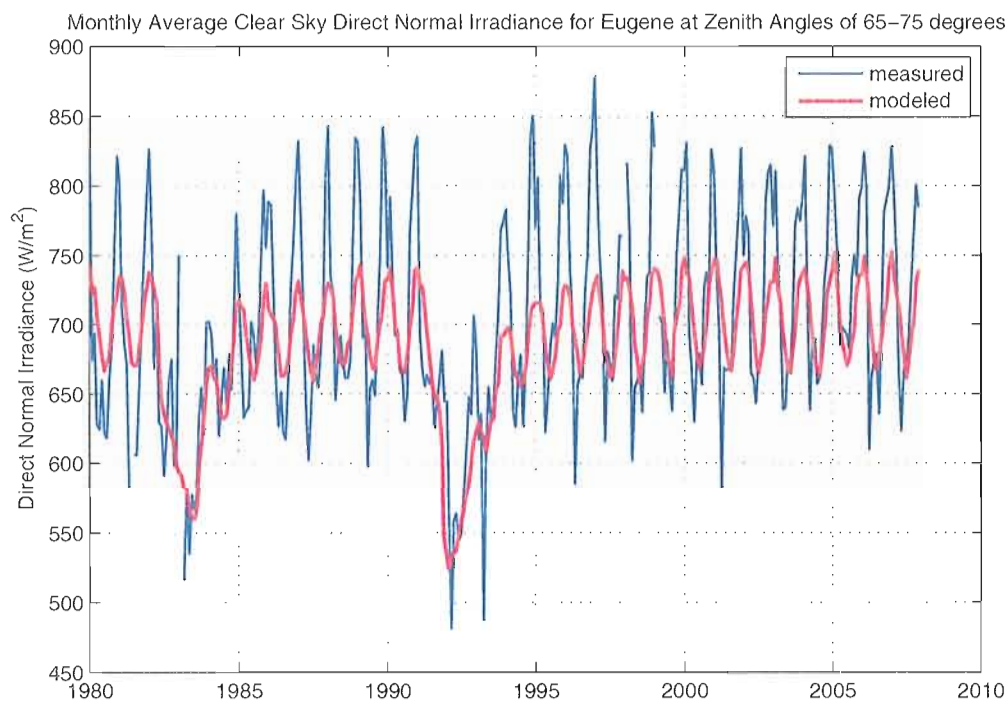


Figure 6.10. Eugene monthly average clear-sky direct normal irradiance at 65-75 degrees. The thin blue line shows measurements, while the thick red line shows modeled values. The modeled values use monthly average temperature and humidity profiles from NCEP reanalysis data, which captures some of the seasonal cycle. A constant tropospheric AOD is used of 0.05 for a continental average aerosol type in the model calculations, explaining the smaller seasonal variation. Model calculations use monthly average the stratospheric AOD plotted in Figure 6.9, which matches the volcanic signal in the measured values quite well.

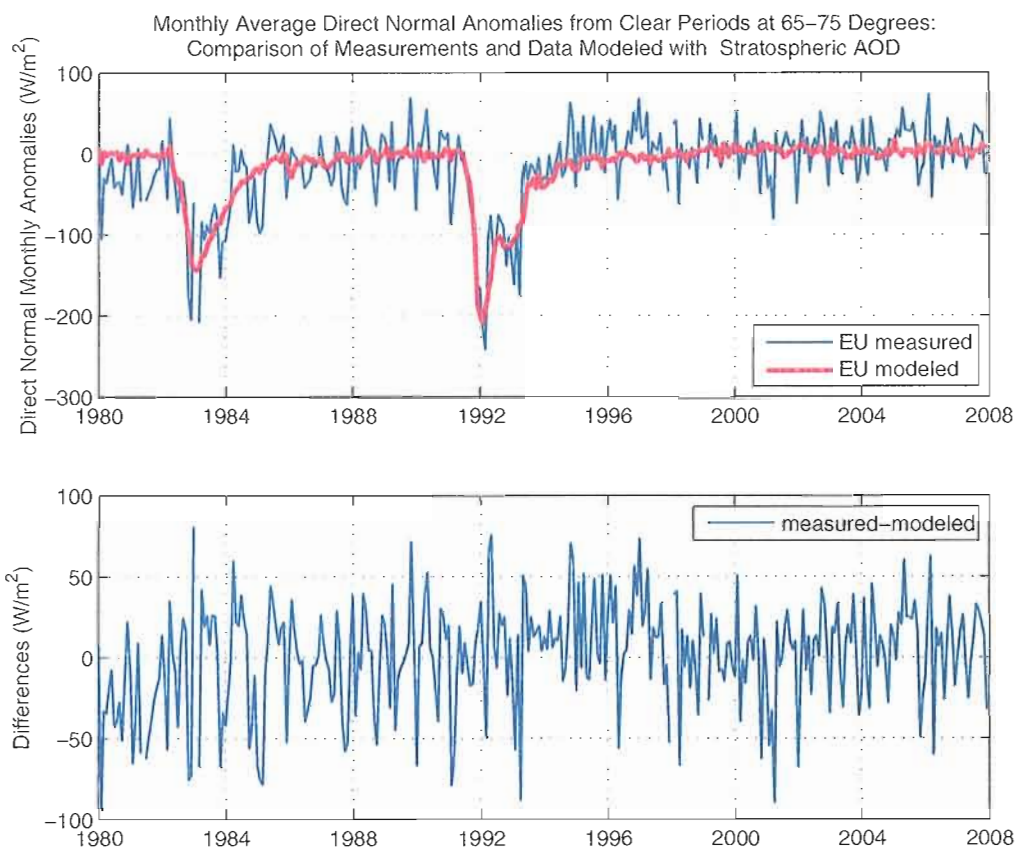


Figure 6.11. Monthly average anomalies of modeled and measured irradiance. The top plot shows the anomalies from average monthly values of the data plotted in Figure 6.10. (The average monthly values are calculated without including volcanic years of March 1982-December 1985 and June 1991-December 1994.) The bottom plot shows the difference between the measured values and modeled ones. The modeled data closely characterizes the impact of the volcanic aerosols.

are plotted. The radiative transfer calculations in Figure 6.12B use both the stratospheric and water vapor input data sets. The model calculations in Figure 6.12D, however, only include monthly climatologies of water vapor and are thus without inter-annual water vapor variability. The difference between the trends shown in plot B and plot D, -0.15 W/m^2 per year, is used as an estimate of the impact of water vapor changes over the 20

years. The trend in plot D is $.65 \pm .18 \text{ W/m}^2$ per year, representing the irradiance impact of just the volcanic aerosol changes. Changes in water vapor and stratospheric aerosols over this time period impact the direction of the trend oppositely. The combined impact of stratospheric aerosols and water vapor is $.49 \pm .09 \text{ W/m}^2$ per year. (The uncertainties represent one standard error of the slope coefficient including a correction for autocorrelation of order one. Trends are considered significant when greater than twice the standard error of the slope.) It should be noted that the NCEP reanalysis water vapor profiles are a class B product, meaning they are influenced strongly by the climate model and not just observations and thus may not give reliable values for trend studies [Kalnay *et al.*, 1996]. Though the magnitude of the impact of the water vapor change is not known well, the direction is consistent with an increase in temperature over the time period.

All of the statistically significant portion of the increase in clear-sky measurements, $0.88 \pm 0.34 \text{ W/m}^2$ per year in the measurements, can be explained by the combined impact of the clearing of stratospheric aerosols and water vapor variability. The remaining trend in the differences, plotted in Figure 6.12C, is used as an estimate of the impact of anthropogenic aerosols. The trend of $.38 \pm .36 \text{ W/m}^2$ per year is on the order of the standard error of the trend line fit and thus is not statistically significant, though does estimate a limit on the possible change in anthropogenic aerosols.

Assuming the average AOD retrieved from direct irradiance measurements in 2001 describes the current background aerosol properties, an estimate can be calculated of what change in tropospheric AOD is consistent with the clear-sky direct normal irradiance increase from 1987-2007. The calculation of the AOD change is found

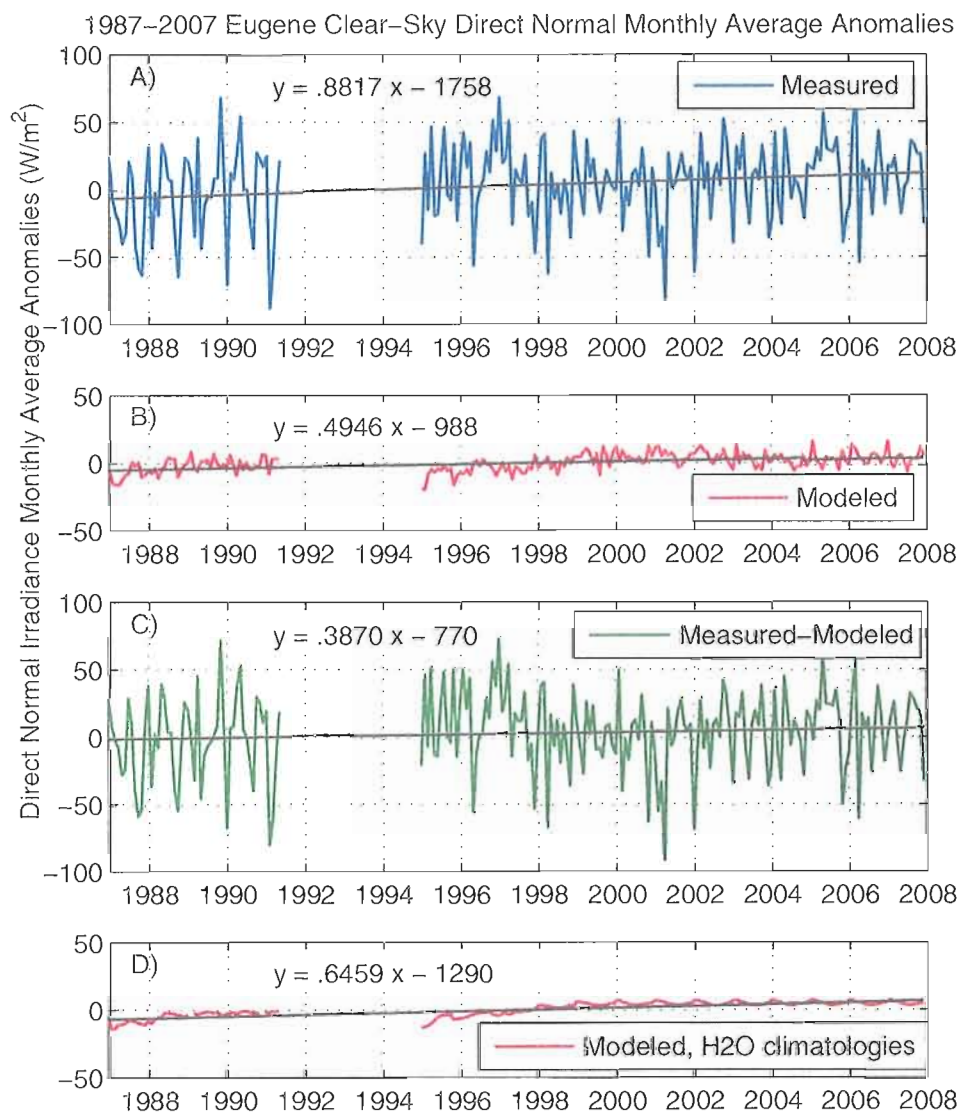


Figure 6.12. Trends in clear-sky Eugene direct normal irradiance from 1987-2007, for four time series: A) Measurements; B) Modeled from both stratospheric aerosols and water vapor changes; C) Difference between A and B; D) Modeled data including only changes in stratospheric aerosols.

assuming all other atmospheric parameters stay constant except for the tropospheric AOD. The average 550 nm AOD for Eugene in 2001 is 0.086. A 20-year increase in direct normal irradiance of 7.74 W/m^2 at $65\text{--}75^\circ$ corresponds to a change in AOD of -0.005 ± 0.005 or $-6\% \pm 6\%$. (The uncertainties represent one standard error of the trend.)

Considering only the uncertainty in the trend calculation, the 95% confidence level range of possible AOD change is -0.014 to 0.004. That large range shows how difficult it is to detect aerosol changes even with direct normal irradiance, at least in a clean environment like that in Oregon. The global average aerosol optical depth decrease estimated by *Streets et al.* [2006], was -0.003 for the 13 years between 1988 and 2000. While the amount of this change is within the possible range of tropospheric aerosol change seen in the data, a change of that magnitude is not detectable given the noise of the time series.

6.5. Annual Average Calculations

Stratospheric aerosol changes clearly impact the high-zenith angle direct normal irradiance, but the impact on annual average irradiance may be much less. In order to estimate that impact, daily average irradiance was calculated for the 16th of each month from January 1980 to December 2007. Irradiance was calculated at 5-minute intervals using the modeled monthly average irradiance described in Section 6.4. Daily averages were calculated from the 5-minute modeled irradiance. The annual mean of these daily averages was used as an estimate of the clear-sky annual average irradiance. This was done for both direct normal and total irradiance.

The results for these model calculations are plotted in Figure 6.13 along with annual average measurements. The measurements are for all-sky annual averages and include cloudy as well as clear periods. The modeled annual averages are calculated for

clear skies and, as expected, are consistently higher than the measurements, which are impacted by clouds. In order to better compare changes in the modeled and measured data, the long-term mean was subtracted from each time series. Figure 6.13 plots these anomalies for direct normal (upper plot) and total irradiance (lower plot).

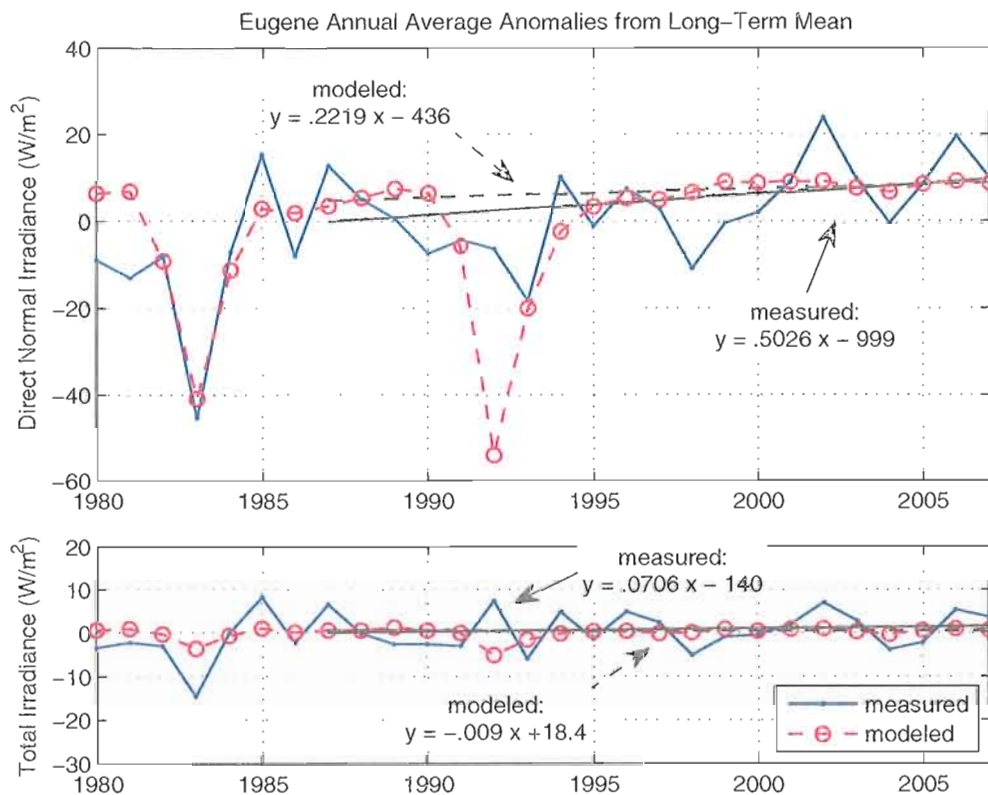


Figure 6.13. Measured all-sky annual average irradiance (solid line) and modeled clear-sky annual averages (dashed line) for both direct normal (upper graph) and total irradiance (lower graph). The average irradiance is subtracted from each time series in order to allow better comparison. Trend lines and their equations are plotted for measured (solid line) and modeled data (dashed line) for the years 1987 to 2007 (excluding 1991-1994).

Linear trend lines from 1987 to 2007 (excluding 1991-1994) show stronger increases in the measured data (solid line) than the modeled data (dashed line). The measured data also has greater variability, however, and the trends in the measured data are not statistically significant for this period. The magnitude and 95% confidence level uncertainties of these trends are given in Table 6.3.

The modeled clear-sky annual average direct normal irradiance increases by $.22 \text{ W/m}^2$ per year between 1987 and 2007, a bit less than half the magnitude of the trend at 65-75 degrees ($.49 \text{ W/m}^2$ per year). When model calculations only include the impact of volcanic aerosols and not water vapor, the trend increases to $.27 \text{ W/m}^2$ per year. This indicates that the changes in stratospheric aerosols impact the direct normal irradiance about 5 times more than the changes in water vapor do. Both modeled trends are statistically significant for this 20-year period. Therefore, the volcanic aerosols are a cause of the trend in annual average direct normal irradiance even after removing the years most visibly affected by those eruptions.

The modeled clear-sky total irradiance, however, actually decreases slightly, though insignificantly, ($-.01 \text{ W/m}^2$ per year) between 1987 and 2007, when the years most impacted by the eruption of Mt. Pinatubo are removed. If the annual average total irradiance is calculated without including the inter-annual variability in water vapor, however, the trend ($.02 \text{ W/m}^2$ per year) becomes positive and significant. This indicates that the change in NCEP water vapor profiles impact the total irradiance as strongly as the clearing of volcanic aerosols. The sensitivity of the model results for total irradiance to the changes in water vapor also indicate that more accurate information will be needed

on the amount of atmospheric absorbers present in order to extract information about changes in aerosols from total irradiance.

Linear trends are also calculated for Eugene measured and modeled annual averages for the period from 1980-2007 (Table 6.3). The results are given for both total and direct normal irradiance for the full time series (all years) and the time series after excluding 1982-1985 and 1991-1994 (no vol). The total irradiance measurements do not show statistically significant trends for these years, unlike the trends calculated from 1976-2007 in Chapter IV. The only statistically significant trend in total irradiance is for the modeled data that only includes stratospheric aerosol changes, giving a trend of $.016 \text{ W/m}^2$ per year. The stratospheric aerosol trend is an order of magnitude less than the trend in measured irradiance, suggesting that the trend seen in all-sky annual average total irradiance comes primarily from cloud variability.

The trends in measured annual average direct normal irradiance from 1980-2007 are statistically significant both including and excluding the volcanic years. The trends in the modeled direct normal irradiance are not significant for this period, however. Removing the volcanic years from the modeled time series reduces the magnitude of the trend by over 70% for the full time period but only reduces the magnitude of the trend in measured data by about 20%. This difference is likely due to the low values in 1980-1981 in the measurements that are not matched in the modeled data.

Table 6.3. Eugene annual average irradiance trends for measured and modeled data (in W/m^2 per year, uncertainties are 2 standard errors)

	Total		Direct Normal	
	<i>All years</i>	<i>No Vol</i>	<i>All years</i>	<i>No Vol</i>
1980-2007				
Measurements	.18 ± .26	.14 ± .22	.90 ± .55	.73 ± .53
Model: Strat. changes	.06 ± .09	.02 ± .01	.71 ± 1.02	.20 ± .31
Model: Strat. and H ₂ O	.03 ± .09	-.01 ± .03	.68 ± 1.04	.16 ± .24
1987-2007				
Measurements	.07 ± .38	.07 ± .35	.69 ± .79	.50 ± .86
Model: Strat. changes	.07 ± .13	.02 ± .02	.90 ± 1.58	.27 ± .24
Model: Strat. and H ₂ O	.04 ± .13	-.01 ± .04	.87 ± 1.60	.22 ± .22

6.6. Summary of Results

Aerosol optical depth could not be retrieved over the full time period because the calculated diffuse observations lacked the accuracy needed to determine an appropriate level of absorption. Measured diffuse is much more accurate and is available for recent years in Eugene. Using 2001 diffuse and direct measurements, the continental aerosol type from *Hess et al.* [1998] was adjusted to give an approximate aerosol mix for Eugene of 1/3 continental average and 2/3 continental clean types. A bias between AOD retrieved from diffuse and direct irradiance is still not understood. The average AOD retrieved from direct irradiance in 2001 is .086, but the average AOD derived from diffuse irradiance is .059. Despite this disagreement, the retrievals still clearly show a very clean average background aerosol in Eugene, with low aerosol optical depths and a low level of absorption.

Radiative transfer calculations of monthly average clear-sky direct normal irradiance at high zenith angles indicate that a clearing of stratospheric aerosols is the greatest factor responsible for the increase in irradiance between 1987 and 2007. Water vapor concentrations increase over the time period according to NCEP reanalysis data, causing a decrease in modeled irradiance. The accuracy of this change is not well known, however, because the reanalysis data is a combination of observations and modeling. The magnitude of the remaining trend in clear-sky direct normal irradiance corresponds to a decrease in tropospheric AOD of -0.005 ± 0.005 or $-6\% \pm 6\%$ over 20 years. However, this remaining trend is not statistically significant, and so no change in tropospheric aerosols can be concluded from the measurements.

Estimates of annual average clear-sky direct normal and total irradiance are also calculated using the monthly average stratospheric AOD and NCEP water vapor profiles. The modeled annual average direct normal irradiance increases by $.22 \text{ W/m}^2$ per year between 1987 and 2007. The impacts on the total irradiance of changes in stratospheric aerosols and water vapor are about equal in magnitude over the same time period but opposite in direction. Forward scattering by aerosols has a smaller impact on total irradiance than direct normal irradiance because much of the scattered radiation reaches the surface as diffuse light. Thus, more information is needed on the accuracy of the water vapor profiles to model the change in total irradiance knowledgeably. The stratospheric aerosol loads and water vapor profiles used to model annual averages do not explain the low values in measured direct normal and total irradiance before 1982.

CHAPTER VII

CONCLUSIONS

The work discussed in this dissertation sought to answer two scientific questions. The first question was, “What caused the increases in all-sky surface solar irradiance at three sites in Oregon?” This study considered instrument calibration, stratospheric aerosol emissions from volcanic eruptions, water vapor, anthropogenic aerosols, and changes in clouds as possible causes of the trends. High aerosol concentrations following volcanic eruptions and low background irradiance before the eruption of El Chichón in 1982 (possibly caused by high aerosol loads) were found to be the strongest factors in the trends. Cloud fraction calculations suggested that a decrease in cloud frequency might also play a role in the trends, but these studies were inconclusive. These conclusions on the impact and limitations in ability to detect each of these factors are discussed in Section 7.1.

A second scientific question was also addressed: “What anthropogenic aerosol change is detectable between 1987 and 2007?” This question was motivated by observations worldwide of a “brightening” in surface solar irradiance around 1990 [e.g., *Wild et al.*, 2005]. One of the causes suggested for this brightening is a decrease in

anthropogenic aerosols following stricter emissions regulations in Europe and the United States. *Streets et al.* [2005] modeled global aerosol emissions and estimated a decrease in global average 550 nm aerosol optical depth (AOD) of 0.003 between 1988 and 2000. *Mischenko et al.* [2007] found a decrease of 0.03 in 550 nm AOD over the oceans from 1991-2005, an order of magnitude larger than the calculations by *Streets et al.* [2005], using AOD values from the satellite-derived Global Aerosol Climatology Project. The radiative impact of anthropogenic aerosol emissions is also of great interest in climate change studies, where the forcing due to anthropogenic aerosols is still a large source of uncertainty [*Solomon et al.*, 2007].

Comparisons of measurements and the impact of stratospheric aerosol changes from volcanic eruptions on modeled irradiance showed that volcanic aerosol change was the strongest factor in the clear-sky direct normal irradiance increase between 1987 and 2007. Decreasing stratospheric aerosol loads explained all statistically significant change in clear-sky irradiance. A change in the average background 550 nm aerosol optical depth of 0.003 is consistent with the irradiance measurements, but a larger change of 0.03 can be rejected at the 99% confidence level. Section 7.2 summarizes the evidence for this conclusion as well as estimates of possible change in anthropogenic aerosol optical depth consistent with trends in clear-sky direct normal irradiance.

7.1. Examining Causes of Trends in All-sky Solar Irradiance

All-sky annual averages of total and direct normal irradiance increase at all three sites examined in Oregon over the full time period available for study (1980-2007 at Burns and Hermiston and 1976-1980 for total and 1979-1980 for direct normal irradiance in Eugene). Unlike other studies [e.g., *Dutton et al.*, 2006; *Wild et al.*, 2005], the time series show no indication of a “dimming” before 1990 followed by a “brightening”.

Calibration was eliminated as a possible cause of the increase seen in direct normal irradiance. The remarkable calibration stability of the pyrheliometers led to the choice to keep the responsivity (calibration number) of each instrument constant for its entire use in the field. Any uncorrected change in the direct normal trends from calibration would be negative. No decrease is detectable in clear-sky or all-sky direct normal measurements.

The responsivities of pyranometers used to measure total irradiance do need to be adjusted frequently to account for instrument degradation. One such pyranometer declined by 9% over 20 years of use in the field. Pyranometer responsivities were adjusted annually by taking into account the calibration history of each instrument and the decrease in solar noon measurements from clear days. Previously, the total irradiance measurements contained biases due to changes in calibration methodology and inconsistent lengths of time using the same responsivity value with an instrument. Changing the responsivity annually improved the consistency of the data set. It is possible that some atmospheric trend was removed with the calibration corrections,

particularly at Burns or Hermiston where calibration corrections relied heavily on clear-day measurements. However, any real trend that was removed was smaller than the calibration degradation, and not detectable given the limitations of the instruments and calibration histories. The comparative stability of pyrhemometers versus pyranometers indicates that direct normal irradiance is a better candidate for trend studies, particularly when looking for small changes in scattering caused by aerosols.

The strongest cause of the increase in direct normal irradiance is the stratospheric aerosols produced by the volcanic eruptions of El Chichón and Mt. Pinatubo. Removing the 4 years most heavily impacted by each of these volcanic eruptions reduces the slope of a linear trend in annual average direct normal irradiance by 20-55%, depending on the site. Removing the volcanic years also reduces the magnitude of the trend in all-sky total irradiance by 5-38%. In the months directly following both eruptions, stratospheric aerosols from volcanic eruptions reduce clear-sky direct normal irradiance at high zenith angles by up to 25%. As described in Section 7.2, comparisons of measured and modeled high-zenith angle direct normal irradiance showed that, even after removing the 4 years most heavily impacted by volcanic eruptions, decreasing stratospheric aerosol optical depth was the strongest factor contributing to the linear trend in the clear-sky direct normal irradiance between 1987 and 2007.

Lower irradiance values at the beginning of the trend were the second strongest cause of the trends. The cause of the low measurements in these early years (1980-1981) before the eruption of El Chichón is not known. The low values are visible at all three sites, in all-sky and clear-sky irradiance, and in both direct normal and total irradiance.

The difference between early (1980-1981) measurements and those at the end of the trend is stronger in the direct normal irradiance than in the total irradiance. No systematic change in the measurement systems could be identified that would cause a decrease at all three sites. Stratospheric lidar backscatter from Germany [Jäger, 2005] suggests that volcanic eruptions of Mt. St. Helens in 1980 and Agung in 1981 might have a larger impact in those years than is estimated in the volcanic aerosol data set used in the modeling [Sato *et al.*, 1993], though this would require further research to determine. Tropospheric aerosols from anthropogenic pollution could also be a cause of the low early values, though further work would be required to investigate changes in regional particulate sources like the paper industry or field burning.

Water vapor and tropospheric aerosol changes may cause small changes in the clear-sky direct normal irradiance in the clean environment in Oregon, but their magnitude is not well known. Water vapor concentrations from NCEP reanalysis [Kalnay *et al.*, 1996] increase over the time series, leading to a decrease in irradiance. The change in water vapor had a relatively small impact on direct normal irradiance compared to stratospheric aerosol changes, but affected total irradiance with a magnitude comparable to that of the exponential reduction of stratospheric aerosol loads following volcanic eruptions. The accuracy of the NCEP reanalysis vapor profiles may not be high enough for trend studies, however, so the magnitude of the impact of water vapor on the total irradiance trend is not well known. No distinguishable trend in tropospheric aerosols was found within the noise of the data, though high aerosol loads could cause the low clear-sky irradiance values before 1982. Also, an apparent dip in irradiance in 2003 in

Hermiston could be caused by local increases in particulates. Section 7.2 summarizes the possible change in tropospheric aerosols from 1987 to 2007 in more detail.

An extension of the *Long and Ackerman* [2000] algorithm was used to try to identify the change in cloudiness over the period, but the cosine response errors of the pyranometers proved to be too great to allow for confirmation of any trends. The analysis did suggest that some of the trend is caused by a decrease in cloud frequency, particularly in summer months. The direction of the trend matches cloud fraction decreases determined from human observers from 1971-1996 *Warren et al.* [2007]. A different data set or method of analysis would be needed to make any firm conclusions about the change in cloud cover.

7.2. Determining Changes in Aerosols between 1987 and 2007

Monthly average clear-sky direct normal irradiance measurements were examined at zenith angles of 65-75° for changes due to aerosols. This data set was shown to be highly sensitive to scattering by volcanic eruptions. The volcanic eruption of Mt. Pinatubo in June 1991, decreased these high zenith angle clear-sky measurements by as much as 200 W/m², or 25%, at each site. Excluding the data directly after the eruption of Mt. Pinatubo (June 1991-December 1994), the clear-sky measurements increased by 2.5% between 1987 and 2007.

Radiative transfer calculations were used to identify what portion of that 2.5% increase over 20 years was accounted for by stratospheric aerosol optical depth time series from NASA GISS [*Sato et al.*, 1993] and water vapor profiles from NCEP reanalysis data [*Kalnay et al.*, 1996]. Any remaining change in the measured irradiance, not explained by the modeled data set, was considered an estimate of the impact of the change in anthropogenic aerosols.

The trend in the differences between measured and modeled direct normal irradiances at 65-75° solar zenith angles, $0.38 \pm 0.36 \text{ W/m}^2$ per year, could be caused by a decrease in 550 nm AOD of -0.005 ± 0.005 (-6% \pm 6%). (Uncertainties represent one standard error of the trend calculations.) At a 95% confidence level, that represents a possible range in 20-year AOD change of -0.014 to 0.004. This estimate of anthropogenic aerosol change assumes a background aerosol optical depth of 0.086 and aerosol properties using a low absorbing aerosol of 1/3 continental average and 2/3 continental clean aerosol mix as defined by *Hess et al.* [1998]. The background aerosol information comes from AOD retrievals in Eugene in 2001. The magnitude of the possible 20-year change in anthropogenic AOD is consistent with the -0.003 AOD decrease calculated by *Streets et al.* [2006]. The relative magnitudes of the noise and the hypothesized signal illustrate the difficulty of measuring the forcing of anthropogenic aerosols in clean environments. Though the uncertainty range is still quite large, a 20-year AOD decrease as large as -0.03, like that found by *Mischenko et al.* [2007], can be rejected over this region.

APPENDIX A
NIP CALIBRATION RECORDS

Table A.1 lists the responsivity values used for NIPs at Eugene, Burns, and Hermiston. With the exception of N2, these responsivities were calculated from the mean value of responsivities from different calibration events over time. This appendix gives details about the calculation of those responsivities for each instrument and the uncertainty of these calibrations when they are used in the field.

Table A.1. NIP responsivities

Instrument number:	Serial #	Responsivity ($\mu\text{V}/\text{W}/\text{m}^2$)	% Uncert. (2 sigma)
N1	13170E6	8.01	1.40%
N2	17666E6	7.82	3.3%*
N3	17829E6	8.27	1.67%
N4	17668E6	8.72	1.34%
N5	18948E6	8.12	2%
N7	21149E6	8.39	1.36%
N9	14981E6	7.67	2.28%

*Not calculated from the standard deviation

Responsivities of instruments N1, N4, N5, N7, and N9 were calculated using the mean of all responsivities in their records. Twice the standard deviation of the records of each instrument is given in Table A.1 as a measure of the uncertainty of the mean responsivity. Figures A.1-A.7 plot the calibration history of each instrument listed in

Table A.1. The figures plot responsivities from individual calibration events normalized by the responsivity chosen for that instrument (as given in Table A.1) so that the percentage variation can be easily seen.

Instruments N2 and N3 both have responsivity values in their history that are several standard deviations away from the mean, and so standard responsivity values were chosen differently for these two instruments. In the case of N3, the mean responsivity was calculated from all of the calibration events except for the five high values between July of 1984 and September of 1986. While the high values are not well understood, there were several reasons to leave these values out of the mean responsivity calculation. First, all the absolute calibrations of the instrument give responsivity values within the uncertainty around the mean responsivity value quoted in Table A.1, including a calibration done in May of 1984 (right before the high values). Secondly, all calibrations done while the instrument was installed at Burns gave responsivity values consistent with the mean responsivity used. Third, using the same responsivity value for N3 gives no trend in clear day values from 1987 to the present (removing the large dip from the volcanic eruption of Mt. Pinatubo in 1991), plotted with red +'s in Figure A.9.

Instrument N2, on the other hand, shows an odd history of absolute calibrations. The responsivities from its three factory calibrations are highlighted in orange in Figure A.2. The first responsivity found in 1978 was $7.6 \mu\text{V}/\text{W}/\text{m}^2$. In 1982, the responsivity found at the Eppley factory was $8.08 \mu\text{V}/\text{W}/\text{m}^2$, 6% higher than the previous responsivity. The next calibration done at Eppley found a responsivity of $7.78 \mu\text{V}/\text{W}/\text{m}^2$ in 2001, about half way in between the other two responsivities. Because the cause of this

large variation was not understood, the average of the three responsivities found by Eppley calibrations ($7.82 \mu\text{V}/\text{W}/\text{m}^2$) was used for N2, with a 3.3% uncertainty based on the percent difference between the responsivities calculated at Eppley and their mean value.

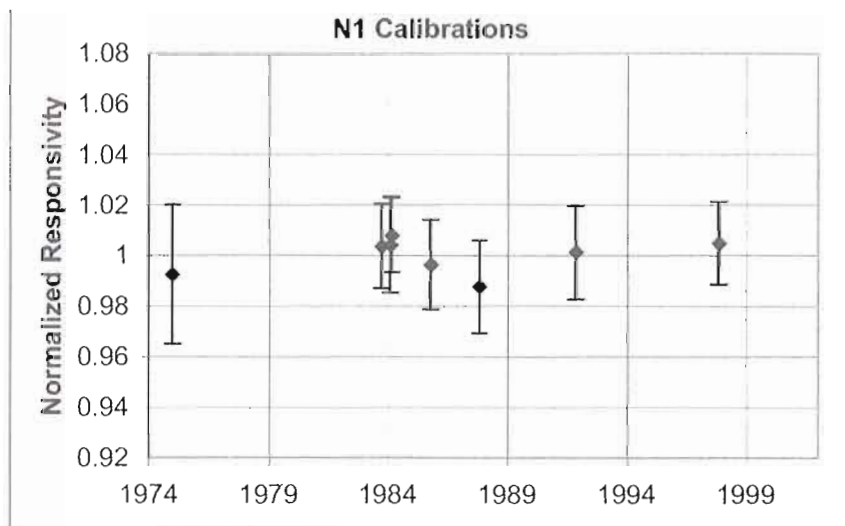


Figure A.1. N1 Calibration Record

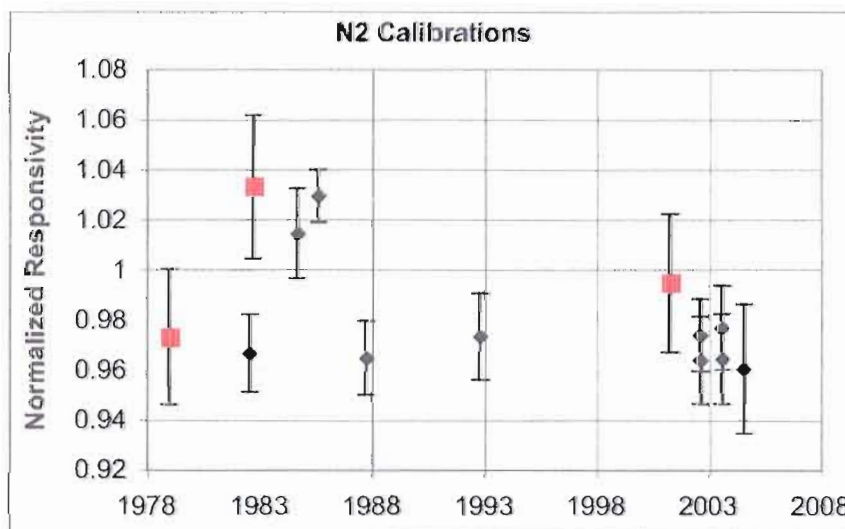


Figure A.2. N2 Calibration Record. Large red squares show calibrations done at Eppley Laboratories. The average of these three responsivities was used as the responsivity for this instrument.

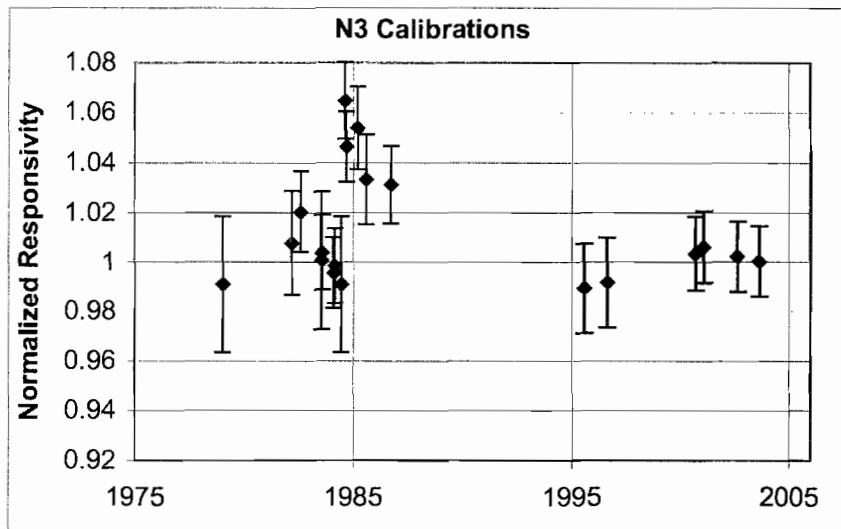


Figure A.3. N3 calibration record.

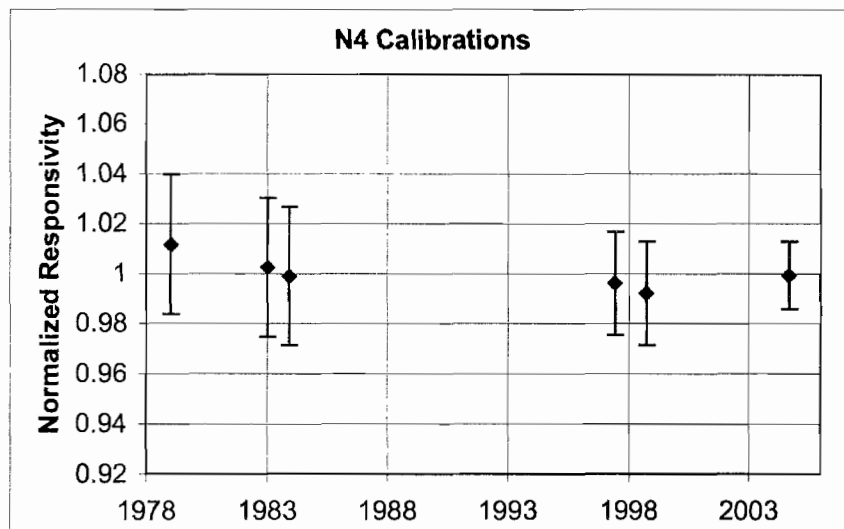


Figure A.4. N4 Calibration Record

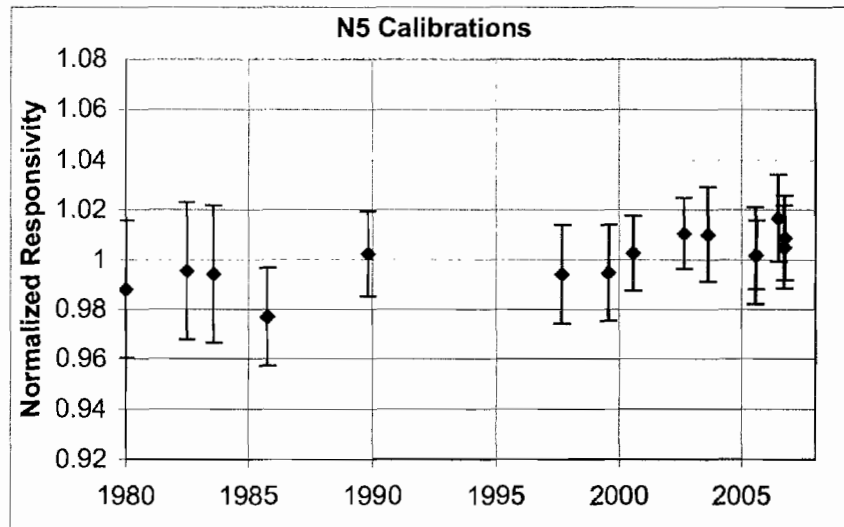


Figure A.5. N5 Calibration Record

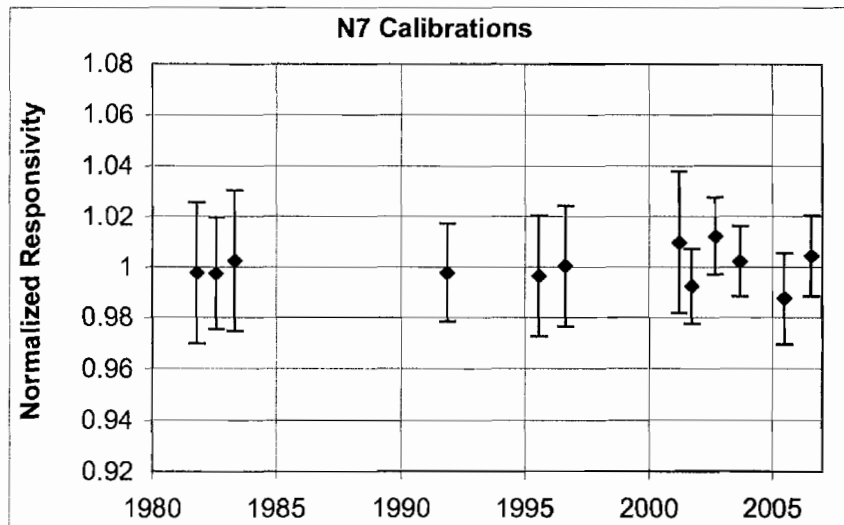


Figure A.6. N7 Calibration Record

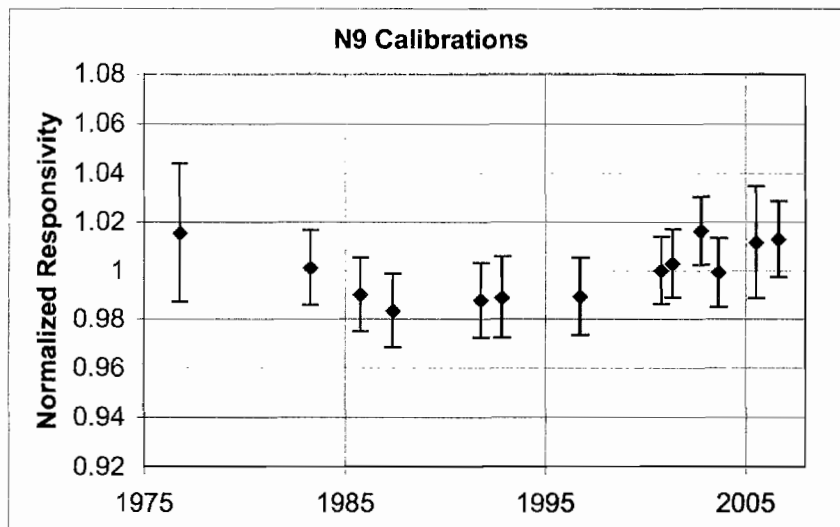


Figure A.7. N9 normalized calibration record.

Clear-sky periods at solar noon confirm the consistency of responsivities chosen for each instrument. The clear noon values were grouped into 15-day bins to improve statistics, and then normalized by the average value of the bin over all years. These clear-sky values are plotted for all three sites with each instrument represented by a different color and symbol in Figures A.8, A.9, and A.10. Besides the volcanic eruptions of El Chichón in 1982 and Mt. Pinatubo in 1991, which decrease the clear day direct normal irradiance significantly, the clear noon values show no trends over time. Periods using the same instrument for 10 years do not decrease but stay remarkably constant (e.g. N1 and N5 in Eugene, and N3 in Burns). Any discontinuities in the time series when switching instruments are within the uncertainties of the responsivities given in Table A.1.

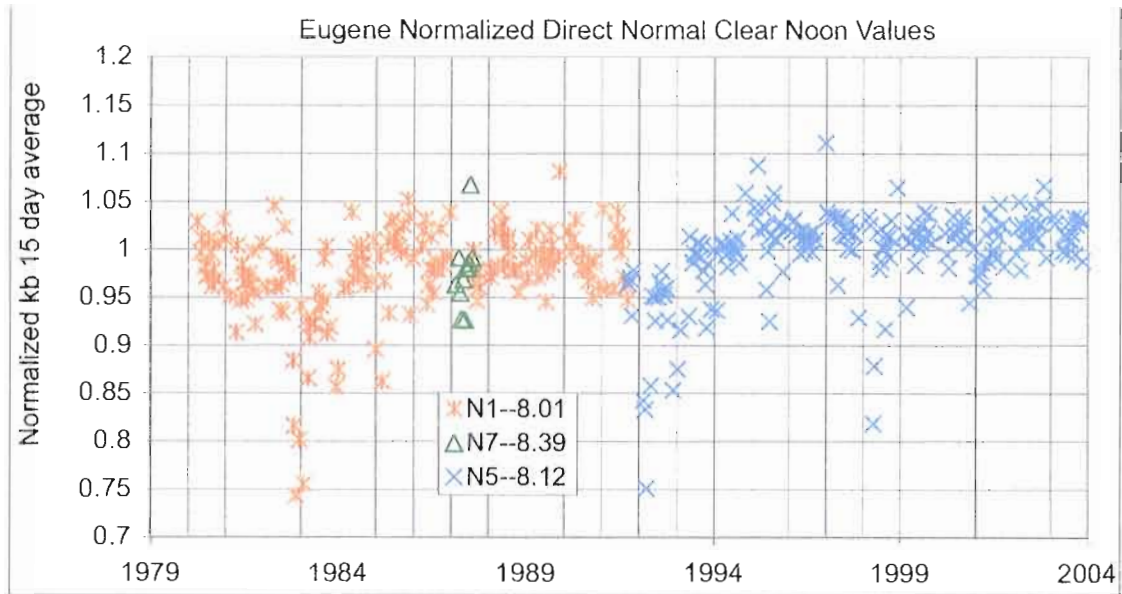


Figure A.8. Eugene normalized clear noon direct normal values.

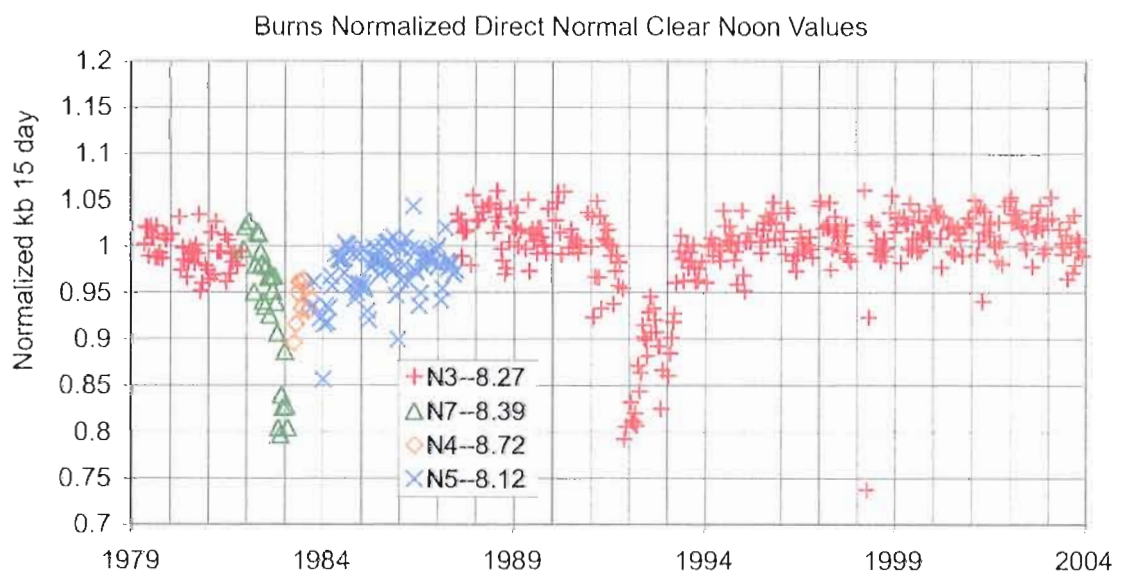


Figure A.9. Burns normalized clear noon values.

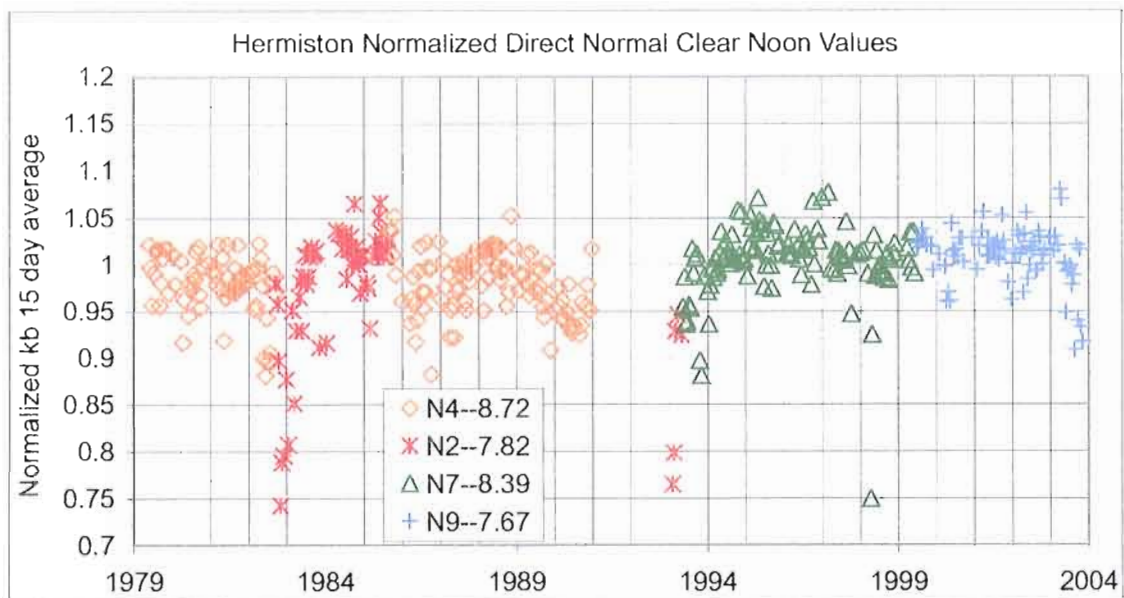


Figure A.10. Hermiston normalized clear noon values.

APPENDIX B

PSP CALIBRATION RECORDS

This appendix contains plots of the calibration records from each of the pyranometers (Figures B.2-B.6, B.8-B.9, B.11-B.16) used to measure total horizontal irradiance at the sites in this study. Clear-sky measurements at solar noon are also plotted (Figures B.1, B.7, B.10) to show the results of the calibration adjustments. As in solar noon plots in Chapter III and Appendix A, the measurements have been grouped into 15-day periods and normalized by the long-term average in that bin.

The plots of instrument calibration histories (Figures B.2-B.6, B.8-B.9, B.11-B.16) are arranged by site. Each of these figures shows the history of responsivities (in $\mu V/(W/m^2)$) for a particular instrument plotted in blue diamonds by date of calibration. Error bars plot uncertainties as 4% of the responsivity. Orange \times 's show the annually adjusted responsivity values used in the study.

Table B.1 lists the pyranometer (using the number assigned by the UO SRML) and value of responsivity used for each year and site. When multiple pyranometers were used in a year, the table contains multiple entries in the year.

B.1. Eugene Instrument Calibration Records

The responsivity corrections for the main instruments used in Eugene, P1, P3, and P19, were made by fitting regression lines to the calibration records. Other instruments used at the site were only there for periods of time less than a year so only one responsivity value was needed for the instrument.

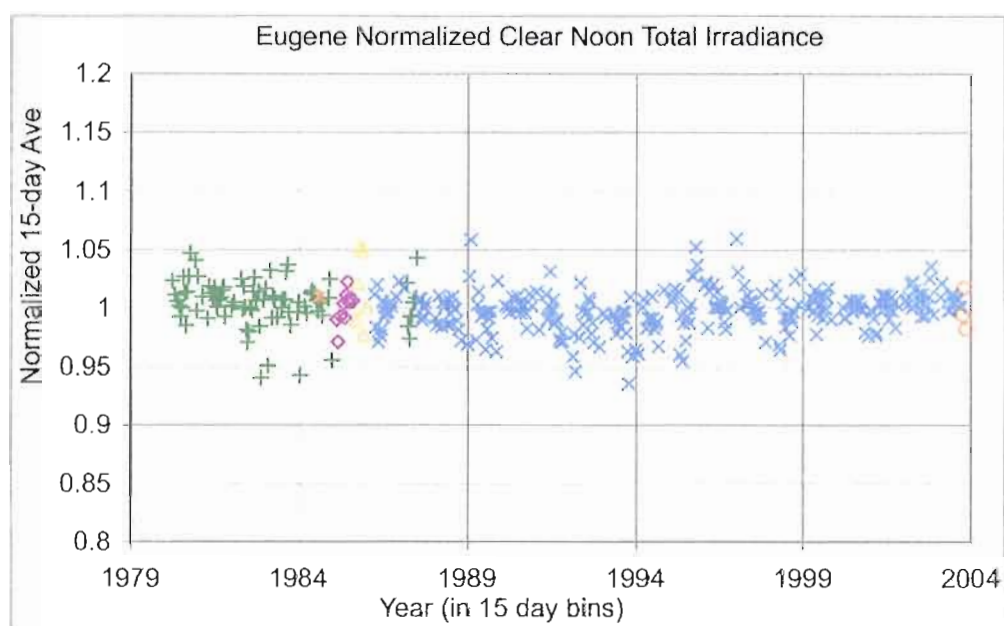


Figure B.1. Normalized clear noon values for total irradiance at Eugene. Different symbols represent different instruments.

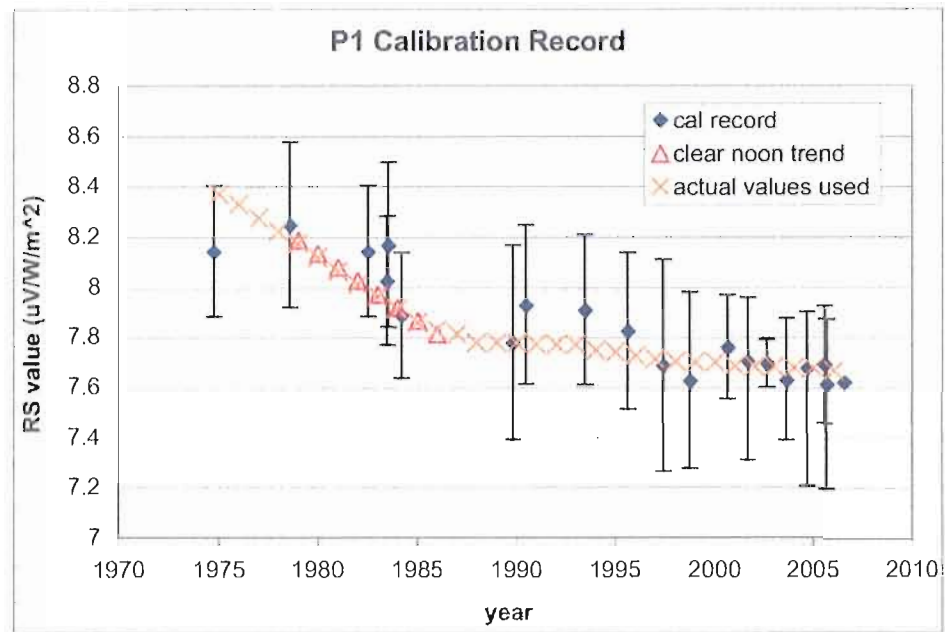


Figure B.2. Calibration records for P1. Note the change in slope of the corrected values (shown in orange x's) in 1987 when the instrument was removed from the field.

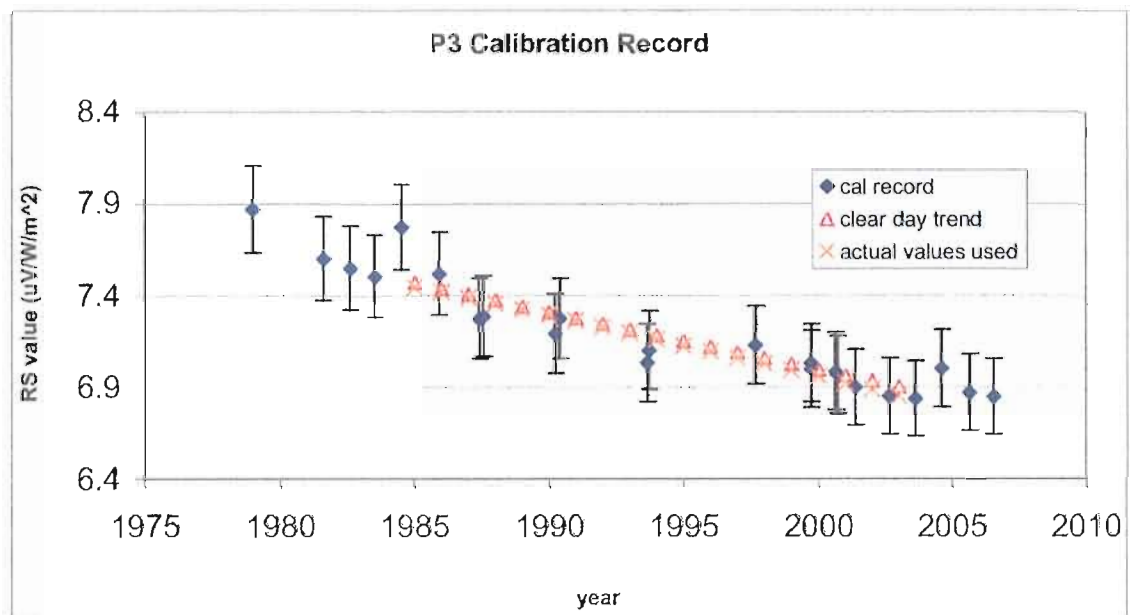


Figure B.3. Calibration records for PSP P3. Note the very close match between the corrected values based on the calibration records (orange x's) and the trend in the clear day plot (red triangles).

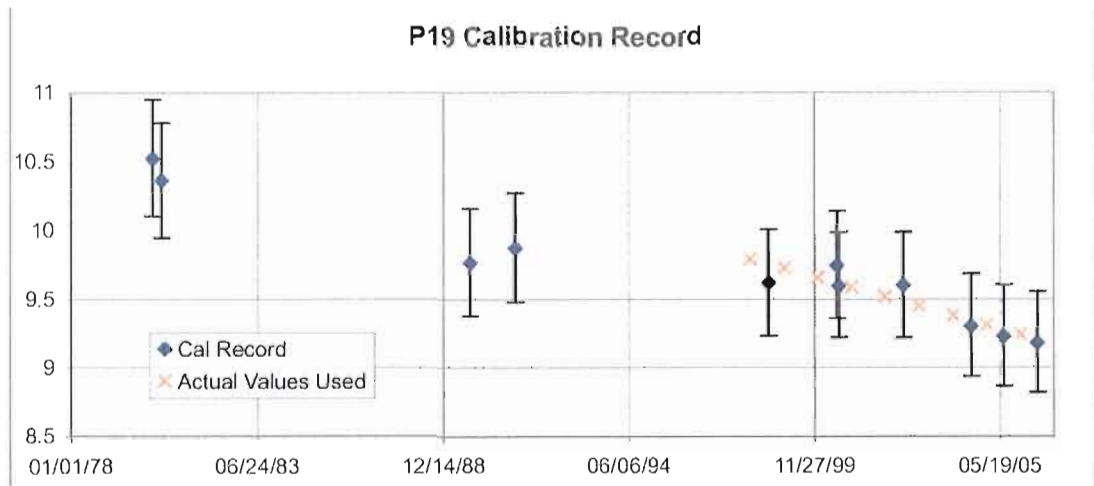


Figure B.6. Calibration records for P19.

B.2. Burns PSP Calibration Records

Only two PSPs have been used at Burns since 1979. P4 was corrected using clear noon values, but P20 responsivities were corrected by fitting a linear regression trend of the most recent calibrations. As seen in Figure B.8, the clear noon corrected responsivities (shown in orange x's) match the trend line fit to the calibration records extremely well. This is another confirmation of the equivalence of correcting responsivities by clear day measurements or calibration records.

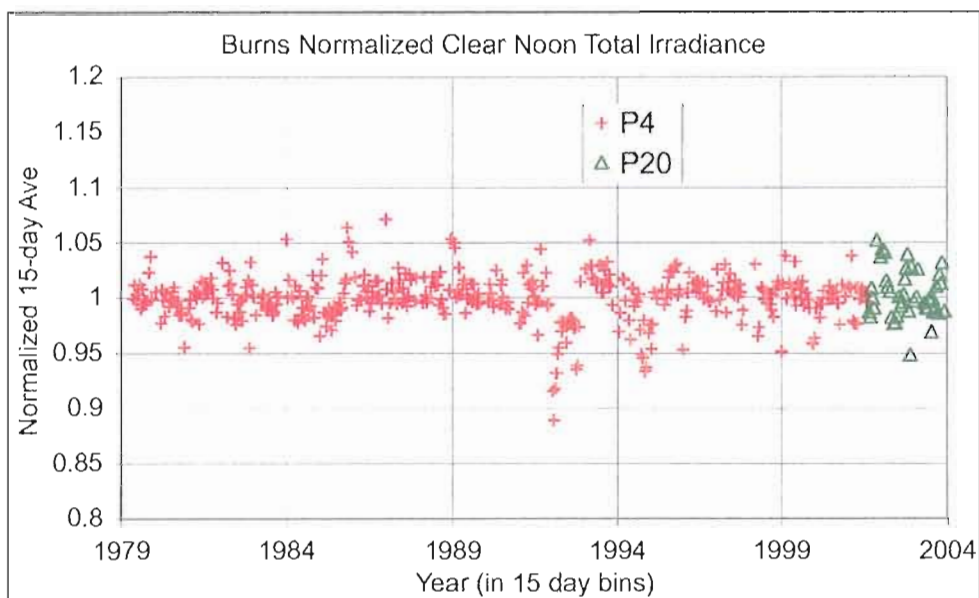


Figure B.7. Normalized clear day solar noon values for total irradiance at Burns.

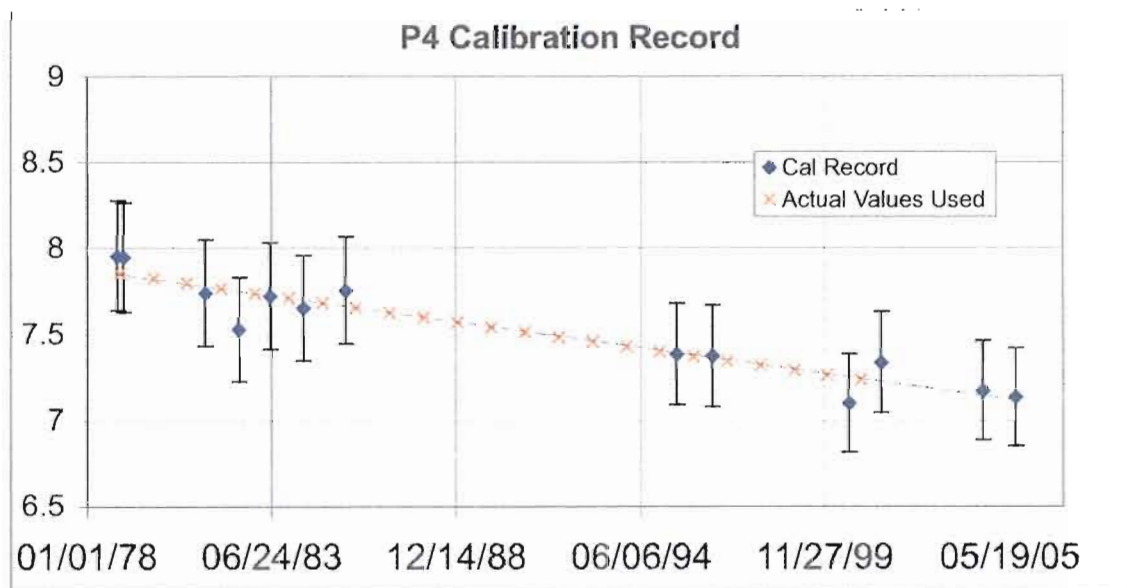


Figure B.8. Calibration records for P4. The line is a regression fit to responsivities from calibration events. Note the incredibly good fit between the clear noon corrected responsivities (orange x's) and the trend line. The actual values used were found by fitting a trend line to the clear day solar noon records. This is another confirmation that the clear day trend is caused by sensor degradation.

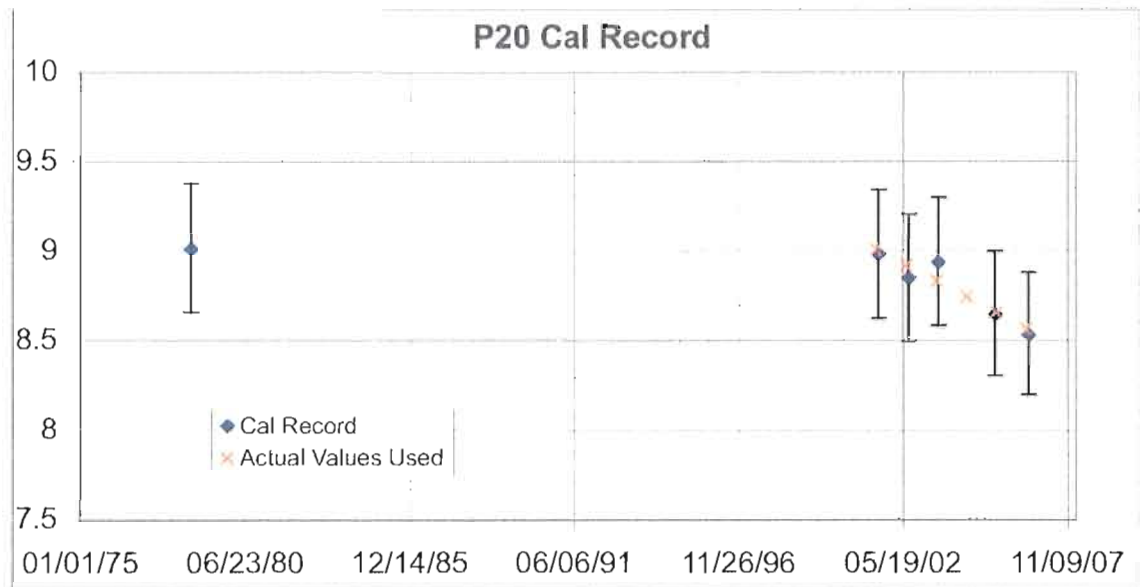


Figure B.9. P20 calibration values were chosen by a line fit to recent calibrations as there was not enough clear day data to determine responsivity values from a clear day trend.

B.3. Hermiston PSP Calibration Records

The responsivity for PSPs used in Hermiston was corrected using clear day values to determine the percent change per year. The values of the responsivities were then determined by fitting that annual change to the absolute values from calibration events. Figures B.11-B.16 show once again how closely the clear noon corrected values (the orange x's) fit the calibration records for the times when the instruments were in use.

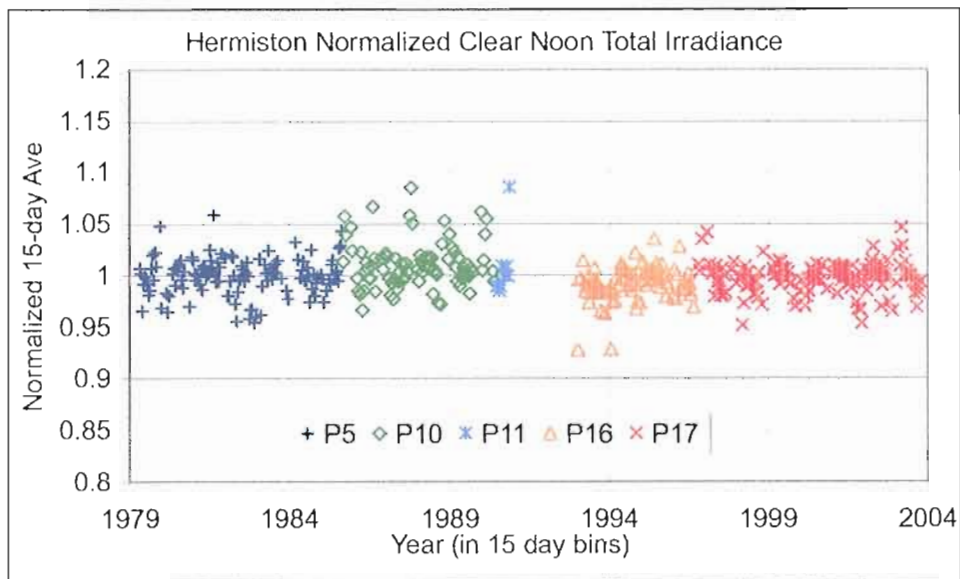


Figure B.10. Normalized clear day values for Hermiston global measurements at solar noon. Plot uses annually corrected responsivity values for instruments.

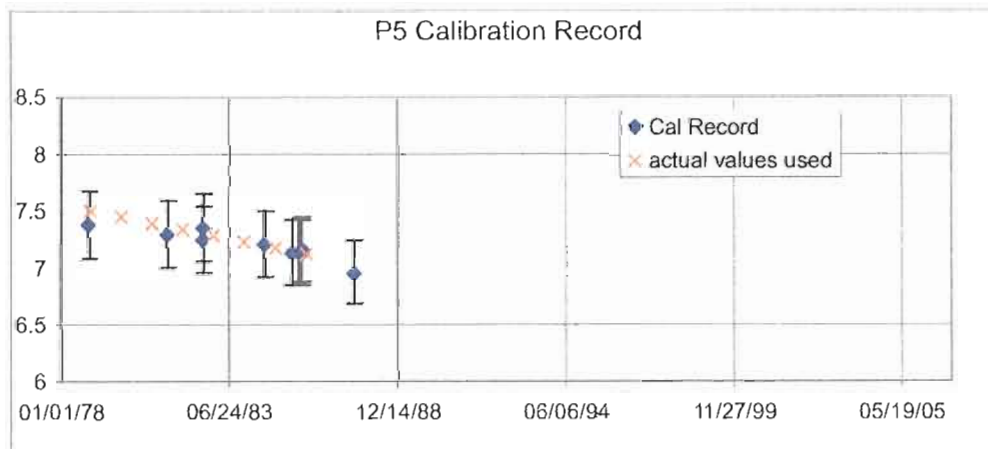


Figure B.11. Calibration records for P5.

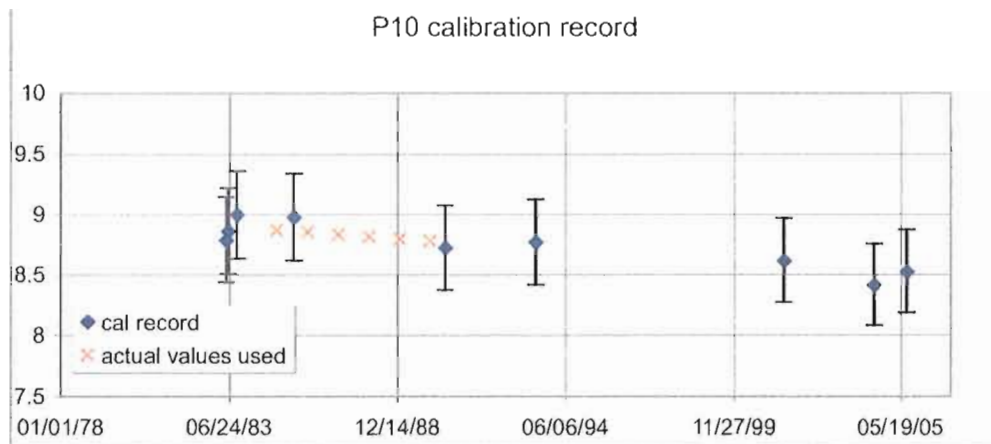


Figure B.12. Calibration records for P10.

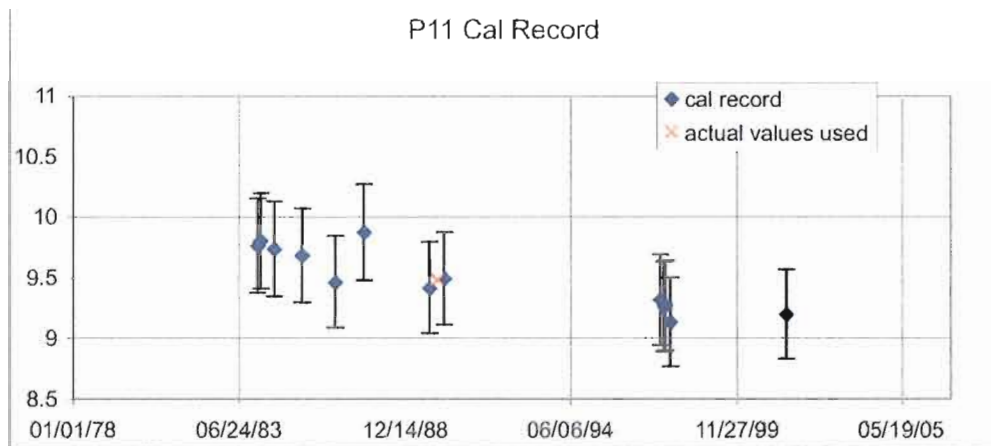


Figure B.13. Calibration records for P11.

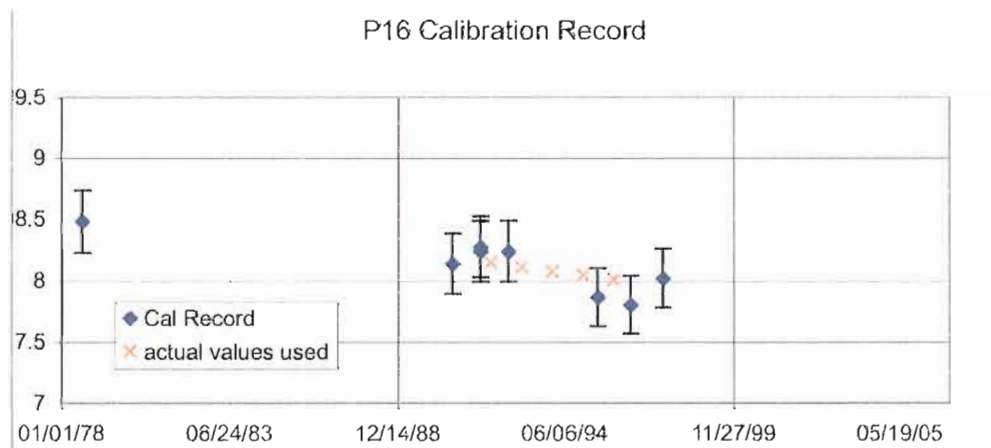


Figure B.14. Calibration records for P16.

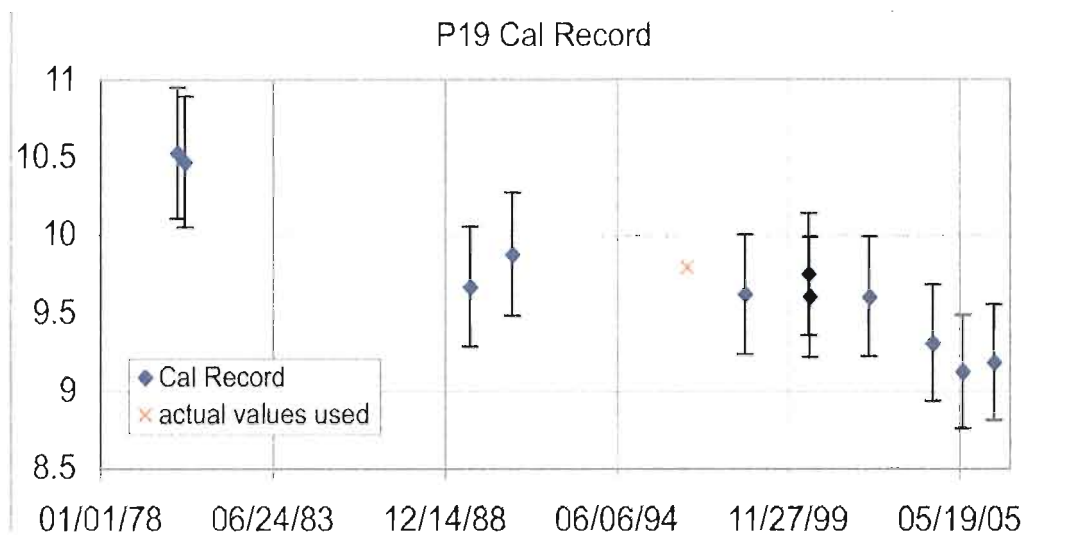


Figure B.15. Calibration records for P19.

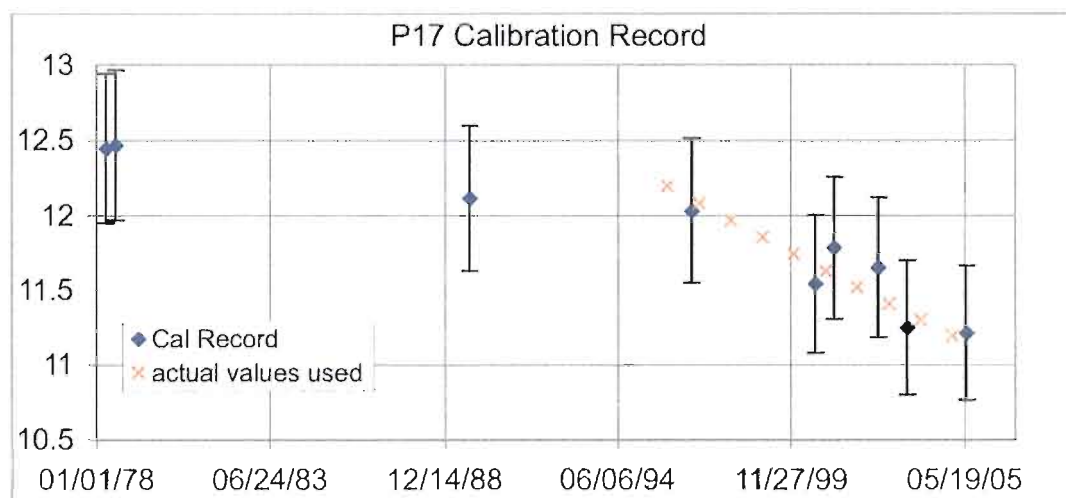


Figure B.16. Calibration records for P17.

Table B.1. PSPs and responsivities used at each site for each year.

<i>Year</i>	Eugene		Burns		Hermiston	
	<i>Inst.</i>	<i>RS</i>	<i>Inst.</i>	<i>RS</i>	<i>Inst.</i>	<i>RS</i>
1975	P1	8.372				
1976	P1	8.330				
1977	P1	8.277				
1978	P1	8.222				
1979	P1	8.174	P4	7.855	P5	7.497
1980	P1	8.120	P4	7.826	P5	7.444
1981	P1	8.065	P4	7.796	P5	7.390
1982	P1	8.011	P4	7.767	P5	7.338
1983	P1	7.963	P4	7.739	P5	7.285
1984	P1	7.914	P4	7.710	P5	7.233
	P9	9.053				
	P12	8.840				
1985	P1	7.861	P4	7.681	P5	7.181
	P3	7.446			P10	8.871
	P7	8.741				
1986	P7	8.741	P4	7.653	P10	8.853
	P3	7.418				
1987	P3	7.389	P4	7.624	P10	8.835
1988	P3	7.356	P4	7.596	P10	8.818
1989	P3	7.324	P4	7.568	P10	8.800
1990	P3	7.293	P4	7.540	P10	8.782
1991	P3	7.261	P4	7.512	P11	9.410
1992	P3	7.226	P4	7.484	P16	8.152
	P16	8.152			P19	9.794
1993	P3	7.194	P4	7.456	P16	8.115
1994	P3	7.160	P4	7.428	P16	8.079
1995	P3	7.127	P4	7.400	P16	8.043
1996	P3	7.093	P4	7.373	P16	8.007
					P19	9.794
					P17	12.197
1997	P3	7.059	P4	7.346	P17	12.081
1998	P3	7.027	P4	7.318	P17	11.966
1999	P3	6.994	P4	7.291	P17	11.852
2000	P3	6.960	P4	7.264	P17	11.740
2001	P3	6.925	P4	7.237	P17	11.628
			P20	9.005		
2002	P3	6.890	P20	8.917	P17	11.517

Table B.1. (continued).

<i>Year</i>	Eugene		Burns		Hermiston	
	<i>Inst.</i>	<i>RS</i>	<i>Inst.</i>	<i>RS</i>	<i>Inst.</i>	<i>RS</i>
2003	P3	6.855	P20	8.830	P17	11.408
	P19	9.451				
2004	P19	9.383	P20	8.742	P17	11.299
2005	P19	9.314	P20	8.655	P17	11.192
2006	P19	9.245	P20	8.567	P17	11.086
2007	P22	9.603	P20	8.479	P17	10.980
	P19	9.177				

APPENDIX C
COMPARING AUTOMATED IDENTIFICATION OF CLEAR PERIODS TO
MANUAL IDENTIFICATION USING CHARTS

The *Long and Ackerman* [2000] automated method (hereafter called the SWC method) of identifying clear data was compared to the method of manually identifying clear periods from continuously plotted chart records. The comparison was done using clear periods around solar noon as these had already been identified manually, as described in Chapter III. The charts have a higher time resolution (on the order of seconds) than the 5-minute average data used with the SWC method. It was thought that the SWC method might compare poorly to the chart identification method because it would not be able to identify the high time resolution variability. The SWC method identified more days as clear around solar noon than the manual method, but this does not seem to be primarily related to the 5-minute resolution. Requiring both solar noon and half of the data points within one hour of solar noon to be identified clear with the SWC method, improves the agreement between the SWC method and manual chart identification.

Both one-minute and five-minute resolution data from Eugene were used with the SWC method from 2001 through 2006 to examine the impact of using 5-minute to identify clear days with this method. The agreement between the two was good. 97% of days found clear within ten minutes of solar noon in the 5-minute data were also found clear in the 1-minute data. This implies that the 5-minute data does not often average out too much of the variability from clouds to identify cloudy skies. The 1-minute resolution data identifies slightly more days as clear at solar noon than the 5-minute data, with 94% of the 535 days with clear solar noon periods found in the 1-minute data also found in the 5-minute data.

First, days were determined with the SWC method that had at least one point identified as clear within ten minutes of solar noon. These SWC identified days were compared to the list of days with clear noon periods identified by the manual chart method. From 2001-2003, 179 days were identified clear by both methods. The manual identification method identified 187 days as clear at solar noon, but the SWC method identified 267 days as clear. Thus, the SWC method finds generally the same clear noon periods as the manual method, but identifies many other days as clear as well. 2001 was examined more closely to understand these additional clear periods.

By normalizing the clear noon irradiances by extraterrestrial radiation, it was seen that some of the days marked clear by the SWC method but not the manual method do not appear to be as clear as days identified by both methods. The normalization was done for total, direct, and diffuse irradiance and is plotted by day of the year in Figures C.1, C.2, and C.3, for those components of radiation respectively. The orange asterisk's show

points from the manual chart method, and the navy blue outlined triangles are SWC points. The “less” clear SWC points can be seen particularly well in the diffuse data (Figure C.3), where there are a number of blue triangles from days 200-300 that are higher than their neighbors.

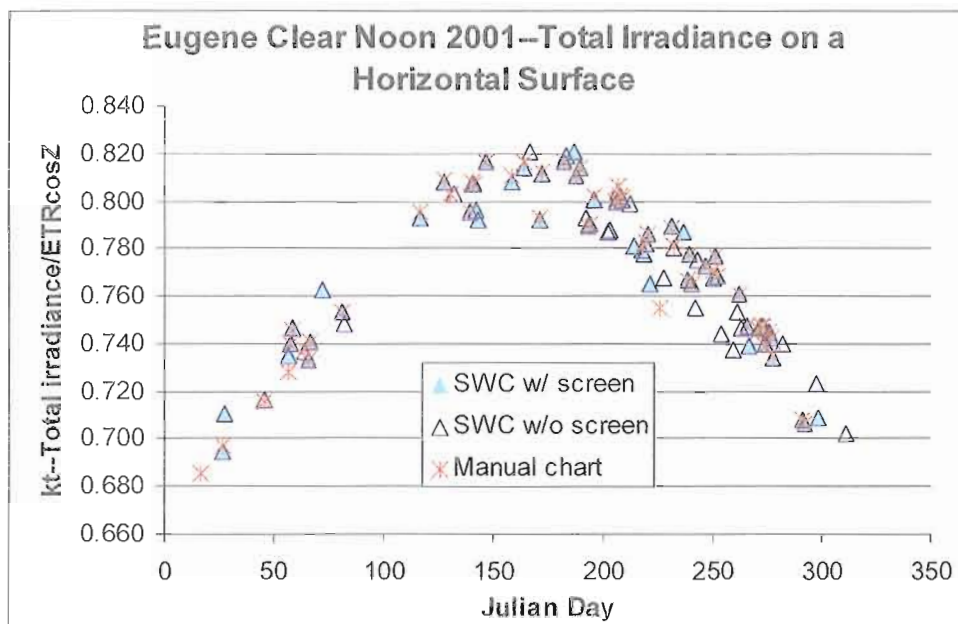


Figure C.1. Total irradiance at solar noon identified as clear and normalized by extraterrestrial solar radiation (kt) for Eugene in 2001. The orange asterisk's plot kt identified clear at solar noon by manual chart inspection. Navy blue outlined triangles represent days with at least one point identified as clear within 10 minutes of solar noon by the SWC method. Those triangles filled in with light blue passed an additional screening requiring at least half of the points +/- 1 hr of solar noon to also be clear.

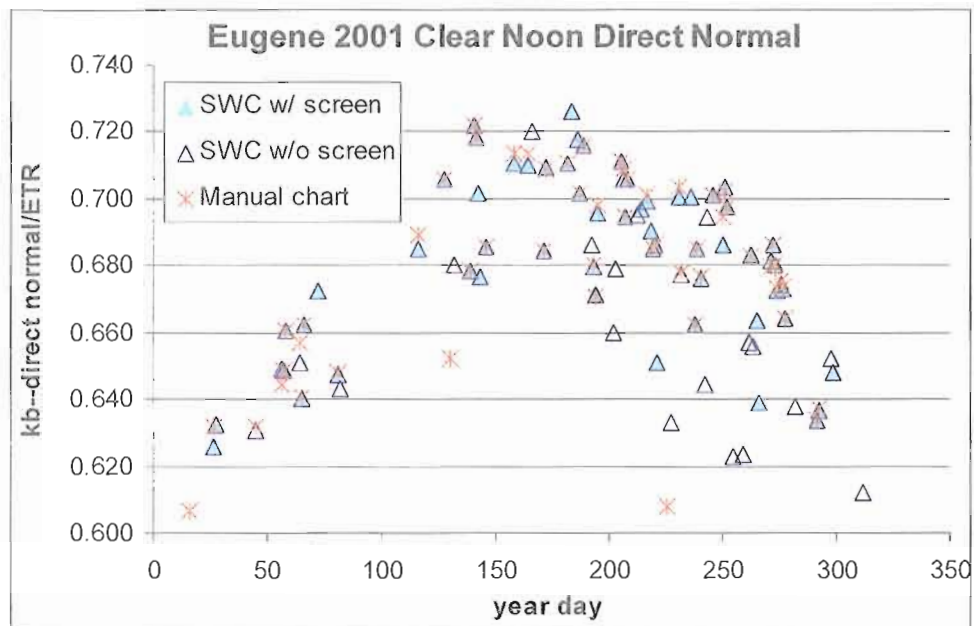


Figure C.2. Clear solar noon direct normal irradiance measurements normalized by extraterrestrial solar irradiance for clear noon periods (kb). Symbols described in Figure C.1.

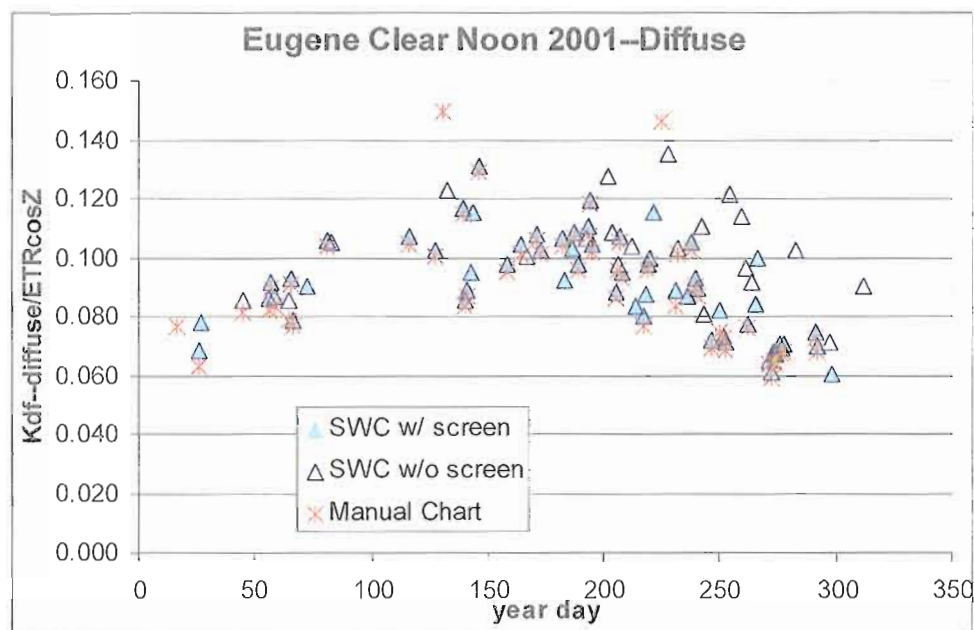


Figure C.3. Clear solar noon diffuse measurements normalized by extraterrestrial irradiance for the year 2001. Symbols described in Figure C.1.

When an additional screen was applied to the SWC data, most of those high points were eliminated. The SWC identified clear noon periods were screened to also require at least half of the points in the 2-hour period surrounding solar noon to be identified as clear. The SWC points that passed this additional screen are filled in with light blue in Figures C.1 to C.3. Most of the high diffuse points in Figure C.3 did not pass this screen and thus are not filled in with light blue. This additional screen helps the data sets match better because the SWC method measures the variability criteria for cloudiness over a period of 15 minutes, while a human observer looks at a longer time period. When examining the chart records, a person is likely to look at the variability for an hour or two around noon and not isolate only a 15-minute period, which is only 0.5 centimeters on the chart records.

This additional screen does not give complete agreement between the two records, but it does bring improvement. Table C.1 gives a summary of the number of days found clear with each method for 2001 with and without the additional screen. In 2001 at Eugene, 54 days are determined clear at solar noon by the manual chart method. Without the additional screen of the 2 hours surrounding solar noon being at least half clear, 52 of those points are also identified clear by the SWC method out of the 81 total days determined clear. With the screen, only 47 of the points remain identified clear by both the SWC and manual methods. However, now only 60 points are identified clear by the SWC method, so that 87% of points identified by SWC are also identified by manual methods compared to 64% without the additional screen. There is an inherent subjectivity in the manual method that is not present in the SWC method, because the observer who

chooses clear periods does so by eye rather than by a strict numerical definition of clear sky. Thus, some of the difference between the results of these two methods may also be due to this subjectivity in addition to the differing time resolution of the data sets.

Table C.1. Number of days found clear at noon using automated and manual methods

<i>Clear ID Method:</i>	<i>Without screen</i>	<i>With screen</i>
Both	52	47
SWC Method	81	60
Manual Chart	54	54

The automated SWC method finds the majority of clear periods at solar noon that a manual clear noon identification scheme also finds. With an additional screening requiring both the data points at noon to be clear and half of the period in the 2 hours surrounding noon to be clear, the automated method determines clear periods with only minimal differences from the manual method. The additional screening eliminates some of the most questionable clear periods, giving very good agreement in the average clear noon values.

REFERENCES

Alpert, P., P. Kishcha, Y. J. Kaufman, and R. Schwarzbard (2005), Global dimming or local dimming?: Effect of urbanization on sunlight availability. *Geophys. Res. Lett.*, *32*, L17802, doi:10.1029/2005GL023320.

Augustine, J.A., C.R. Cornwall, G.B. Hodges, C.N. Long, C.I. Medina, and J.J. DeLuisi (2003), An automated method of MFRSR calibration for aerosol optical depth analysis with application to an Asian dust outbreak over the United States, *J. Appl. Meteor.*, *42*, 266-278.

Bush, B. C., F. Valero, and A. S. Simpson (2000), Characterization of thermal effects in pyranometers: A data correction algorithm for improved measurement of surface insolation, *J. Atmos. Ocean. Technol.*, *17*, 165-175.

Che, H. Z., G. Y. Shi, X. Y. Zhang, R. Arimoto, J.Z. Zhao, L. Xu, B. Wang, and Z. H. Chen (2005), Analysis of 40 years of solar radiation data from China, 1961-2000, *Geophys. Res. Lett.*, *32*, L06803, doi:10.1029/2004GL022322.

Dutton, E. G., J. J. Michalsky, T. Stoffel, B. W. Forgan, J. Hickey, D. W. Nelson, T. L. Alberta, and I. Reda (2001), Measurement of broadband diffuse solar irradiance using current commercial instrumentation with a correction for thermal offset errors. *J. Atmos. Ocean. Technol.*, *18*, 297-314.

Dutton, E. G., D. W. Nelson, R. S. Stone, D. Longnecker, G. Carbaugh, J. M. Harris, and J. Wendell (2006), Decadal variations in surface solar irradiance as observed in a globally remote network, *J. Geophys. Res.*, *111*, D19101, doi:10.1029/2005JD006901.

El-Wakil, S. A., M. El-Metwally, and C. Gueymard (2001), Atmospheric turbidity of urban and desert areas of the Nile Basin in the aftermath of Mt. Pinatubo's eruption, *Theor. Appl. Climatol.*, *68*, 89-108.

Fröhlich, C., and J. Lean (1998), The sun's total irradiance: Cycles, trends and related climate change uncertainties since 1976, *Geophys. Res. Lett.*, 25(23), 4377-4380.

Fu, Q., and K. Liou (1992), On the correlated k -distribution method for radiative transfer in nonhomogenous atmospheres, *J. Atmos. Sci.*, 49(22), 2139-2156.

Gilgen, H., and Ohmura, A. (1999), The Global Energy Balance Archive. *Bull. Amer. Meteorol. Soc.*, 80(5), 831-850.

Gilgen, H., M. Wild, and A. Ohmura (1998), Means and trends of shortwave irradiance at the surface estimated from Global Energy Balance Archive Data. *J. Climate*, 11, 2042-2061.

Guo, G., and J. A. Coakley (2008), Satellite estimates and shipboard observations of downward radiative fluxes at the ocean surface. *J. Atmos. Ocean. Technol.*, 25, 429-441, doi:10.1175/2007JTECHA990.1.

Hess, M., P. Koepke, and I. Shult (1998), Optical Properties of Aerosols and Clouds: The software package OPAC., *Bull. Amer. Meteorol. Soc.*, 79(5), 831-844.

Hinkelman, L. M., T. Zhang, B. Weatherhead, B. A. Wielicki, P. W. Stackhouse Jr., J. C. Mikovitz, M. Wild, and A. Ohmura (2006), Detection of global energy budget trends using satellite and surface sites: is the current surface site distribution sufficient?, paper presented at 12th Conference on Atmos. Rad., Amer. Meteor. Soc., Madison, Wisconsin, 10-14 July.

Jäger, H. (2005), Long-term record of lidar observations of the stratospheric aerosol layer at Garmisch-Partenkirchen, *J. Geophys. Res.*, 110, D08106, doi:10.1029/2004JD005506

Kalnay, E., et al. (1996), The NCEP/NCAR 40-year reanalysis project, *Bull. Amer. Meteorol. Soc.*, 77, 437-470.

Liepert, B. G. (2002), Observed reductions of surface solar radiation at sites in the United States and worldwide from 1961 to 1990, *Geophys. Res. Lett.*, 29(10), 1421, doi:10.1029/2002GL014910.

Liepert, B. G., and G. J. Kukla (1997), Decline in global solar radiation with increased horizontal visibility in Germany between 1964 and 1990, *J. Climate*, 10, 2391-2401.

Lohmann, S., L. Riihimaki, F. Vignola, and R. Meyer (2007), Trends in direct normal irradiance in Oregon: Comparison of surface measurements and ISCCP-derived irradiance, *Geophys. Res. Lett.*, 34, L02705, doi:10.1029/2006GL027322.

- Long, C. N., and T. P. Ackerman (2000), Identification of clear skies from broadband pyranometer measurements and calculation of downwelling shortwave cloud effects, *J. Geophys. Res.*, 105(D12), 15,609-15,626.
- Long, C. N., and K. L. Gaustad (2004), The shortwave (SW) clear-sky detection and fitting algorithm: algorithm operational details and explanations, Tech. Rep. ARM TR-004, Atmos. Rad. Meas. Prog., U.S. Dept. of Energy, Washington, D.C.
- Long, C. N., T. P. Ackerman, J. J. DeLuisi, and J. Augustine (1999), Estimation of Fractional Sky Cover from Broadband SW Radiometer Measurements, paper presented at 10th Conference on Atmos. Rad., Amer. Meteor. Soc., Madison, Wisconsin, 28 June–2 July.
- Michalsky, J. J., and G. M. Stokes (1983), Mt. St. Helens' aerosols – Some tropospheric and stratospheric effects, *J. Climate Appl. Meteor.*, 22, 640-648.
- Myers, D., T. L. Stoffel, I. Reda, S. M. Wilcox, and A. M. Andreas (2002), Recent progress in reducing the uncertainty in and improving pyranometer calibrations, *J. Sol. Energy Eng.*, 124(1), 44-50, doi:10.1115/1.1434262.
- Myers, D.R., I. Reda, S. Wilcox, and A. Andreas (2004), Optical radiation measurements for photovoltaic applications: instrumentation uncertainty and performance, *Proc. SPIE*, 5520, 142, doi:10.1117/12.555947.
- Mishchenko, M. I., I. V. Geogdzhayev, W. B. Rossow, B. Cairns, B. E. Carlson, A. A. Lacis, L. Liu, and L. D. Travis (2007), Long-term satellite record reveals likely recent aerosol trend, *Science*, 315, 1543, doi:10.1126/science.1136709.
- Nelson, R. J., J. R. Augustyne, and C. Jennings (1994), Radiometer calibration drift, in *Proceedings of the 1994 Annual Conference of the American Solar Energy Society, San Jose, Cal., June 27-30, 1994*, edited by S. Burley, M. E. Arden, R. Campbell-Howe, and B. Wilkins-Crowder, pp. 385-389, Am. Sol. Energy Soc., Boulder, Colo.
- Maxwell, E. L., W. F. Marion, D. R. Myers, M. D. Rymes, and S. M. Wilcox (1995), National Solar Radiation Data Base (1961-1990). Final technical report. Volume 2, Nat. Ren. Energy Lab., Golden, Colo., doi:10.2172/70747.
- Pinker, R.T., B. Zhang, and E. G. Dutton (2005), Do satellites detect trends in surface solar radiation? *Science*, 308(5723), 850-854, doi:10.1126/science.1103159.
- Pittock, A. B. (2006), "Are Scientists Underestimating Climate Change?" *Eos Trans. AGU*, 87(34), 340.

Qian, Y., D. P. Kaiser, L. R. Leung, and M. Xu (2006), More frequent cloud-free sky and less surface solar radiation in China from 1955 to 2000, *Geophys. Res. Lett.*, *33*, L01812, doi:10.1029/2005GL024586.

Riihimaki, L., F. Vignola, S. Lohmann, R. Meyer, and R. Perez (2006), Long-term variability of global and beam irradiance in the pacific northwest, in *Denver Solar 2006, July 18-13, 2006, Denver, Colorado: Proceedings of 35th ASES Annual Conference* [CD-ROM], edited by R. Campbell-Howe, Am. Sol. Energy Soc., Boulder, Colo.

Sato, M., J. E. Hansen, M. P. McCormick, and J. B. Pollack (1993), Stratospheric aerosol optical depths, 1850-1990, *J. Geophys. Res.*, *98*, 22,987-22,994.

Schwartz, R. D. (2005), Global dimming: Clear-sky atmospheric transmission from astronomical extinction measurements, *J. Geophys. Res.*, *110*, D14210, doi:10.1029/2005JD005882.

Solomon, S., D. Qin, M. Manning, Z. Chen, M. Marquis, K. B. Averyt, M. Tignor, and H. L. Miller (Eds.) (2007), *Climate Change 2007: The Physical Science Basis: Contribution of Working Group I to the Fourth Assessment Report of the Intergovernmental Panel on Climate Change*, 996 pp., Cambridge Univ. Press, New York.

Stamnes, K., S.-C. Tsay, K. Jayaweera, and W. Wiscombe (1988), Numerically stable algorithm for discrete ordinate-method radiative transfer in multiple scattering and emitting layered media, *Appl. Opt.*, *27*, 2502-2509.

Stanhill, G., and S. Cohen (2001), Global dimming: A review of the evidence for a widespread and significant reduction in global radiation with discussion of its probable causes and possible agricultural consequences, *Agric. Forest Meteorol.*, *107*, 255-278.

Streets, D. G., Y. Wu, and M. Chin (2006), Two-decadal aerosol trends as a likely explanation of the global dimming/brightening transition, *Geophys. Res. Lett.*, *33*, L15806, doi:10.1029/2006GL026471.

Vignola, F. (2006), Removing systematic errors from rotating shadowband pyranometers data, in *Denver Solar 2006, July 18-13, 2006, Denver, Colorado: Proceedings of 35th ASES Annual Conference* [CD-ROM], edited by R. Campbell-Howe, Am. Sol. Energy Soc., Boulder, Colo.

Vignola, F., and D. K. McDaniels (1986), Beam-global correlations in the Pacific Northwest, *Solar Energy*, *36*(5), 409-418.

Vignola, F., and R. Perez (2004), Solar Resource GIS Data Base for the Pacific Northwest using Satellite Data, Final Tech. Report, DOE DEPS36-0036-00GO10499, US Dept. of Energy, Washington, DC. doi:10.2172/839110.

Vignola, F., and I. Reda (1998), Responsivity of an Eppley NIP as a Function of Time and Temperature, in *Proceedings of the 1998 Annual Conference of the American Solar Energy Society, Albuquerque, NM, June 14-17, 1998*, edited by R. Campbell-Howe, T. Cortez, and B. Wilkins-Crowder, pp. 517-522, Am. Sol. Energy Soc., Boulder, Colo.

Warren, S. G., R. M. Eastman, and C. J. Hahn (2007), A survey of changes in cloud cover and cloud types over land from surface observations, 1971-96, *J. Climate*, 20(4), 717-738, doi:10.1175/JCLI4031.1.

Weatherhead, E. C., et al. (1998), Factors affecting the detection of trends: Statistical considerations and applications to environmental data, *J. Geophys. Res.*, 103(D14), 17149-17161.

Wilcox, S., D. Myers, N. Al-Abbadi, and M. Y. B. Mahfoodh (2001), Using irradiance and temperature to determine the need for radiometer calibrations, in *Forum 2001: Solar Energy, the Power to Choose, Washington, D.C., April 21-25, 2001: Proceedings of ASES Annual Conference* [CD-ROM], edited by R. Campbell-Howe, Am. Sol. Energy Soc., Boulder, Colo.

Wild, M., H. Gilgen, A. Roesch, A. Ohmura, C. N. Long, E. G. Dutton, B. Forgan, A. Kallis, V. Russak, and A. Tsvetkov (2005), From dimming to brightening: Decadal changes in solar radiation at Earth's surface. *Science*, 308, 845-850.

Wiscombe, W. (1977), The delta- M method: Rapid yet accurate radiative flux calculations for strongly asymmetric phase functions, *J. Atmos. Sci.*, 34, 1408-1422.